THE VISUALIZATION OF SECOND-ORDER TENSOR FIELDS

A DISSERTATION
SUBMITTED TO THE DEPARTMENT OF APPLIED PHYSICS
AND THE COMMITTEE ON GRADUATE STUDIES
OF STANFORD UNIVERSITY
IN PARTIAL FULFILLMENT OF THE REQUIREMENTS
FOR THE DEGREE OF
DOCTOR OF PHILOSOPHY

Thierry Delmarcelle
December 1994

© Copyright by Thierry Delmarcelle 1994
All Rights Reserved

I certify that I have read this dissertation and that in my opinion it is fully adequate, in scope and quality, as a dissertation for the degree of Doctor of Philosophy.

Lambertus Hesselink
Department of Electrical Engineering
(Principal Adviser)

I certify that I have read this dissertation and that in my opinion it is fully adequate, in scope and quality, as a dissertation for the degree of Doctor of Philosophy.

Marc Levoy
Department of Computer Sciences

I certify that I have read this dissertation and that in my opinion it is fully adequate, in scope and quality, as a dissertation for the degree of Doctor of Philosophy.

Sebastian Doniach
Department of Applied Physics

Approved for the University Committee on Graduate Studies:

Abstract

The field of scientific visualization covers the study of visual representations of scientific data. These data often consist of continuous scalar, vector, or second-order tensor fields extending across a $n-$dimensional space, $n \geq 1$. While research efforts aimed at developing efficient representations of scalar and vector data have led to important achievements, this dissertation is the first extensive study of visualization techniques for second-order tensor fields.

Tensor fields are multivariate; they can embed as much information as n^2 scalar fields, or equivalently, n vector fields. Visualizing continuous tensor data is, therefore, difficult mainly because the underlying continuity must be rendered while visual clutter has to be avoided. We develop a theoretical ground work for the visualization of symmetric tensor fields by studying their geometry and their topological structure, and by designing at each step appropriate icons to represent the information. We also extend some of our concepts to asymmetric tensor data.

First, we design icons that emphasize the continuity of the tensor data, overcoming some of the limitations of discrete point icons. A n-dimensional, symmetric tensor field is equivalent to n orthogonal families of smooth and continuous curves that are tangent to the eigenvector fields. For $n = 2$ we generate textures to render these trajectories, and for $n = 3$ we use numerical integration. To fully represent the tensor data, we surround the resulting trajectories by tubular surfaces that represent the transverse eigenvectors—we call these surfaces *hyperstreamlines.* We also define the concept of a solenoidal tensor field, and we show that its hyperstreamlines possess geometric properties similar to the streamlines of solenoidal vector fields.

Then, we analyze the topology of symmetric tensor fields by using a formalism

which is analogous to the phase-space analysis of dynamical systems. As with vector field topology, we derive a set of points and trajectories that embed global information, representing the collective behavior of a continuous distribution of hyperstreamlines. We call the points that underlie the topology of tensor fields *degenerate points,* because the eigenvalues are equal to each other at these points. Depending on the tensor gradients, degenerate points can be of various types that correspond to different local patterns of the eigenvectors. We carry out a mathematical analysis of degenerate points, identifying trisector points, wedge points, nodes, foci, saddle points, dipoles, cusps, saddle-nodes, as well as other, more exotic patterns. We call the trajectories that underlie the topology of tensor fields *separatrices.* They are specific hyperstreamlines that are either limit cycles, or trajectories emanating from degenerate points and lying on the border of hyperbolic sectors.

Separatrices and degenerate points are the basic constituents of tensor field topology but they are not its only determinants. When a tensor field is defined across a surface, the topology of the surface constrains the topology of the tensor field; it limits the number and the nature of the degenerate points. We explore this relation, transposing to tensor fields the Poincaré-Hopf Theorem for vector fields.

Acknowledgements

I am grateful to Professor Lambertus Hesselink for providing researchers with an environment that fosters creativity and for enthusiastically supporting new research ideas. Thanks are due to everyone in Bert's group for making it a pleasurable work environment. I would like to mention Jim Helman, whose work inspired me; Mark Peercy, for insights into graphics and for critical comments about the present manuscript and other publications; Paul Ning, for insights into system administration and for critical comments about various publications; and Yuval Levy, for insights into fluid dynamics. I also greatly profited from exchanges with researchers at NASA Ames, particularly Dr. Daniel Asimov. Tomiko Yoda helped me with semiotics and improved the English of this manuscript.

I would like to express my deepest gratitude to Mrs. Albert Jadot, who funded my first year at Stanford through the Belgian American Educational Foundation. My research was supported by NASA under contracts NAG2-701 and NAG2-911, and also by NSF under grants ECS-8815815 and ECS-9215145.

Finally, I am indebted to Tomiko Yoda for her constant support, and to my parents who enabled me to pursue my education.

Contents

Abstract **iv**

Acknowledgements **vi**

1 Introduction **1**

1.1 Objectives 3

1.1.1 A New Era 4

1.1.2 The Topological Structure of Tensor Fields 5

1.1.3 A Model for Continuous Multivariate Fields 5

1.2 Second-Order Tensor Fields 5

1.3 Framework for Scientific Visualization 8

1.3.1 Icons 9

1.3.2 Attributes of Icons 10

1.4 Overview of Tensor Visualization 12

1.4.1 Overview 14

1.4.2 Contributions 18

1.5 Structure of the Dissertation 21

2 Review of Vector Icons **23**

2.1 Elementary Icons 24

2.1.1 Point Icons 24

2.1.2 Particle Traces, Streaklines, and Streamlines 26

2.1.3 Streamsurfaces 31

2.2 Local Icons 33

2.2.1 Critical Points and Their Glyphs 33
2.2.2 Streamribbons and Streamtubes 38
2.3 Global Icons 40
2.3.1 2-D Vector Field Topology 42
2.3.2 2-D Time-Dependent Vector Field Topology 44
2.3.3 3-D Separated Flows 44
2.4 Chapter Summary 52

3 Elementary Tensor Icons 54
3.1 Continuous Icons versus Point Icons 55
3.2 2-D Symmetric Tensor Fields 59
3.2.1 Texture Generation 59
3.2.2 Trivariate Data Visualization 63
3.3 3-D Symmetric Tensor Fields 65
3.3.1 3-D Hyperstreamlines 65
3.3.2 Correlating Vector and Scalar data 71
3.3.3 Color Coding Schemes 72
3.4 Solenoidal Tensor Fields 75
3.4.1 2-D Solenoidal Tensor Fields 76
3.4.2 3-D Solenoidal Tensor Fields 79
3.5 Asymmetric Tensor Fields 90
3.5.1 Symmetric/Antisymmetric Decomposition 90
3.5.2 Polar Decomposition 92
3.6 Chapter Summary 95

4 Local and Global Tensor Icons 97
4.1 Introduction 97
4.1.1 Investigated Data 98
4.1.2 Degenerate Points 99
4.1.3 Tensor Field Topology 101
4.1.4 Chapter Content 101
4.2 Theory of the Tensor Index 101

4.2.1 Tensor Index of a Jordan Curve 102
4.2.2 Tensor Index at a Degenerate Point 105
4.3 Degenerate Points and Separatrices 108
4.3.1 Sectors and Separatrices 108
4.3.2 The Invariant δ 113
4.3.3 Simple Degenerate Points 117
4.3.4 Multiple Degenerate Points 126
4.3.5 Limit Cycles 139
4.4 Tensor Field Topology 146
4.4.1 Tracking Degenerate Points 147
4.4.2 Correlating Vector and Tensor Data 150
4.4.3 Topological Skeletons 152
4.5 Tensor Topological Rule 157
4.6 Extensions to 3-D Symmetric Tensor Fields 166
4.6.1 Degenerate Points 166
4.6.2 Topological Loci 170
4.7 Chapter Summary 174

5 Conclusions and Future Research 180
5.1 A Look Back 180
5.2 ...and a Look Ahead 183
5.2.1 Visual Issues 183
5.2.2 Physical Issues 184
5.2.3 Mathematical Issues 185

A Smooth Hue Scale 187

B Locating Simple Degenerate Points 193

C Related Publications 196

Bibliography 198

List of Tables

1.1 Vector fields in fluid flows. ρ = mass density, p = pressure, and T = temperature. 2

1.2 Cartesian components of second-order tensor fields in fluid flows. p = pressure, ρ = mass density, v_i and v_j = velocity components, and μ and λ = viscosity coefficients. δ_{ij} is the Kronecker symbol. v_i' and v_j' are velocity fluctuations about the mean, and $< \ldots >$ are averages over time. (a) = asymmetric, (s) = symmetric. 3

1.3 Vector icons to be discussed in Chapter 2 . (c) means object contraction. 11

1.4 Tensor icons to be discussed in Chapters 3 and 4 . (c) means object contraction. Italicized items are icons to be designed in this dissertation. 12

3.1 Behavior of hyperstreamlines in 2-D solenoidal tensor fields. 79

4.1 Rotation of the eigenvectors during a counterclockwise motion around a degenerate point. 110

4.2 Parameters describing the geometry of degenerate points. 111

4.3 Simple degenerate points. α_i is the angle spanned by hyperbolic sectors. 127

4.4 Euler characteristic of generic surfaces. 159

5.1 Vector icons. (c) means object contraction. The stars indicate promising research areas. 181

5.2 Tensor icons. (c) means object contraction. Italicized items show the contributions of this dissertation. The stars indicate promising research areas. 181

List of Figures

1.1 2-D and 3-D symmetric tensor fields. Orthogonal eigenvector fields $\vec{v}_i$ are represented as bidirectional arrows. 6

1.2 Two compressive forces applied to the top surface of a semi-infinite elastic material. 12

1.3 Contour lines of the components of the stress-tensor field induced by two compressive forces. 13

1.4 Contour lines of the tensor field in Figure 1.3 , after a 45° rotation of the coordinate axes. 15

1.5 Ellipses with principal axes representing the two eigenvectors $\vec{v}_i$ of an elastic stress-tensor field. 16

1.6 Textures representing an elastic stress tensor induced by two compressive forces; (top): most compressive (minor) eigenvector; (bottom): least compressive (major) eigenvector. Color encodes the longitudinal eigenvalue according to color scale 2 of Figure A.3 (Appendix A). . . 17

1.7 Topological skeletons representing of an elastic stress-tensor field induced by two compressive forces. Minor (top) and major (bottom) eigenvectors. 19

1.8 Correlation of the stress-tensor field (topological lines) with the displacement field (texture). Color encodes the magnitude of the local displacement, according to color scale 2 of Figure A.3 (Appendix A). 20

2.1 Arrows depicting the velocity field in the flow past a cylinder. Blue, green, yellow, and red correspond to increasing kinetic energy density. 25

2.2 Streamlines of the steady flow in Figure 2.1 . Color maps kinetic energy density according to scale 1 in Figure A.3 (Appendix A). 28

2.3 Same streamlines as in Figure 2.2 , but rendered as thin tubes with finite cross-section. 29

2.4 Streamsurface in the flow around a post. 32

2.5 2-D critical points. R1 and R2 denote the real parts of the eigenvalues of **J**, I1 and I2 the imaginary parts. 34

2.6 3-D saddle/saddle/node. 36

2.7 Local characterization of the velocity field in Figure 2.1 37

2.8 Streamribbons near the surface of the body in Figure 2.1 . The twist of the ribbons encodes streamwise vorticity, and their width reflects cross-flow divergence. 39

2.9 Streamtube colored with air pressure, visualizing the flow in a room (top); comparison of a streamline, a streamribbon, and a streamtube (bottom). 41

2.10 Topological representation of the 2-D flow past a circular cylinder at two different time steps. The flow is coming from the left; *at* = attachment point; *de* = detachment point; *sp* = saddle point; *ce* = center. . 43

2.11 Topological surfaces depicting the time evolution of the 2-D flow past a circular cylinder. Time increases from back to front. 45

2.12 Skin-friction topology on the upper hemisphere of the cylinder in Figure 2.1 . *Sa, Ss* = saddles of attachment and separation; *Na, Ns* = nodes of attachment and separation; *Fa, Fs* = spiral nodes of attachement and separation. 47

2.13 Streamsurfaces depicting separation topology. 49

2.14 Contour lines of helicity density H_d (red/white = right-handed vortices; blue/black = left-handed vortices), together with skin-friction topology (blue and yellow lines) and vortex cores (magenta lines). 51

3.1 Point icons of 2-D and 3-D symmetric tensor fields. 55

3.2 Representation of a continuous and symmetric tensor field as orthogonal families of smooth, non-intersecting curves for the case $n = 2$. This analogy holds in regions that do not comprise degenerate points. . . . 58
3.3 Reynolds-stress tensor in a 2-D flow past a circular cylinder; major (top) and minor (bottom) eigenvector fields. Color scale 2 of Figure A.3 (Appendix A) is used to encode the longitudinal eigenvalue. 62
3.4 Trivariate data visualization to fully represent the Reynolds-stress tensor field corresponding to Figure 3.3 64
3.5 Stress tensor induced by two compressive forces; hyperstreamline trajectories. Color scale 1 of Figure A.3 is used. 66
3.6 Stress tensor induced by two compressive forces; minor tubes, medium and major helices. Color scale 1 of Figure A.3 is used. 68
3.7 Four different stages of a minor tube in an elastic stress-tensor field. Color scale 1 of Figure A.3 (Appendix A) is used. 70
3.8 Reversible momentum flux density tensor in the flow past a hemisphere cylinder. Color scale 1 of Figure A.3 is used. 73
3.9 The minor tube of Figure 3.7 colored as a function of the normal stress. Color scale 2 of Figure A.3 is used. 74
3.10 Sign of the geometric factor K_{lt} for 2-D solenoidal tensor fields. . . . 77
3.11 Major (left) and minor (right) eigenvectors of a solenoidal tensor field. Color encodes the longitudinal eigenvalue. Increasing values correspond to color shifts from blue to green, yellow, orange, and red (color scale 2 of Figure A.3). 78
3.12 Sign of the geometric factors K_{lt_i}, $i = 1, 2$. 80
3.13 Rotation of the orthonormal eigenvector basis. 85
3.14 Major tubes illustrating the solenoidal property of the momentum-flux-density tensor in one region of the flow past a hemisphere cylinder. Color scale 1 of Figure A.3 is used. 87
3.15 Close view of the sudden divergence of minor hyperstreamlines on one side of the plane of symmetry in Figure 3.6 . Color scale 1 of Figure A.3 is used. 88

3.16 Rake of major tubes of the momentum-flux-density tensor in the flow past an ogive cylinder. Color scale 1 of Figure A.3 is used. 89

3.17 Examples of line icons for 3-D asymmetric tensor fields. Symmetric/antisymmetric decomposition (top) and polar decomposition (bottom). Color scales 1 and 2 of Figure A.3 are used for tubes and ribbons, respectively. 91

3.18 Polar Decomposition of asymmetric data. 93

4.1 The two orthogonal eigenvector fields $\vec{v}_i$, represented as bidirectional arrows. 98

4.2 Away from degenerate points, continuous and symmetric tensor fields are diffeomorphic to constant data. 100

4.3 a: Jordan curve; b and c: non-Jordan curves. 102

4.4 Illustration of Theorem 4 104

4.5 Illustration of Theorem 5 106

4.6 Hyperbolic (α_i), parabolic (β_j), and elliptic (γ_k) sectors at a degenerate point. 109

4.7 Simple degenerate points. $\delta = ad - bc \neq 0$ and $I_{\mathbf{T}}$ = tensor index. Trisector ($\delta < 0$) and wedge ($\delta > 0$) points. Trajectories s_k are separatrices. 121

4.8 Textures representing the two eigenvector fields in the vicinity of a trisector point (top) and a wedge point (bottom). Color encodes the difference between the two eigenvalues. 122

4.9 Illustration of Theorem 11 123

4.10 Polar components of $\mathbf{T}$. 124

4.11 Combination of wedges and trisectors looking like a center in the far field. 128

4.12 Merging degenerate points. δ = invariant of Equation 4.13 , $I_{\mathbf{T}}$ = resulting tensor index. Each column represents one eigenvector field. . 129

4.13 Dipole created by four merging wedge points. 130

4.14 Merging wedge/trisector pairs inducing a cusp (top) and saddle-node (bottom). Each pattern appears simultaneously in one of the two eigenvector fields. 130
4.15 Textures representing the eigenvectors of $\mathbf{T}_1(\vec{x})$. The tensor exhibits two foci at the origin. Color encodes the square root of the difference between the eigenvalues according to color scale 2 of Figure A.3 . . . 135
4.16 Textures representing the eigenvectors of $\mathbf{T}_2(\vec{x})$. The tensor exhibits a center and a star-node at the origin. Color encodes the square root of the difference between the eigenvalues according to color scale 2 of Figure A.3 136
4.17 Textures representing the eigenvectors of tensor field $\mathbf{T}_3(\vec{x})$. The tensor exhibits two saddle points at the origin. Superimposed are the separatrices. Color encodes the square root of the difference between the eigenvalues according to color scale 2 of Figure A.3 138
4.18 Textures representing the eigenvector fields of a node of $\mathbf{T}_4(\vec{x})$. The tensor exhibits a node and a center at the origin. Color encodes the square root of difference between the eigenvalues according to color scale 2 of Figure A.3 140
4.19 Textures representing the eigenvector fields of $\mathbf{T}_5(\vec{x})$. The tensor exhibits a multiple degenerate point with $n_h = 2$ hyperbolic sectors. Superimposed are the separatrices. Color encodes the fourth root of the difference between the eigenvalues according to color scale 2 of Figure A.3 141
4.20 a: two limit cycles of a continuous tensor field; b and c: closed trajectories that are not limit cycles after Definition 12 142
4.21 Textures representing the major eigenvector field (traction) of Reynolds stresses in a 2-D flow past a cylinder. Superimposed are two limit cycles. White dots are trisector points and red dots are wedge points. Color encodes the magnitude of the longitudinal Reynolds stress according to color scale 2 of Figure A.3 144
4.22 Attractor cycles in 3-D tensor fields. 146

4.23 Frames of Video Clip 1 showing the flow at two representative time steps. Color encodes velocity magnitude from fast (red) to slow (blue), according to color scale 2 of Figure A.3 148
4.24 Frames of Video Clips 2 and 3 showing the motion of degenerate points of the stress-tensor field over time. Wedge points are represented as black dots and trisectors are white dots. Color encodes the most compressive eigenvalue, λ_2, from very compressive (red), to mildly compressive (orange, yellow, green), to little compressive (blue). We use color scale 2 of Figure A.3 149
4.25 Spatiotemporal trajectories of degenerate points in the stress-tensor field. Time increases from front to back. Red spheres = wedges, green spheres = trisectors. M and C indicate merging and creation of wedge-trisector pairs, respectively. 151
4.26 A frame of Video Clip 4 showing the correlation between the velocity field (moving texture) and the degenerate points of the stress tensor. Color encodes the most compressive stresses, from very compressive (red), to mildly compressive (orange, yellow, green), to little compressive (blue). Red dots = wedges, white dots = trisectors. 153
4.27 A frame of Video Clip 5 showing the instantaneous topology of the most compressive eigenvector $\vec{v}_2$. Color encodes λ_2, from very compressive (red), to mildly compressive (orange, yellow, green), to little compressive (blue). W = wedge points, T = trisectors. 155
4.28 Two consecutive frames showing a topological transition of the stress-tensor field. 156
4.29 Trivariate data visualization to fully represent the stress-tensor field. The texture and the topological skeletons show the most compressive eigenvector $\vec{v}_2$. Color encodes λ_2, from very compressive (red), to mildly compressive (orange, yellow, green), to little compressive (blue). Red dots are wedge points and white dots are trisectors. The elevation of the surface encodes the least compressive eigenvalue, λ_1. 158
4.30 A tensor field defined across an orientable surface $\mathbf{M}$. 160

4.31 A tensor field tangent to a sphere **S**. T's are trisectors and W's are wedge points. 162
4.32 Calculation of the tensor index of a surface of genus $g(\mathbf{M})$. 163
4.33 Illustration of the tensor topological rule for a torus and a sphere. . . 165
4.34 Three-dimensional wedge point and trisector around a degenerate point where $\lambda_1 = \lambda_2 > \lambda_3$. 168
4.35 A trisector point that deflects minor hyperstreamline trajectories of the elastic stress tensor in Figure 3.6 . Color encodes the longitudinal eigenvalue according to color scale 1 in Figure A.3 169
4.36 Topological loci of the elastic stress tensor in Figure 3.6 173
4.37 Stress tensor in the flow past a hemisphere cylinder. Color scale 1 of Figure A.3 is used. 175
4.38 Viscous-stress tensor in the flow past a hemisphere cylinder. Color scale 1 of Figure A.3 is used. 176

A.1 A line segment and a circle as color paths. 188
A.2 Color path in CIE 1976 $L^*u^*v^*$ color space. 190
A.3 Smooth color scale for encoding univariate variables. 191

B.1 A grid cell. 194

Chapter 1

Introduction

Visualizing data involves using abstract pictures to show numbers. Surprisingly, this is a relatively new way of presenting information; it was not until well into the eighteenth century, long after René Descartes and his discovery of Cartesian coordinates, that designers fully grasped the advantages of using abstract graphics to display information. William Playfair (1759-1823), a Scottish political economist, is acclaimed as the inventor of modern graphical designs. In his book *The Commercial and Political Atlas* (London, 1786), Playfair used for the first time x-y plots rather than tables to visualize time-series data. He described the superiority of graphics over tables by noting that "on inspecting any one of these Charts attentively, a sufficiently distinct impression will be made, to remain unimpaired for a considerable time, and the idea which does remain will be simple and complete [...]" (Reference [1]).

Various authors since Playfair have used a wealth of ingenuity and imagination to make the graphical depiction of information as effective and aesthetic as possible. A particularly challenging problem was, and still is, to find efficient ways of rendering multivariate information on a simple sheet of paper—the two-dimensional world of *Flatland* illustrated in Edwin Abbott's book (Reference [2]). Multivariate data typically involve multiple information fields that eventually extend across multidimensional domains, such as subsets of $\mathbf{R}^n$ where $n \geq 1$. Many visualization pioneers designed creative solutions to represent such data, partly overcoming *Flatland*'s low dimensionality. For example, a famous map by the French engineer Charles Joseph

$\vec{v}$	velocity
$\vec{m} = \rho\vec{v}$	momentum density
$\vec{\omega} = \vec{\nabla} \times \vec{v}$	vorticity
$\vec{g} = \vec{\nabla} f$	scalar gradient ($f = \rho, p, T$, etc.)

Table 1.1: Vector fields in fluid flows. ρ = mass density, p = pressure, and T = temperature.

Minard (1781-1870) portrays the terrible fate of Napoleon's army in Russia by simultaneously showing the evolution in time ($n = 1$) of six independent variables—freezing temperatures on the Russian front, French army size, location, and direction of movement. Another landmark idea was Chernoff's use of cartoon faces (Reference [3]) to represent multivariate data across a two-dimensional domain ($n = 2$). Chernoff assumed that our well trained abilities at recognizing facial expressions would help us to cluster the data. In their seminal work, Edward R. Tufte (References [1, 4]) and Jacques Bertin (Reference [5, 6]) discuss many more visualization examples, drawing a set of design principles that lead to accurate, effective, and aesthetic graphics—i.e., visualization excellence.

As today's computer technology enables researchers to generate increasingly large and complex data sets, there is a greater need for newer, faster, and more powerful visualization technologies. Fortunately, computers do not only create needs. They also provide solutions: by substituting machine computation and computer graphics for conscious visual processing, computers help us to overcome our inherent cognitive limitations. This motivated the National Science Foundation to initiate in 1987 a multidisciplinary effort aimed at developing new computer technologies to visualize scientific data (Reference [7]). *Scientific visualization* emerged as a new discipline.

Many scientific data are scalar, vector, or second-order tensor fields defined across n-dimensional subsets of $\mathbf{R}^n$. (Typically $n = 1$ to 4.) Such data are particularly abundant in fluid flow physics, and a few examples of vector and tensor fields in fluid flows are listed in Tables 1.1 and 1.2, respectively.

There are already effective ways of communicating scalar information, such as isosurfaces (Reference [8]) or volume rendering (References [9, 10, 11]). Vector and

$J_{ij} = \frac{\partial v_i}{\partial x_j}$	velocity gradient (a)
$\epsilon_{ij} = J_{ij} + J_{ji}$	rate-of-strain tensor (s)
$\sigma'_{ij} = \mu\epsilon_{ij} + \lambda\delta_{ij}\frac{\partial v_k}{\partial x_k}$	viscous stress tensor (s)
$\sigma_{ij} = -p\delta_{ij} + \sigma'_{ij}$	stress tensor (s)
$\Pi^r_{ij} = p\delta_{ij} + \rho v_i v_j$	reversible momentum-flux-density tensor (s)
$\Pi_{ij} = \Pi^r_{ij} - \sigma'_{ij}$	momentum-flux-density tensor (s)
$R_{ij} = \rho < v'_i v'_j >$	Reynolds-stress tensor (s)

Table 1.2: Cartesian components of second-order tensor fields in fluid flows. p = pressure, ρ = mass density, v_i and v_j = velocity components, and μ and λ = viscosity coefficients. δ_{ij} is the Kronecker symbol. v'_i and v'_j are velocity fluctuations about the mean, and $< \ldots >$ are averages over time. (a) = asymmetric, (s) = symmetric.

second-order tensor fields, however, are more complex; they embed as much information as n and n^2 independent scalar fields, respectively. And because computer screens are still *Flatland,* the basic problems have not changed since Playfair and Minard: How are we to represent large amounts of multivariate information on a two-dimensional medium, in a form that is suitable to the human visual system?

1.1 Objectives

In this dissertation, we design representations of continuous, second-order tensor fields and show connections with vector visualization techniques. We decided to undertake this work after noticing that, although many visualization researchers stressed the need for tensor visualization schemes (References [12] [13] [14] [15] [16]), actual attempts were scarce and superficial. Clearly, no one really knew what tensor fields looked like.

Our main objectives are as follows:

- to start an era of tensor visualization,
- to show that tensor fields contain simple topological structures, and
- to serve as a model for the visualization of other continuous multivariate data.

1.1.1 A New Era

Much research effort is being devoted to the visualization of vector fields. Not much has been undertaken, however, for second-order tensor fields. This is to be expected; after all, tensor data are more complex and somewhat more "abstract" that their vector counterparts. But this is also surprising.

Second-order tensor fields are central to many areas of physics. For example, most of general relativity is based on tensor fields. The mechanical properties of solids are expressed mainly as second-order tensor data—such as stresses and strains. In fluid flows, stresses, strain rate, and Reynolds stresses are all tensor quantities (Table 1.2). Even the momentum transfers are expressed as second-order tensor fields: the steady-state Euler's equations, which govern ideal gas flows, can be simply written as

$$\sum_i \frac{\partial \Pi^r_{ij}}{\partial x_i} = 0 \tag{1.1}$$

where the only quantity involved is Π^r_{ij} (Table 1.2), a tensor field that represents reversible momentum transfers (transfers due to the mechanical transport of fluid particles or to the pressure forces). Likewise, the steady-state Navier-Stokes equations, which govern viscous flows, are equivalent to

$$\sum_i \frac{\partial \Pi_{ij}}{\partial x_i} = 0 \tag{1.2}$$

Again, there is only one quantity involved, the second-order tensor field Π_{ij} (Table 1.2) which accounts for both reversible and irreversible momentum transfers.

Turbulence modeling is another area that calls for tensor visualization schemes. The ability to plot tensor fields and to compare their topological structure is, indeed, crucial to validate (or invalidate) widely used turbulence models such as the *eddy-viscosity model* (Reference [17]).[1]

As shown by these examples, second-order tensor fields occur in many different areas. Visualizing them can contribute to improving our understanding of various physical processes. This dissertation fills the present lack of visualization techniques for second-order tensor fields and discusses their geometric structure.

[1] The eddy-viscosity model assumes that the Reynolds-stress tensor is proportional to the rate-of-strain tensor—an assumption which can be verified only by comparing the topology of these two tensor fields (Table 1.2).

1.1.2 The Topological Structure of Tensor Fields

Our second objective is to show that second-order tensor fields contain simple topological structures. Because this work is, to our knowledge, the first topological study of second-order tensor fields, we adopt a general rather than case-specific approach with the hope of being as widely relevant as possible. We would like to make three points:

- A continuous tensor field is a continuum and must be visualized as such. In other words, continuous tensor fields are best represented by using continuous rather that discrete icons, by emphasizing the underlying continuity of the data rather than cluttering the display with discrete, multidimensional information.

- Tensor fields present simple topological structures that outline their geometry. This visual simplicity dramatically contrasts with the mathematical complexity of tensor algebra.

- Data compression. By displaying the key topological features of tensor data, we create simple depictions of complex multivariate information while achieving significant data compression.

1.1.3 A Model for Continuous Multivariate Fields

We hope that this dissertation will serve as a model for the visualization of other continuous multivariate data fields. We show strong similarities between challenges and solutions in vector and tensor field visualization, and these similarities can serve as guidelines for future research efforts on similar problems.

1.2 Second-Order Tensor Fields

In this section, we provide explicit mathematical definitions of the data to be investigated in the subsequent chapters.

Definition 1 (Second-Order Tensor Field) *Let $\mathcal{L}(X,Y)$ be the set of all the linear transformations of the vector space X into the vector space Y, and let E be an*

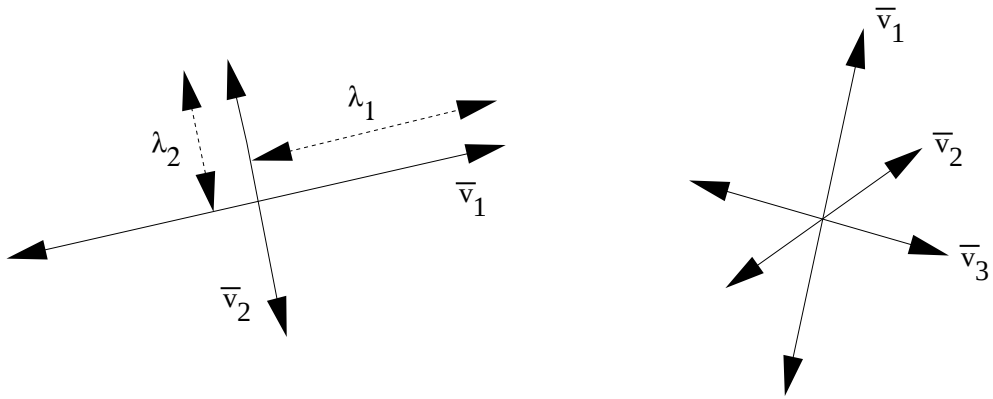

Figure 1.1: 2-D and 3-D symmetric tensor fields. Orthogonal eigenvector fields $\vec{v}_i$ are represented as bidirectional arrows.

open subset of $\mathbf{R}^n$*. A second-order tensor field* $\mathbf{T}(\vec{x})$ *defined across* E *is a mapping* $\mathbf{T} : E \to \mathcal{L}(\mathbf{R}^m, \mathbf{R}^m)$ *that associates to each vector* $\vec{x}$ *of* E *a linear transformation of* $\mathbf{R}^m$ *into itself. If* $\mathbf{R}^m$ *is referenced by a Cartesian coordinate system,* $\mathbf{T}(\vec{x})$ *can be represented by* m^2 *Cartesian components* $T_{ij}(\vec{x})$*,* $i, j = 1, \ldots, m$*, that transform according to*

$$T'_{ij} = \sum_{p,q=1}^{m} \beta_{ip}\beta_{jq}T_{pq} \tag{1.3}$$

under an orthonormal transformation $\beta = \{\beta_{ij}\}$ *of the coordinate axes.*

From now on we refer to second-order tensor fields simply as "tensor fields." We also confine our study to the case $n = m = 2$ or 3. That is, we discuss 2×2 tensor fields defined across subsets of $\mathbf{R}^2$, and 3×3 tensor fields defined across subsets of $\mathbf{R}^3$. Explicit Cartesian components of these tensor fields are as follows:

- 2-D symmetric tensor fields

$$\mathbf{T}(\vec{x}) = \mathbf{T}(x, y) = \begin{pmatrix} T_{11}(x, y) & T_{12}(x, y) \\ T_{12}(x, y) & T_{22}(x, y) \end{pmatrix} \tag{1.4}$$

These data are fully equivalent to two orthogonal eigenvector fields

$$\vec{v}_i(\vec{x}) = \lambda_i(\vec{x})\vec{e}_i(\vec{x}) \tag{1.5}$$

where $i = 1, 2$. $\lambda_i(\vec{x})$ $(i = 1, 2)$ are the eigenvalues and $\vec{e}_i(\vec{x})$ $(i = 1, 2)$ the corresponding unit eigenvectors. Both eigenvalues and eigenvectors are real. We represent $\vec{v}_1$ and $\vec{v}_2$ in Figure 1.1 (left) as bidirectional arrows because of the sign ambiguity of the eigenvectors. By convention, we order eigenvalues as $\lambda_1(\vec{x}) \geq \lambda_2(\vec{x})$, and because of this particular ordering, we refer to $\vec{v}_1$ and $\vec{v}_2$ as the "major" and "minor" eigenvectors, respectively.

- 3-D symmetric tensor fields

$$\mathbf{T}(\vec{x}) = \mathbf{T}(x, y, z) = \begin{pmatrix} T_{11}(x,y,z) & T_{12}(x,y,z) & T_{13}(x,y,z) \\ T_{12}(x,y,z) & T_{22}(x,y,z) & T_{23}(x,y,z) \\ T_{13}(x,y,z) & T_{23}(x,y,z) & T_{33}(x,y,z) \end{pmatrix} \tag{1.6}$$

These data are equivalent to three orthogonal eigenvector fields

$$\vec{v}_i(\vec{x}) = \lambda_i(\vec{x})\vec{e}_i(\vec{x}) \tag{1.7}$$

where $i = 1, 2, 3$. Both eigenvalues and eigenvectors are real. The eigenvectors $\vec{v}_i(\vec{x})$ are represented as bidirectional arrows in Figure 1.1 (right). Again, we order eigenvalues as $\lambda_1(\vec{x}) \geq \lambda_2(\vec{x}) \geq \lambda_3(\vec{x})$ and we refer to $\vec{v}_1$, $\vec{v}_2$, and $\vec{v}_3$, as the "major," "medium," and "minor" eigenvectors, respectively.

- 3-D asymmetric tensor fields

$$\mathbf{T}(\vec{x}) = \mathbf{T}(x, y, z) = \begin{pmatrix} T_{11}(x,y,z) & T_{12}(x,y,z) & T_{13}(x,y,z) \\ T_{21}(x,y,z) & T_{22}(x,y,z) & T_{23}(x,y,z) \\ T_{31}(x,y,z) & T_{32}(x,y,z) & T_{33}(x,y,z) \end{pmatrix} \tag{1.8}$$

At least one of the following conditions is met: $T_{12}(x, y, z) \neq T_{21}(x, y, z)$, $T_{13}(x, y, z) \neq T_{31}(x, y, z)$, or $T_{23}(x, y, z) \neq T_{32}(x, y, z)$. This case is complicated by the possible occurrence of complex eigenvalues and complex, non-orthogonal eigenvectors.

Visualizing symmetric tensor fields is an important problem per se. It is also a necessary step in order to visualize more complex asymmetric tensor data. Indeed, an asymmetric tensor field $\mathbf{T}(\vec{x})$ can always be decomposed as

$$\mathbf{T}(\vec{x}) = \mathbf{S}(\vec{x}) + \mathbf{A}(\vec{x})$$

or as

$$\mathbf{T}(\vec{x}) = \mathbf{S}(\vec{x})\mathbf{A}(\vec{x})$$

where $\mathbf{S}(\vec{x})$ is a symmetric tensor field and $\mathbf{A}(\vec{x})$ is an antisymmetric tensor field. One can show that $\mathbf{A}(\vec{x})$ is equivalent to a vector field. Thus, by visualizing and extracting the topology of vector and symmetric tensor fields, one can also display general asymmetric tensor data. (More on this topic in Section 3.5.)

1.3 Framework for Scientific Visualization

Scientific visualization is a new discipline and the correlations between various techniques are ill-defined, mainly due to the lack of a conceptual model for thinking about multivariate data visualization (Reference [18]). However, the problem of representation tackled by scientific visualization—creating a mental image of the data—is hardly a new subject; its theoretical and practical implications have been studied extensively in various disciplines such as logic, linguistics, psychology, and sociology.

Visualization processes transform raw experimental or simulated data into a form suitable for human understanding; they can take on many different forms, depending on the nature of the original data and the information that is to be extracted. However, visualization processes can be generally subdivided into three main stages: data preprocessing, visualization mapping, and rendering (References [12, 13]).

Data preprocessing involves diverse operations, such as interpolating irregular data to a regular grid, filtering and smoothing raw data, or deriving functions of measured or simulated quantities. Visualization mapping—in many ways the most crucial and least automated stage of the visualization process—consists of designing an adequate representation of the filtered data, an *icon*, which conveys efficiently the relevant information. This often involves first deciding what aspects of the data carry

meaningful information and then extracting data features such as singularities, vortex cores, etc. Finally, icons must be rendered in order to communicate the information.

1.3.1 Icons

Icons in scientific visualization are often defined as geometric objects that encode the data at a given point either through geometric characteristics, such as lengths or angles, or through other visible attributes, such as color or opacity (Reference [19]). In this dissertation however, an "icon" is a more general concept that relates to the semiotics of data visualization. Visualization mappings construct intelligible representations of the data by means of *signs.* That is to say, the data are expressed semiologically by constituting a relation between an *object* (data) and its *representation.*

Signs, according to the logician C.S. Peirce, relate to the object in three different ways—as an icon, an index, or a symbol (Reference [20]):

- an icon is based on a resemblance between the object and its representation. It is not, however, affected by the object and has no "dynamic" connection to it. Examples are chemical diagrams that represent molecules. On the other hand,

- an index "is a sign which refers to the object that it denotes by virtue of being really affected by that object." Typical examples include a clock indicating the time of the day and the photograph of an object. In fact, an index is essentially causal whereas an icon is mainly mimetic (Reference [21]). Finally,

- a symbol relates to the object by virtue of an arbitrary convention. For example, the correspondence between the shape of letters in the roman alphabet and their sound is largely arbitrary.

In order to characterize the nature of signs used in scientific visualization, consider for example representing a vector at a given point in space by an arrow. The arrow in itself is an icon; it has qualities in common with the data, such as direction and length. However, for the visualization mapping to be useful, the orientation and length of the arrow must be determined by the data. In other words, the representation is indexical,

based on a causal—rather than mimetic or arbitrary—relation between the arrow and the data. This index, it should be remembered, also involves an icon that embodies the information.

Many more examples of such combined signs are discussed in the dissertation (Tables 1.3 and 1.4). For simplicity, we conform to the prevailing usage of the term "icon," but it should be kept in mind that "icons" here are in fact "indices-involving-icon" in respect to their semiological functions. The use of these complex signs is a common property shared by diverse scientific visualization systems. It helps to distinguish the discipline from other applications of computer graphics which usually produce pure icons—as in architectural design or photorealistic studies.

1.3.2 Attributes of Icons

We can derive important features of visualization mappings from the attributes of the associated icons—object, spatial domain, and embedded information level:

- Object. Icons are characterized by the object they represent: scalar, vector, or tensor data. Object contraction consists in simplifying the visualization mapping by displaying derived data of lower multivariability—such as representing a vector field by its scalar magnitude. Object contraction implies a loss of information which is compensated, however, by a considerable simplification of the visualization mapping.

- Spatial domain. Icons represent their object across a spatial domain. An arrow, for example, displays vector information at a single point. Overall, there are point, line, surface, and volume icons.

- Information level. Perhaps the most fundamental attribute of icons, the information level embedded in the representation is elementary, local, or global.[2] Elementary icons represent their object strictly across the extent of their spatial domain (point, line, etc.) For example, an arrow is an elementary point

[2]Embedded information levels correspond closely to those suggested by Bertin (Reference [5, 6]) in his work on the semiology of graphics, and were used more recently by Robertson (Reference [22]) in choosing an adequate methodology for representing 2-D bivariate data.

Spatial Domain	Embedded Information		
	Elementary	Local	Global
Point	arrows wedges hedgehogs	critical-point glyphs	
Line	streamlines streaklines particle traces	streamribbons streamtubes	vortex cores
Surface	streamsurfaces		2-D vector topology
Volume			skin-friction topology and separation surface, helicity density (c), or vortex cores

Table 1.3: Vector icons to be discussed in Chapter 2. (c) means object contraction.

vector icon. On the other hand, local icons represent, in addition to elementary information, a local distribution of the values of the data around the spatial domain. Practically, this means that local icons display, at least partially, data gradients—which are scalar, vector, or tensor gradients. Finally, global icons show the structure of the complete data field. Global icons of multivariate data are typically obtained by feature extraction. What makes them global is therefore problem-specific since it requires those parts of the data that carry structural information to be distinguished from those that can be neglected. Designing global icons for data visualization is a complex but worthwhile endeavor. Because they represent multivariate information by means of a few carefully selected points, lines, or surfaces, global icons result in significant data compression.

Table 1.3 lists various vector icons to be discussed in Chapter 2. Table 1.4 summarizes tensor icons to be designed in Chapters 3 and 4.[3]

[3]Vector gradients are tensors, so local vector icons display elementary tensor information. However, we do not assimilate local vector icons to elementary tensor icons because some attributes of local vector icons, such as the position of critical-point glyphs or the trajectory of streamribbons and streamtubes, are determined by a vector field, not a tensor field. Tensor icons are able to represent

Spatial Domain	Embedded Information		
	Elementary	Local	Global
Point	ellipsoids tensor glyphs	*degenerate points*	
Line	trajectories (c) *hyperstreamlines*		
Surface			*2-D tensor topology*
Volume			*3-D topological loci*

Table 1.4: Tensor icons to be discussed in Chapters 3 and 4. (c) means object contraction. Italicized items are icons to be designed in this dissertation.

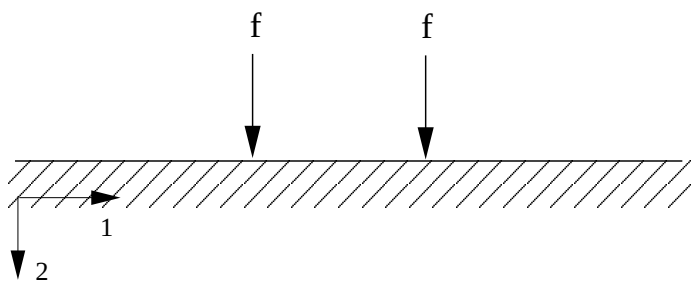

Figure 1.2: Two compressive forces applied to the top surface of a semi-infinite elastic material.

1.4 Overview of Tensor Visualization

In this section, we present an overview of our work by means of a simple example of elasticity. This will explain how we designed our specific visualization mappings, while illustrating the objectives stated above. The example consists of the elastic stress-tensor in a material. These data are fairly simple, but they contain some of the basic features that are encountered in more complex tensor fields. The geometry of the problem is shown in Figure 1.2: two compressive forces are applied on the edge of a semi-infinite plane, inducing elastic stresses in the material.[4]

any tensor data, including those that are not vector gradients.

[4]The data is a two-dimensional cut of a three-dimensional tensor field. Poisson modulus is 0.25.

Figure 1.3: Contour lines of the components of the stress-tensor field induced by two compressive forces.

1.4.1 Overview

Tensor fields are usually visualized by drawing contour lines of individual components, as in Figure 1.3. Although valuable information is represented, these images suffer from three significant limitations. First, they do not teach us much about the structure of the tensor field. Second, three plots are necessary to represent the tensor field. (And in the case of 3-D data, we need six or nine of these plots.) Third, the displayed information depends critically on the orientation of the coordinate axes. For example, Figure 1.4 shows the same data as Figure 1.3, but after rotating the coordinate axes by 45°. Clearly, there is not much in common between the two figures, apart from the fact that in each case tensor components are large in the area where forces are applied. Of course, with such a simple geometry, it is only natural to orient coordinate axes as in Figure 1.2. (This leads to the set of contour lines in Figure 1.3.) But in more complex settings such as tensor fields in fluid flows, there are no particular reasons for privileging a specific orientation of the coordinate axes. Drawing contour lines is then not a suitable representation of tensor data; the information embedded in individual tensor components is not only partial, it also varies with the orientation of the coordinate axes (Equation 1.3).

How are we, then, to represent a tensor field in a way that is invariant under rotation of the coordinate axes? Figure 1.5 shows one possibility. Ellipses represent the two eigenvector fields $\vec{v}_i$ (Figure 1.1—left) at coarsely-spaced points. (The ellipses' principal directions lie along the eigenvectors $\vec{v}_i$.) The advantage of doing so lies in the fact that the displayed information remains invariant upon rotation of the coordinate axes. Ellipses, however, occupy a lot of screen space and they tend to produce visual clutter. This is even more critical when we visualize three-dimensional tensor fields by using ellipsoids. To avoid visual clutter, the density of displayed ellipsoids must be kept so low, that interpolating the data at intermediate points becomes difficult, if possible at all. The tensor field may be continuous, but ellipses or ellipsoids merely render the data at discrete, coarsely-spaced points.

The continuity of tensor components causes the eigenvector fields $\vec{v}_i$ to be continuous at most points. Thus, we can generate textures (References [23, 24]), such

Figure 1.4: Contour lines of the tensor field in Figure 1.3, after a 45° rotation of the coordinate axes.

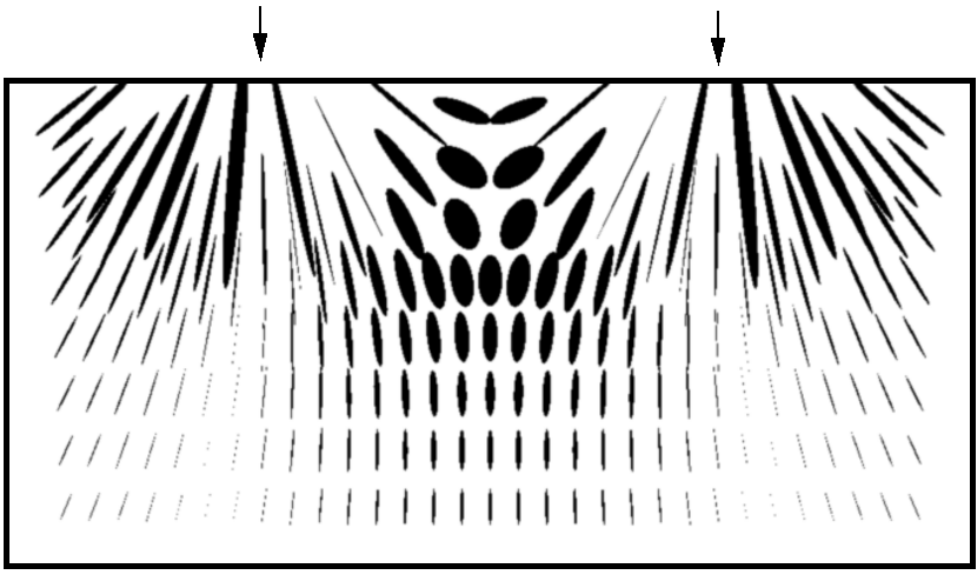

Figure 1.5: Ellipses with principal axes representing the two eigenvectors $\vec{v}_i$ of an elastic stress-tensor field.

as Figure 1.6, which represent the eigenvector fields in a continuous manner. Figure 1.6 (top) shows the minor eigenvector $\vec{v}_2$: the most compressive force in the material; and Figure 1.6 (bottom) shows the major eigenvector $\vec{v}_1$: the least compressive force. Color encodes the longitudinal eigenvalue, from highly compressive (red), to mildly compressive (orange, yellow, green), and to little compressive or even tensile in the case of $\vec{v}_1$ (blue). Clearly, the representation in Figure 1.6 is continuous and invariant under rotation of the coordinate axes.

The texture lines in Figure 1.6 are known in mechanics as "trajectories of the principal stresses." We call them "hyperstreamline trajectories," for consistency with the terms used in our design of 3-D tensor icons in Chapter 3. These trajectories show the way forces are transmitted in the elastic material. They can be visualized experimentally by using photoelasticity techniques (Reference [25]). However, these experimental techniques are applicable only for transparent materials subjected to planar stresses. By using computer visualization, we can generate these trajectories for any numerically defined tensor field—stresses, strains, momentum flux density, etc.

Textures reveal more of the structure of the tensor field than either contour lines

Figure 1.6: Textures representing an elastic stress tensor induced by two compressive forces; (top): most compressive (minor) eigenvector; (bottom): least compressive (major) eigenvector. Color encodes the longitudinal eigenvalue according to color scale 2 of Figure A.3 (Appendix A).

or ellipses. In Figure 1.6 for example, the trajectories never cross each other, except at one point. We call such a point a "degenerate point." We will analyze the eigenvector fields in the vicinity of degenerate points and identify various patterns—such as wedges, nodes, foci, dipoles, etc.

Trajectories that do not meet at degenerate points tend to converge towards a few specific lines that emanate from degenerate points. We call such lines "separatrices." In Figure 1.7, we overlay the separatrices to the texture. This emphasizes the topology of the eigenvector fields. These topological skeletons separate the domain into regions where the eigenvectors are equivalent to uniform fields. From this simple set of lines, one can easily infer the direction of the eigenvectors at any points in the plane.

Topological skeletons depict in a simple manner the geometric structure of tensor data. They can also be used to correlate a tensor field with other data. In Figure 1.8 for example, we correlate elastic stresses and displacements by superimposing the topological skeletons of the stress-tensor on textures of the displacement vector.

The example discussed in this section highlights some of the points to be developed in the course of the dissertation. First, it is better to represent eigenvectors rather than individual tensor components because the latter are tied to a particular orientation of the coordinate axes. Second, visual clutter can be avoided by representing multivariate information continuously rather than discretely. Finally, it is possible to extract topological skeletons that encode schematically the structure of tensor fields. A simple and austere depiction results from which the tensor data can be inferred at any points of the domain.

1.4.2 Contributions

Up to now, there have been very few visualization mappings of tensor fields. Existing techniques, prior to this work, were confined to contour lines of individual components—such as Figures 1.3 and 1.4—and elementary point icons—such as ellipses, ellipsoids (Reference [19]), or tensor glyphs (Reference [12, 13]). We already discussed the drawbacks of using these techniques when visualizing any but the most elementary tensor data.

In 1989, however, R. Dickinson recognized the need to use continuous rather than

Figure 1.7: Topological skeletons representing of an elastic stress-tensor field induced by two compressive forces. Minor (top) and major (bottom) eigenvectors.

Figure 1.8: Correlation of the stress-tensor field (topological lines) with the displacement field (texture). Color encodes the magnitude of the local displacement, according to color scale 2 of Figure A.3 (Appendix A).

discrete mappings (Reference [26]). In this dissertation, we draw on his suggestion, expanding the range of available tensor visualization techniques. We also conduct the first mathematical investigation of the geometry and the topology of second-order tensor fields. The italicized items in Table 1.4 represent icons to be designed in the following chapters. We may summarize the resulting contributions as follows:

- A framework for scientific visualization. This framework allows the classification of many visualization mappings of vector and tensor fields. It develops a unified structure and common vocabularies for the new discipline of scientific visualization. It also points out new questions for future research.

- Textures. A recent major advance in the rendering of 2-D vector fields has been the use of textures rather than numerical integration to represent streamlines. We show that textures are important visualization tools for 2-D tensor data as well.

- Hyperstreamlines. We design new icons that fully represent 3-D symmetric and asymmetric tensor data along continuous trajectories—reducing the problems related to visual clutter.

- Solenoidal tensor fields. We define solenoidal tensor fields and we show that the geometric properties of their hyperstreamlines are in many ways similar to the properties of streamlines of solenoidal vector fields.

- Topology of symmetric tensor fields. We define and analyze the topology of symmetric tensor fields. The tensor topology is based on the notions of degenerate points, hyperstreamline separatrices, and limit cycles. We discuss the geometric structures that are contained in symmetric tensor fields—broadening geometric theories such as the phase-space analysis of dynamical systems.

1.5 Structure of the Dissertation

In Chapter 2, we specifically focus on the state of the art in vector field visualization (Table 1.3). The review, however, raises general issues pertaining to continuous,

multivariate data visualization in general, and lays a framework for our subsequent theory of tensor field visualization (Table 1.4). In Chapter 3, we discuss elementary icons of tensor fields. Our main concern is the design of line icons that overcome the shortcomings of point icons. In Chapter 4, we discuss global tensor icons. We define, analyze, and extract the topology of symmetric tensor fields, introducing new concepts, such as degenerate points and separatrices of a tensor field. In Chapter 5, we summarize our contributions and we outline further research issues. Tensor visualization is in its first phase of development. This dissertation breaks new grounds, but it also raises many new questions to be addressed in the future.

Chapter 2

Review of Vector Icons

In this chapter, we discuss visualization mappings of vector fields. Although we strongly emphasize the case of fluid flow data—where most of the visualization work has been carried out—the concepts to be reviewed here apply to a much wider variety of vector fields.

The purpose of this chapter is threefold. First, we provide an extensive review of recently developed techniques in continuous, multivariate data visualization, prior to our work on tensor fields. Second, the chapter illustrates our claims that continuous, multivariate information is better conveyed by using continuous, rather than discrete, icons; and that problems related to visual clutter can be overcome by a schematic, global depiction of the geometric structure of the data. Third, we fit numerous vector mappings within the framework developed in Chapter 1, while simultaneously emphasizing issues that helped structuring our methodology for tensor-field visualization.

In the following, we review elementary (Section 2.1), local (Section 2.2), and global (Section 2.3) icons of vector fields—all of which were summarized together with their attributes in Table 1.3. It will be seen that elementary icons typically mimic experimental flow visualization techniques, while local and global icons are more abstract representations.

The interested reader can draw many analogies between the material to be discussed in Section 2.1 and Chapter 3, where we design elementary icons of tensor fields. The discussion in Sections 2.2 and 2.3 are also useful introductions to global

representations of tensor fields, to be developed in Chapter 4.

2.1 Elementary Icons

Elementary vector icons represent vector information strictly across their spatial domain—which can be points, lines, or surfaces. First, point icons (and their limitations) are described; then, we discuss line and surface icons that provide a continuous representation of vector fields, therefore improving perception of the data.

2.1.1 Point Icons

The most straightforward vector mapping consists in drawing point icons, such as arrows, at selected locations in the flow—a technique analogous to tufts or vanes used by experimentalists (Reference [27]). Different point icons—such as wedges or bulb-shaped hedgehogs—are sometimes used, but a comparative study shows that simple arrowheads are most efficient at conveying vector information from volumetric data sets (Reference [28]).

Arrows are useful in visualizing 2-D slices of 3-D vector fields, such as cutting planes (Reference [29]); yet, they are impractical when applied to the entire volume. This is because, in order to avoid visual clutter, the density of displayed arrows must be kept very low—in which case, however, it is not possible to comprehend the underlying structure of the vector field by mentally interpolating adjacent arrows, except for very simple objects.

Figure 2.1, for example, shows the velocity field in the flow past a cylinder. For improved perception, color maps kinetic energy density. Although valuable information is represented, the display of merely 4% of the arrows renders the image overly cluttered. Point icons do not represent the intrinsic continuity of the data, and the displayed information is of too poor spatial resolution for elucidating important flow features such as vortices.

Figure 2.1: Arrows depicting the velocity field in the flow past a cylinder. Blue, green, yellow, and red correspond to increasing kinetic energy density.

2.1.2 Particle Traces, Streaklines, and Streamlines

Line icons are more efficient in the sense that they provide a continuous representation of the data, therefore avoiding mental interpolation of point icons. Consider a vector field $\vec{v}(\vec{x}, t)$, where $\vec{x}$ is the position in space and t is the time; in the following we discuss particle traces, streaklines, and streamlines—all of them are line icons that emphasize different aspects of the flow.

Definitions

Particle traces are trajectories traversed by fluid elements over time. They are visualized experimentally by injecting instantaneously a dye or smoke in the flow and by taking a long exposure photograph. Numerically, the trace $\vec{x}(t)$ of a particle originally at position $\vec{x}_o$ is the curve obtained by integrating the equation

$$\frac{d\vec{x}}{dt} = \vec{v}(\vec{x}, t) \tag{2.1}$$

with the initial condition $\vec{x}(0) = \vec{x}_o$. A collection of particle traces, therefore, gives a sense of the complete time evolution of the flow.

The streakline $\vec{x}(\vec{x}_o, t_o)$ passing through the point $\vec{x}_o$ at time t_o is formally defined as the locus, at time t_o, of all the fluid elements that have previously passed through $\vec{x}_o$. Streaklines are obtained experimentally by injecting continuously a non-diffusive tracer (such as hydrogen bubbles) at $\vec{x}_o$, and by taking a short exposure photograph at time t_o. Numerically, streaklines are computed by linking the endpoints of all the trajectories obtained by integrating Equation 2.1 between times t_i and t_o, for every value of t_i such that $0 \leq t_i \leq t_o$, and with initial conditions $\vec{x}(t_i) = \vec{x}_o$. Thus, streaklines at time t_o give information on the past history of the flow.

Finally, streamlines at time t_o are integral curves satisfying

$$\frac{d\vec{x}}{ds} = \vec{v}(\vec{x}, t_o)$$

where t_o is held constant and s is a parameter measuring distance along the path. Streamlines at time t_o are everywhere tangent to the steady flow $\vec{v}(\vec{x}, t_o)$; a collection of such streamlines provides an instantaneous "picture" of the flow at time t_o.

Streamlines in unsteady flows are by nature transitory, but they can be visualized experimentally by injecting a large number of tracer particles in the flow and taking a short-time exposure photograph.

In general, particle traces, streaklines, and streamlines are distinct from each other, but these three families of trajectories coincide in steady flows.

Figure 2.2 represents streamlines of the flow in Figure 2.1. Two pairs of vortices, that are completely hidden in Figure 2.1, are clearly shown in Figure 2.2; when comparing the two figures, it is clear that line icons reveal more of the flow structure than point icons. The same streamlines are rendered as thin tubes with finite cross-section in Figure 2.3. By exploiting our intrinsic ability to use hidden surfaces as perceptual cues, the display in Figure 2.3 improves our perception of the spatial arrangement of the trajectories. As we show in Section 2.3.3, however, important flow features are still hidden in Figure 2.3.

Accuracy and Interactivity

The simulation of the planet Jupiter for the movie "2010" required the computation of approximately 10 million 2-D particle traces that were blended in a moving texture (References [30, 31]). Fortunately, photo-realism is not the goal of scientific visualization, and a more modest number of particles—say a few tens to a few hundreds—suffices for representing fluid flows. Accuracy and interactivity, on the other hand, are primary concerns.

The complexity of most interesting 3-D flows is reflected by intricate trajectories, and integration must be handled with care in order to avoid excessive numerical errors. This is especially relevant in turbulent flows, where the distance between adjacent fluid elements is known to grow exponentially with time (Reference [32]). Any numerical error is therefore dramatically enhanced as integration proceeds.

The integration scheme is an important source of numerical errors. Straightforward integration techniques, like the simple (but fast) Euler explicit scheme, are inadequate. Acceptable results, however, are found using a second-order Runge-Kutta algorithm with step size based on cell dimensions and inverse of vector magnitude (Reference [33]). Higher-order integration techniques, such as fourth-order adaptive

Figure 2.2: Streamlines of the steady flow in Figure 2.1. Color maps kinetic energy density according to scale 1 in Figure A.3 (Appendix A).

Figure 2.3: Same streamlines as in Figure 2.2, but rendered as thin tubes with finite cross-section.

Runge-Kutta, are more accurate, but lead to increased computational loads.

Numerical errors also occur due to vector field interpolation between grid nodes. In fact, simple trilinear interpolation is the main source of errors in turbulent flows (Reference [34]), and higher-order interpolation schemes, such as cubic splines, while being more accurate, impose a strong performance penalty.

Researchers in flow visualization are exploring new hardware configurations that improve both speed and accuracy. An example is distributed particle tracing, where trajectories are computed with a supercomputer and communicated to a front-end workstation handling all the graphics operations (Reference [35]). This configuration, which is being implemented in virtual reality-based systems, such as the Virtual Wind Tunnel (Reference [36]), leads to speedups of an overall factor of 7 during typical visualization sessions.

Recent algorithmic enhancements also improve speed and accuracy. These algorithms exploit the fact that streamlines of 2-D incompressible flows can be computed as contour lines of a stream function (Reference [37]), and that streamlines of 3-D steady flows are intersection curves of the isosurfaces of two stream functions (Reference [38]). In both cases, streamlines are quickly obtained by means of scalar mappings that do not require any error-prone numerical integration of trajectories. An obvious drawback of these methods is the need to precompute the stream functions.

Textures

A recent major improvement, however, was made by adopting a new rendering technique, namely anisotropic textures. By generating textures, we render 2-D streamlines directly, without the need for integrating the vector field (Reference [24]). Among other benefits, textures provide an adequate solution to problems of accuracy. Some texture algorithms, however, use vector integration along short distances—a technique which is supposed to yield improved results (Reference [23]). We discuss textures in more detail in Section 3.2.1, as we use them for visualizing tensor fields.

2.1.3 Streamsurfaces

Because they do not require a mental interpolation of adjacent point icons, streamlines improve the perception of the flow and emphasize the continuity of the vector field. The next logical step is to design surface icons—or streamsurfaces—that are tangent to the vector field at each of their points. Similar to streamlines which are created by advecting one fluid particle, streamsurfaces are obtained by advecting a material line segment—i.e., a front of particles.

Figure 2.4 shows a streamsurface and its polygonal tiling in the flow around a post. The original line segment is made up of six fluid particles and is drawn in black at the bottom of the figure. The algorithm (Reference [39]) models the surface as a collection of ribbons, obtained by building polygonal tilings of pairs of adjacent streamlines. As opposed to earlier algorithms which typically postprocessed previously computed streamlines (References [40, 41]), tiling is performed during advection of the particle front.

As pointed out earlier, adjacent streamlines in divergent flows tend to spread. The algorithm then adaptively adds particles to the advancing front, so oversized polygons can be avoided. A few instances of these "ribbon splitting" events can be seen in Figure 2.4. Also, the front is severed into two independent advancing fronts wherever it becomes too stretched, for example at the boundary of an obstacle. Finally, the tiling of individual ribbons is done with care in order to avoid long and skinny polygons in sheared flows, in which neighboring particles are advected at substantially different speeds.

Generating streamsurfaces does not especially require a polygonal tiling. For example, we can render directly an advected front of "surface particles"—i.e., small facets modeled as points with a normal vector (Reference [42]). Surface particles are shaded according to their normal vector. Then, each particle is blurred, filtered, and scan-converted. No geometry is generated. A large number of surface particles gives the appearance of a continuous surface. However, holes can appear if there is no adaptive control of the density of particles.

Figure 2.4: Streamsurface in the flow around a post.

Image courtesy of J.P.M. Hultquist (Reference [39]).

2.2 Local Icons

Local vector icons represent information about vector gradients. Existing local vector icons include point icons, such as critical-point glyphs, and line icons, such as streamribbons and streamtubes.

2.2.1 Critical Points and Their Glyphs

Phase-space techniques used in analyzing differential equations can be applied to visualize fluid flows. Among these techniques, important features of vector fields are critical points—i.e., points in the flow where the magnitude of the vector field vanishes and where the slope of streamlines is locally indeterminate. Streamlines never cross each other except at critical points (References [43, 44, 45]).

Critical points are rarely used by themselves for visualization purposes; they are generally embedded in a topological representation of vector fields—a global icon to be discussed in Section 2.3. However, as primary constituents of vector field topology, they are often displayed together with a glyph representing vector field gradients. In this respect, critical points are local icons and are therefore discussed in this section. We start with 2-D critical points, which are important for both 2-D vector fields (Sections 2.3.1 and 2.3.2) and 3-D vector fields (Sections 2.3.3). Then, we extend the discussion to 3-D critical points.

2-D Critical Points

Since a vector field vanishes at a critical point, the behavior of nearby streamlines is determined by the first order partial derivatives of the vector field. More precisely, the 2-D vector field $\vec{v} = (v_1, v_2)$ near a critical point is given, in most cases, by the first-order expansion

$$\begin{cases} v_1(dx_1, dx_2) \approx \frac{\partial v_1}{\partial x_1} dx_1 + \frac{\partial v_1}{\partial x_2} dx_2 \\ v_2(dx_1, dx_2) \approx \frac{\partial v_2}{\partial x_1} dx_1 + \frac{\partial v_2}{\partial x_2} dx_2 \end{cases}$$

where dx_1 and dx_2 are small distance increments from the critical point position. Thus, the nearby flow pattern is completely determined by the 2×2 Jacobian matrix

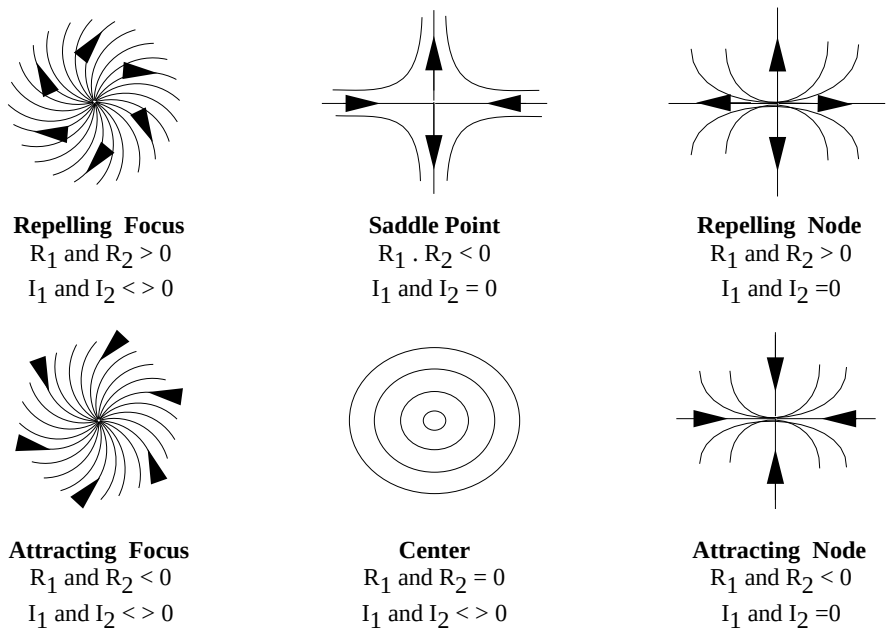

Figure 2.5: 2-D critical points. R1 and R2 denote the real parts of the eigenvalues of **J**, I1 and I2 the imaginary parts.

J, whose elements

$$J_{ij} = \frac{\partial v_i}{\partial x_j} \tag{2.2}$$

$(i, j = 1, 2)$, are evaluated at the critical point position.

Different patterns arise that are characterized by the invariants of the matrix **J**, or equivalently by its eigenvalues. Figure 2.5 shows how the eigenvalues of **J** classify a critical point as an attracting node, a repelling node, an attracting focus, a repelling focus, a center, or a saddle. Real eigenvectors of **J** are tangent to the streamlines ending at the critical point. A positive eigenvalue defines an outgoing direction and a negative eigenvalue corresponds to an incoming direction. When the eigenvalues are complex, the streamlines circulate about the critical point; the direction of the motion is inward if the real part of the eigenvalues is negative, and outward if it is positive.

Critical points sometimes occur so close together that it is difficult to distinguish among them. In fact, they act as elementary building blocks of the vector field, meaning that a combination of critical points looks like a single critical point in the far field. For example, the combination {node, saddle, node}, which occurs frequently, is similar to a pure node in the far field.

3-D Critical Points

The former classification of 2-D critical points can be extended to 3-D vector fields defined over 3-D domains, $\vec{v} = (v_1, v_2, v_3)$. The Jacobian $\mathbf{J}$ is now a 3×3 matrix whose elements are given by Equation 2.2, for $i, j = 1, 2, 3$. However, $\mathbf{J}$ has three eigenvalues and three eigenvectors. Again, real eigenvectors are tangent to streamlines ending at the critical point, and complex eigenvalues (which always occur in pairs) denote circulation. Thus, possible 3-D patterns include repelling nodes (eigenvalues are all real and positive), which behaves as 2-D repelling nodes in each of the three planes spanned by pairs of eigenvectors; attracting nodes (eigenvalues are all real and negative), which behaves as 2-D attracting nodes in each of the planes; saddle/saddle/nodes (eigenvalues are all real, but one has a different sign), which behaves as 2-D saddles in two planes and as a 2-D node in the third plane; and spiral nodes (one real and two complex conjugate eigenvalues), which have an attractive or repelling third direction. Figure 2.6, for example, shows a saddle/saddle/node. This type of critical points plays an important role in flow separation (Section 2.3.3). An algorithm for locating and extracting critical points is detailed in Reference [46].

3-D critical-point glyphs. We usually display critical points together with a glyph that characterizes local flow patterns (References [46, 40]). An example is given in Figure 2.7, which shows some of the 3-D critical points in the velocity field of Figure 2.1.

The arrows are oriented in the direction of the real eigenvectors of $\mathbf{J}$ and show incoming or outgoing directions that correspond to negative or positive eigenvalues, respectively. The disks are in planes spanned by pairs of complex eigenvectors, where circulation occurs. Dark blue or yellow disks represent positive or negative real parts.

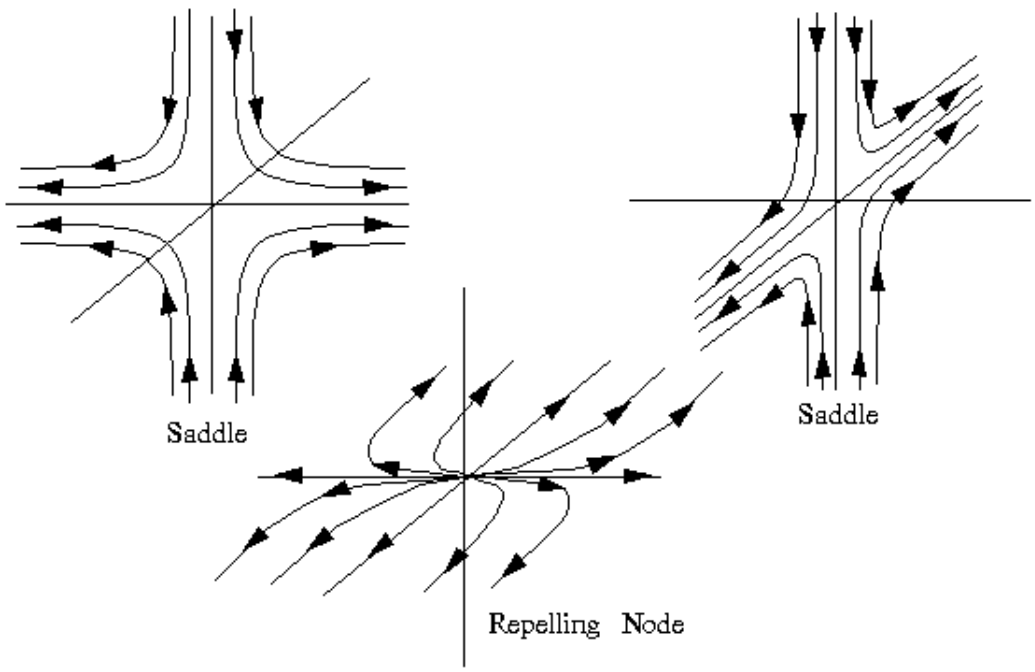

Figure 2.6: 3-D saddle/saddle/node.

Light blue or red disks represent imaginary parts.

The glyphs in Figure 2.7 are point local icons that visualize vector field gradients J_{ij} at critical points. In addition, we can use these glyphs to represent J_{ij} at other points in the flow, where $\vec{v}$ does not vanish. In this case, the glyphs represent local flow patterns seen by a massless observer moving with the flow. That is, they encode the behavior of neighboring streamlines relative to the observer's own trajectory.

Unsteady Flow Fields. Critical points in unsteady vector fields move and eventually merge or split. These phenomena are studied by tracking and representing their trajectories over time (Reference [47]), or by locating interactively critical points in nearby space-time regions (Reference [48]).

Figure 2.7: Local characterization of the velocity field in Figure 2.1.

Image courtesy of J. Helman (Reference [40]).

2.2.2 Streamribbons and Streamtubes

Fluid elements moving along streamlines of nonuniform vector fields undergo local deformations due to vector field gradients. These deformations are expressed mathematically by the components of the matrix **J** (Equation 2.2) along the trajectories. Two distinct additive deformation mechanisms arise: strain and rigid body rotation. Strain changes the shape and volume of fluid elements, and is expressed locally by the symmetric part of **J**—i.e., the rate-of-strain tensor ϵ_{ik} (Table 1.2). Rigid body rotation, on the other hand, is described by the antisymmetric component of **J**, which is equivalent to the vorticity vector, $\vec{\omega}$ (Table 1.1).

The critical-point glyphs of Section 2.2.1 represent **J** at isolated points. In the following, we discuss streamribbons (References [49, 50, 51, 52]) and streamtubes (References [51, 52]), both of which are local line icons representing, at least partially, deformations along streamlines. More complex tensor icons, such as those to be discussed in Section 3.5, must be used for a complete depiction of deformations.

Streamribbons

Streamribbons are narrow surfaces defined by two adjacent streamlines. An example is given in Figure 2.8, where streamribbons are used to visualize the flow near the surface of the cylinder in Figure 2.1. (The cylinder's surface is outlined by dots.)

Streamribbons are, in fact, streamsurfaces built from a front of only two particles.[1] They nevertheless are local icons, since their width reflects local flow divergence, and their twist rate encodes local streamwise vorticity. Indeed, the rotation of a ribbon sheet per unit length is given by

$$\frac{d\phi}{ds} = \frac{1}{2}\frac{\vec{\omega}\cdot\vec{v}}{|v|} \tag{2.3}$$

where s is the distance along the streamline. The right-hand side is half the streamwise vorticity. Adjacent streamlines in vortical regions wrap around each other, therefore

[1]Streamribbons are generated by using simplified versions of the streamsurface algorithm discussed in Section 2.1.3. Another technique, which is detailed in Reference [50], consists in interpolating the two constituent streamlines for additional intervening lines that are clustered together to give the appearance of a surface. This technique is useful for drawing streamribbons that are transparent, or with plotting devices capable of line plots only.

Figure 2.8: Streamribbons near the surface of the body in Figure 2.1. The twist of the ribbons encodes streamwise vorticity, and their width reflects cross-flow divergence.

creating streamribbons with high twist rate.

Streamribbons in divergent flows may become too wide; in this case they must be discarded since the twist rate no longer correctly reflects the streamwise vorticity along the trajectory. To remedy this, streamribbons in Figure 2.8 are built by adding to a single streamline, a narrow strip of polygons whose twist is obtained by integrating Equation 2.3 along the trajectory. This avoids problems related to flow divergence, and produces streamribbons that always have the correct twist (Reference [52]).

Streamtubes

Combined effects of streamwise vorticity and transverse strains can be visualized by linking N streamribbons and forming a streamtube, as in Figure 2.9 (top) where $N = 4$. The technique amounts to sweeping along a streamline a N-sided polygon[2] that is deformed locally by the matrix $\mathbf{J}$. In a streamtube, the rotation of the edges reflects both streamwise vorticity and transverse strains,[3] whereas the expansion of the cross-section encodes cross-flow divergence. Figure 2.9 (bottom) compares a streamline, a streamribbon, and a streamtube with $N = 6$, respectively. Alternate faces of the streamtube are colored with flow temperature and flow pressure.

Again, problems in diverging flows can be avoided by computing only one streamline, and surrounding it by a tubular surface whose cross-section varies as a function of the cross-flow divergence along the trajectory (References [51, 52]).

2.3 Global Icons

As shown in Figure 2.1, arrows must be coarsely distributed in space to avoid visual clutter. Comprehending the global structure of the vector field is then made difficult because of the need to interpolate the displayed information. In this respect, line icons such as streamlines are more appropriate. Understanding complex flows, however, requires many streamlines which clutter the display without guaranteeing the

[2] Hence the name "streampolygon" of this technique (Reference [51]).

[3] Discriminating between both effects is somewhat difficult. A palliative solution consists in adding to the surface a narrow colored stripe with techniques similar to those in Reference [51]. If the stripe is forced to rotate according to Equation 2.3, the effect of streamwise vorticity can be isolated.

Figure 2.9: Streamtube colored with air pressure, visualizing the flow in a room (top); comparison of a streamline, a streamribbon, and a streamtube (bottom).

Image courtesy of W.J. Schroeder (Reference [51]).

detection of all important features of the flow.

These problems typically arise from using elementary icons. With global icons, we render the structure of the complete data field by producing a simplified and more abstract representation. We prevent visual clutter by discarding unnecessary information, while keeping only those features that are structurally relevant. By using global icons and reducing the multivariate data field to a set of points, lines, or surfaces, we achieve significant data compression. Also, due to their simplicity and abstract nature, global icons are suitable input to automated data analysis systems (Reference [53]).

There is no universal method for designing global icons and each solution is problem-specific. In the following, we focus on flows past a body, which play a central role in aerodynamics, and we discuss their topological representation.

2.3.1 2-D Vector Field Topology

Vector field topology is conceptualized as a schematic depiction of the behavior of a large collection of streamlines. The basic constituents of vector field topology are

- the critical points (Section 2.2.1) and
- the set of their connecting streamlines.

Among critical points, saddle points are distinct in that there are only four tangent curves which actually hit the point itself (Figure 2.5). These tangent curves are called "separatrices" because streamlines that are arbitrarily close to each other on either side of a separatrix are diverted to very different regions in the flow. In 2-D flows, critical points near the surface of a body have a similar property. Indeed, near walls where the velocity is constrained to be zero[4] the flow is mainly tangential and streamlines propagate parallel to the surface. However, there are points where the tangential velocity field vanishes and a streamline, instead of being deflected parallel to the body, suddenly originates or terminates on the surface. These points are known as "detachment" and "attachment" points, respectively (Reference [54]). They play

[4]No-slip condition.

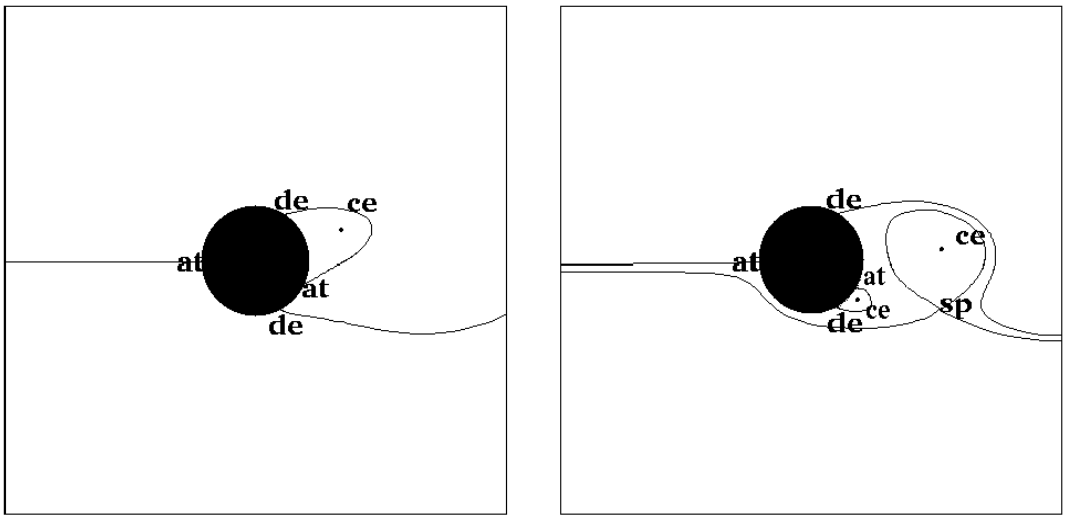

Figure 2.10: Topological representation of the 2-D flow past a circular cylinder at two different time steps. The flow is coming from the left; *at* = attachment point; *de* = detachment point; *sp* = saddle point; *ce* = center.

Image courtesy of J. Helman (Reference [40]).

the same role as saddle points in the sense that adjacent streamlines can be deflected in opposite directions.

Figure 2.10 shows topological skeletons of the 2-D flow past a cylinder at two different time steps. They are obtained by locating critical points, and by integrating streamlines from the saddle, attachment, and detachment points along the principal directions of their respective Jacobian matrices **J** given by Equation 2.2 (streamlines in the incoming directions are integrated backward).

The topological skeletons divide the field into regions topologically equivalent to uniform flow. The representation is highly effective, due to the ease of inferring from these simplified graphs the instantaneous behavior of every streamline in the flow. Also, comparing the flow at different time steps is greatly facilitated and can be automated using syntactic pattern recognition (Reference [53]). The flow in Figure 2.10, for example, underwent a topological transition between the two represented time steps—the attachment-detachment bubble on the left having developed into a paired

saddle and center on the right.

2.3.2 2-D Time-Dependent Vector Field Topology

Global icons of vector fields that depend on time, Reynolds number, or any other parameter, must represent not only the "instantaneous" structure of the flow but also topological transitions that may occur between consecutive steps. For 2-D vector fields, such icons can be obtained by stacking instantaneous topological skeletons (Reference [55]).

Figure 2.11 evinces the complete spatiotemporal evolution of the flow previously shown at two individual time steps in Figure 2.10. Adjacent skeletons are joined by linking their corresponding critical points and connecting streamlines, and the stacked topologies are displayed as a set of surfaces with the third dimension corresponding to time. Yellow and blue surfaces correspond to incoming and outgoing separatrices of the saddle points, respectively; surfaces from attachment points are colored orange and those from detachment points are colored purple. The periodic vortex shedding can be seen in the repeated development and movement downstream of saddle-center pairs. This clearly evinces the spatiotemporal structure of the flow.

2.3.3 3-D Separated Flows

3-D separated flows play a significant role in aerodynamics because of the close relationship between separation and vortices, which are important structures of the flow far from the body (Reference [54]).

As in the 2-D example of Figures 2.10 and 2.11, the fluid in 3-D separated flows moves parallel to the body and then suddenly detaches from the surface, creating vortices in the wake. The fluid can also reattach, causing recirculation regions similar to the bubble in Figure 2.10. However, detachment and attachment in 3-D flows do not arise at isolated points on the surface of the body, but are distributed along entire lines that extend into surfaces in the flow. Theoretical papers have been written on the subject (References [56, 57, 54]), but computer visualization techniques are necessary for accurately depicting both the surface of separation and the associated

Figure 2.11: Topological surfaces depicting the time evolution of the 2-D flow past a circular cylinder. Time increases from back to front.

Image courtesy of J. Helman (Reference [40]).

vortices. In this section, we discuss several complementary global icons. First, we display the skin-friction topology, that characterizes the flow near the surface of the body. Then, we represent topological extensions in the flow, namely the surface of separation and associated vortices.

Since there is no agreement on a universal definition of vortex and vortex core, resulting visualization techniques are varied and numerous. Batchelor, for example, defines a vortex core as "a region with a finite cross-sectional area of relatively concentrated vorticity (Reference [58])," while Chong et al. suggest that "a vortex core is a region of space where the vorticity [$\vec{\omega}$ (Table 1.1)] is sufficiently strong to cause the rate-of-strain tensor [ϵ_{ik} (Table 1.2)] to be dominated by the rotation tensor—i.e., the ...[velocity gradient] has complex eigenvalues (Reference [45])." As pointed out by Yates et al., "in ...[3-D] separated flows, ...there are no discontinuities that define the extent of the vortices and their cores (Reference [59])." The problem of detecting and representing vortices is therefore complex. We close the discussion on separation by two vortex detection techniques that are gaining wide acceptance: representation by means of helicity density (which involves object contraction), and line icons for vortex core tracing.

Skin-Friction Topology

The first step in visualizing 3-D separated flows consists in depicting the structure of the vector field near the body, for which an adequate description is inferred from the skin-friction field—i.e., the 2-D tangential velocity field one grid plane away from the surface of the body.[5]

Experimentally, the skin-friction field is studied by examining the streaks that form in an oil film on the surface of a body in a wind tunnel (Reference [27]). In computer visualization, similar information is derived by integrating 2-D streamlines of the skin-friction field or, preferably, by extracting its 2-D topological skeleton. The skin-friction topology of the flow in Figure 2.1 is represented in Figure 2.12 which shows outgoing separatrices, incoming separatrices, as well as 2-D nodes *(N)*, foci *(F)*, and saddles *(S)*. The main difference with former topological examples is that critical

[5]Velocity vanishes right on body.

Figure 2.12: Skin-friction topology on the upper hemisphere of the cylinder in Figure 2.1. *Sa, Ss* = saddles of attachment and separation; *Na, Ns* = nodes of attachment and separation; *Fa, Fs* = spiral nodes of attachement and separation.

points are now truly three-dimensional. Hence, they always have a principal direction that cuts the surface, and along which the flow is either outgoing (attachment points), or incoming (detachment or separation points).

Surface of Separation

The surface of separation and the associated vortices are extensions in the flow of the skin-friction topology. Among skin-friction critical points, saddles of separation *(Ss)* play indeed a particular role. As shown in Figure 2.6, their 3-D structure is really saddle/saddle/repelling node. Hence, there is always an entire plane of outgoing trajectories that emanate from them and that leave the surface of the body.[6] In fact, the surface of separation intersects the body along the outgoing separatrices of the saddles of separation, which are therefore called "lines of separation." Note that these lines always connect saddle points to nodes or foci, but not to other saddles because such connections are structurally unstable.

The surface of separation is the streamsurface computed by advecting (as in Section 2.1.3) a front of particles initially positioned along the lines of separation. For example, Figure 2.13 shows parts of the surface of separation whose rolled up form delineates vortices. (Compare Figure 2.13 to Figure 2.3.)

Object contraction and helicity density. Drawing the surface of separation is appropriate for detecting vortices. Yet it is complex and requires critical points and lines of separation to exist in the skin-friction field—in which case the separation is termed "global" (Reference [56]). As opposed to this, the skin-friction field in "local"[7] separations does not possess such features. The flow exhibits all the characteristics of separation downstream from the surface of the body, but not right on it. It is therefore not possible to compute surfaces of local separations with the aforementioned technique.

Object contraction offers a simple and reliable alternative. Instead of representing

[6]The same situation arises for 3-D nodes and spiral nodes that are repelling in every direction; however, these nodes do not appear in incompressible or steady compressible flows because they are not compatible with the continuity equation.

[7]Also called "cross-flow" (Reference [57]).

Figure 2.13: Streamsurfaces depicting separation topology.

Image courtesy of J. Helman (Reference [40]).

vector fields such as velocity $\vec{v}$ or vorticity $\vec{\omega}$, one can display a scalar function, the helicity density defined by Moffat (Reference [60]) as

$$H_d = \vec{v} \cdot \vec{\omega} = |\vec{v}||\vec{\omega}| \cos \varphi$$

where φ is the angle between $\vec{v}$ and $\vec{\omega}$. Contour lines of H_d are shown in Figure 2.14.[8] The advantage of displaying H_d rather than other scalar functions, such as vorticity magnitude ($|\vec{\omega}|$) or enstrophy density ($\frac{1}{2}|\vec{\omega}|^2$), is that both its magnitude and sign are relevant. Indeed, large positive values of H_d reflect large velocity and vorticity magnitudes together with small values of φ—a configuration that denotes right-handed vortices. Conversely, large negative values of H_d indicate left-handed vortices. The contour lines in Figure 2.14 allow us to discriminate between primary and smaller secondary vortices—they have opposite swirl (color)—and reveal structures hidden in all of Figures 2.1, 2.2, and 2.3. Figure 2.14 also illustrates the correlation between changes in swirl direction and skin-friction lines, a fact noted in Reference [61].

Line icons for vortex core detection. Instead of drawing the entire surface of separation, one can further simplify the display and draw only vortex cores—i.e., vortex center lines. In global separations, vortex cores are streamlines lying at the edges of the separation sheet. They are often associated with spiral nodes (Section 2.2.1) either in the flow above the body[9] or on its surface.[10] In both cases, vortex cores are found by integrating from spiral nodes streamlines in the direction of the real eigenvector. Vortex cores obtained by this technique are shown in magenta in Figure 2.14; they are in good agreement with the contour lines of H_d. However, no vortex core is found for the secondary separation, which is local and therefore not associated with any critical point. In this case, other core detection techniques are applicable. For example, streamlines can be integrated from points in the flow where scalar functions, such as velocity magnitude, normalized helicity,[11] or streamline curvature, are extremum. Each method generally yields slightly different results (Reference [59]),

[8] Using H_d is obviously not restricted to local separations and applies equally well to global separations, such as the primary separation in Figure 2.14.

[9] Type I separation (Reference [57]).

[10] Type II separation (Reference [57]).

[11] The normalized helicity $H_n = \frac{H_d}{|\vec{v}||\vec{\omega}|}$ is discussed in Reference [61].

Figure 2.14: Contour lines of helicity density H_d (red/white = right-handed vortices; blue/black = left-handed vortices), together with skin-friction topology (blue and yellow lines) and vortex cores (magenta lines).

suggesting that a precise and universal definition, as well as a method for detecting vortex cores, is still open to question.

2.4 Chapter Summary

In this chapter, we review state-of-the-art visualization techniques for vector fields, with a special emphasis towards fluid flow data. We use the framework laid out in Chapter 1 as a guide to the exposé. (In subsequent chapters, we use the same methodology to develop tensor-field visualization mappings.)

First, we discuss elementary vector icons, which represent vector data strictly across the extent of their spatial domain. Using point icons (arrows) often results in visually cluttered displays, but using continuous icons can produce better representations. These include line icons—such as particle traces, streaklines, and streamlines—and surface icons—such as streamsurfaces. The underlying continuity of vector fields is clearly better conveyed this way, although important flow features, such as small vortices, can still be missed. We also demonstrate the benefits of using tubes with finite cross-section rather than thin lines to comprehend the (possibly complex) spatial arrangement of a large number of streamlines displayed simultaneously. This review of elementary vector icons lays out a basis for designing elementary tensor icons in Chapter 3.

Then, we discuss local vector icons, which display vector gradients in addition to elementary information. We provide a classification of critical points—i.e., points in the flow where velocity vanishes. Critical points are typically drawn with a glyph that represents local streamline patterns (velocity gradients). When moving along their trajectories, fluid elements undergo deformations caused by velocity gradients. We can represent these deformations, at least partially, by drawing local line icons—i.e., surfaces built around streamlines and representing aspects of both the rate-of-strain tensor and the vorticity vector. We do not discuss local surface icons, which are yet to be designed. The analysis and classification of critical points is a useful introduction to the study of local tensor patterns around degenerate points—a topic to be developed in detail in Chapter 4.

Finally, we discuss global representations of vector fields, restricting the scope to the case of flow fields past bodies. After reviewing 2-D vector field topology, which is based on critical points and the set of their connecting separatrices, we derive a topological representation of 2-D time-dependent vector fields by stacking instantaneous topological skeletons. Then, we deal with the topology of 3-D separated flows—in which case basic topological constituents are skin-friction topology and 3-D topological extensions. The skin-friction topology is the topology of the 2-D vector field tangent to the body's surface, and 3-D topological extensions are the separation surface and vortices. We discuss vortex-detection techniques, including helicity density and line icons. Many parallels will emerge in Chapter 4, where we define and analyze global icons of tensor fields.

Chapter 3

Elementary Tensor Icons

In this chapter, we develop elementary icons of continuous tensor fields. Instead of visualizing the data at discrete, coarsely spaced points, we represent tensor fields along lines, so as to render the underlying continuity of the data while reducing visual clutter. We restrict the discussion to line icons, as surface icons are yet to be designed. Conceptualizing tensor fields as a network of line icons enables us to analyze their geometric properties; the material discussed here lays the foundation for the topological analysis of tensor fields to be developed in Chapter 4.

We refer the reader to Section 1.2 for equations that show explicitly the data to be visualized. In Section 3.1, we prove that symmetric tensor fields with continuous components have eigenvectors that are continuous "almost everywhere"—an important fact for the design of continuous icons. In these regions, we can conceptualize continuous, symmetric tensor fields as several orthogonal families of continuous, smooth, and non-intersecting curves. In Section 3.2, we discuss textures to render these curves in the case of 2-D symmetric tensor fields (Equation 1.4) which are fully equivalent to the two orthogonal eigenvector fields

$$\vec{v}_i = \lambda_i \vec{e}_i$$

where $i = 1, 2$. In Section 3.3, we develop line icons of 3-D symmetric tensor fields (Equation 1.6) to which correspond three orthogonal eigenvector fields

$$\vec{v}_i = \lambda_i \vec{e}_i$$

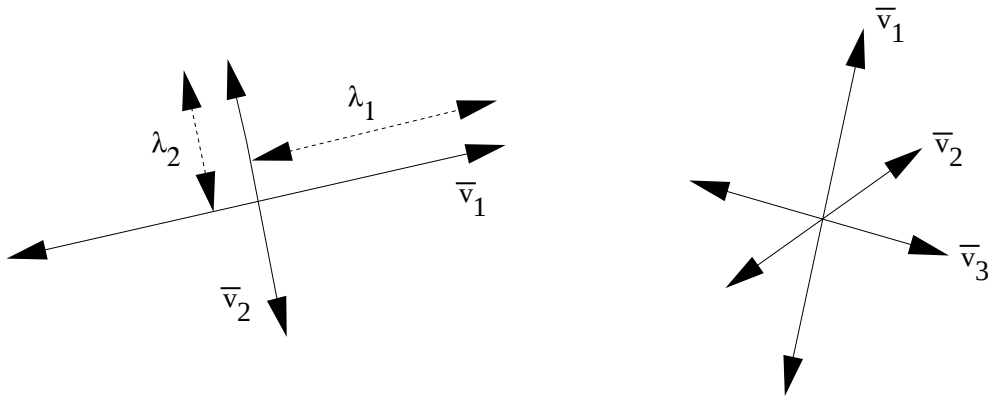

Figure 3.1: Point icons of 2-D and 3-D symmetric tensor fields.

where $i = 1, 2, 3$. In Section 3.5, we briefly discuss line icons of 3-D asymmetric tensor data (Equation 1.8), a case which is complicated by the possible occurrence of complex eigenvalues and complex, non-orthogonal eigenvectors. Finally, we summarize the results in Section 3.6.

3.1 Continuous Icons versus Point Icons

Consider a n-dimensional symmetric tensor field, $\mathbf{T}$. Its simplest and most natural representation is a set of n orthogonal eigenvectors, $\vec{v}_i$ (Equation 1.5 or 1.7). Figure 3.1 shows elementary point icons that represent $\mathbf{T}$ for $n = 2$ and $n = 3$, respectively. Eigenvectors are drawn as bidirectional arrows due to their sign indeterminacy. There are other point icons equivalent to those in Figure 3.1. In Figure 1.5 for example, ellipses with principal axes lying along the eigenvectors $\vec{v}_i$ were used to visualize $\mathbf{T}$ at coarsely spaced points. Likewise in three dimensions, we can visualize three eigenvector fields either with ellipsoids or with Haber's tensor glyphs, which are slightly more sophisticated point icons designed to improve the perception of the eigenvectors (References [12, 13]).

However, using point icons to represent tensor fields inevitably produces severe visual clutter. (When compared to vector arrows, visual clutter is enhanced; imagine Figure 2.1 with ellipsoids instead of arrows!) To avoid cluttered images, the density of displayed icons must be kept so low that it becomes impossible to comprehend the structure of the tensor data by mentally interpolating adjacent icons.

Fortunately, most tensor fields encountered in practice are spatially continuous and we can obtain better representations by using icons that embed the underlying continuity in their very design.

Definition 2 (Continuity of Tensor Fields) *Let E be an open subset of $\mathbf{R}^n$, and let $\mathbf{T} : E \to \mathcal{L}(\mathbf{R}^n, \mathbf{R}^n)$ be a tensor field defined across E. We define*

$$\mathbf{T} \in C^k(E) \quad (k \geq 0)$$

iff the n^2 partial derivatives

$$\frac{\partial^k T_{ij}}{\partial x_{j_1} \cdots \partial x_{j_k}} \quad (i, j = 1, \ldots, n)$$

exist and are continuous across E. (Each of the indices $j_1, \ldots, j_k$ belongs to the set $\{1, \ldots, n\}$.)

For example, tensor data defined on a regular grid and linearly interpolated in between vertices belong to at least $C^1(E)$.

Because tensor icons represent the eigenvector fields, we discuss in the following the relation between continuity and differentiability of the tensor components (T_{ij}), and continuity and smoothness of the eigenvectors ($\vec{v}_i$). (The sign of $\vec{v}_i$ being indeterminate, by "continuity and smoothness of $\vec{v}_i$" we really mean continuity and differentiability of $\vec{v}_i$'s magnitude—λ_i—and $\vec{v}_i$'s direction—any angles that unambiguously characterize the orientation of an undirected line segment lying along $\vec{v}_i$.)

Let β_{ij} be the coefficients of an orthonormal transformation that diagonalizes a symmetric tensor field $\mathbf{T} = \{T_{ij}\}$, $i, j = 1, \ldots, n$. From Equation 1.3 and from the orthonormality of the coefficients β_{ij},

$$T_{ij} = \sum_{p=1}^{n} \beta_{pi} \beta_{pj} \lambda_p \quad (i, j = 1, \ldots, n) \tag{3.1}$$

where λ_p, $p = 1, \ldots, n$, are the eigenvalues of $\mathbf{T}$. Equations 3.1 provide relations between tensor components, eigenvalues, and orientation of the eigenvectors (β_{ij} is the jth-component of the unit eigenvector $\vec{e}_i$). $\mathbf{T}$ is symmetric ($T_{ij} = T_{ji}$), so there are only $\frac{1}{2}n(n+1)$ independent tensor components which we denote by $X_1, \ldots, X_{\frac{n(n+1)}{2}}$. There are n eigenvalues, λ_i, and $\frac{1}{2}n(n-1)$ independent angles, α_i, that define the orientation of the eigenvectors (or equivalently, the coefficients β_{ij}). Thus, Equations 3.1 can be written as a system of $\frac{1}{2}n(n+1)$ equations

$$F_k(X_1, \ldots, X_{\frac{n(n+1)}{2}} | \lambda_1, \ldots, \lambda_n; \alpha_1, \ldots, \alpha_{\frac{n(n-1)}{2}}) = 0 \quad (k = 1, \ldots, \frac{1}{2}n(n+1)) \tag{3.2}$$

Equations 3.2 implicitly define the n eigenvalues λ_i and the $\frac{1}{2}n(n-1)$ angles α_i in terms of the $\frac{1}{2}n(n+1)$ tensor components X_i.

Assume that $\mathbf{T} \in C^1(E)$—i.e., that all the partial derivatives

$$\frac{\partial X_i}{\partial x_p} \quad (i = 1, \ldots, \frac{1}{2}n(n+1))$$

exist and are continuous across the domain E. (x_p, $p = 1, \ldots, n$, are position coordinates.) Then, according to the Implicit Function Theorem (Reference [62]), the set of implicitly defined functions

$$\lambda_i(X_1, \ldots, X_{\frac{n(n+1)}{2}}) \quad (i = 1, \ldots, n)$$

and

$$\alpha_i(X_1, \ldots, X_{\frac{n(n+1)}{2}}) \quad (i = 1, \ldots, \frac{1}{2}n(n-1))$$

are unique, continuous, and differentiable with respect to position coordinates at every point $\vec{x}$ of E where the $\frac{1}{2}n(n+1) \times \frac{1}{2}n(n+1)$ Jacobian determinant

$$\begin{vmatrix} \frac{\partial F_1}{\partial \lambda_1} & \cdots & \frac{\partial F_1}{\partial \lambda_n} & \frac{\partial F_1}{\partial \alpha_1} & \cdots & \frac{\partial F_1}{\partial \alpha_{\frac{n(n-1)}{2}}} \\ \vdots & \vdots & \vdots & \vdots & \vdots & \vdots \\ \frac{\partial F_{\frac{n(n+1)}{2}}}{\partial \lambda_1} & \cdots & \frac{\partial F_{\frac{n(n+1)}{2}}}{\partial \lambda_n} & \frac{\partial F_{\frac{n(n+1)}{2}}}{\partial \alpha_1} & \cdots & \frac{\partial F_{\frac{n(n+1)}{2}}}{\partial \alpha_{\frac{n(n-1)}{2}}} \end{vmatrix} \neq 0 \tag{3.3}$$

We can show that this determinant vanishes only at points where

$$\lambda_1 - \lambda_2 = 0$$

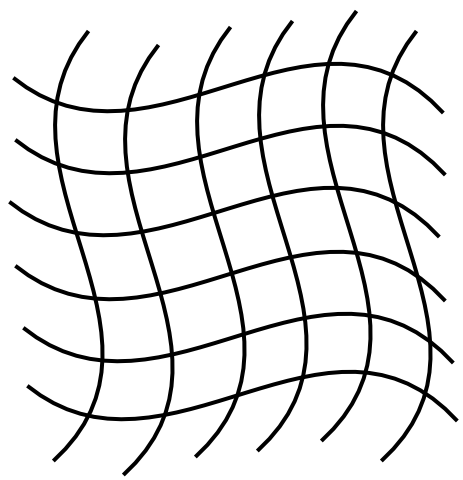

Figure 3.2: Representation of a continuous and symmetric tensor field as orthogonal families of smooth, non-intersecting curves for the case $n = 2$. This analogy holds in regions that do not comprise degenerate points.

for $n = 2$, and

$$(\lambda_1 - \lambda_2)(\lambda_2 - \lambda_3)(\lambda_3 - \lambda_1) = 0$$

for $n = 3$.[1] Thus, the unsigned eigenvectors $\vec{v}_i$ are uniquely defined, continuous, and smoothly varying in space, at every point $\vec{x}$ of E where eigenvalues are distinct from each other.

We call "degenerate points" the points where two or more eigenvalues are equal. In Chapter 4, we develop a theory of tensor field topology based on degenerate points but for the remaining of this chapter, we restrict our analysis to areas that do not

[1]The proof goes as follows. For $n = 2$, Equations 3.2 consist of three relations linking three independent tensor components ($X_1 = T_{11}$, $X_2 = T_{12}$, and $X_3 = T_{22}$), two eigenvalues (λ_1 and λ_2), and one angle α_1 ($0 \leq \alpha_1 < \pi$) that determines the orientation of the eigenvectors. Accordingly, $\beta_{11} = \cos\alpha_1$, $\beta_{12} = \sin\alpha_1$, $\beta_{21} = -\sin\alpha_1$, and $\beta_{22} = \cos\alpha_1$. After expliciting the β_{ij}'s in Equations 3.1, the 3×3 determinant in Equation 3.3 can be shown to be equal to $\lambda_1 - \lambda_2$. The $n = 3$ case is similar in essence but involves more complex mathematics; the determinant in Equation 3.3 is now 6×6. Equations 3.2 consist of six implicit relations, with $X_1 = T_{11}$, $X_2 = T_{12}$, $X_3 = T_{13}$, $X_4 = T_{22}$, $X_5 = T_{23}$, and $X_6 = T_{33}$. There are three eigenvalues, λ_1, λ_2, and λ_3. Three angles, α_1, α_2, and α_3, are necessary to determine the orientation of the eigenvectors. By expanding the coefficients β_{ij} in terms of Euler's angles—precession, nutation, and gyration—we can compute the 6×6 determinant in Equation 3.3.

comprise degenerate points. Within these regions, the tensor field can be thought of as a set of n orthogonal families of curves that are continuous, smooth, and that do not intersect each other (Figure 3.2). Each family of curves is tangent to an eigenvector field. The very purpose of line icons is to render and cross-correlate the n eigenvalues with these n families of curves.

3.2 2-D Symmetric Tensor Fields

In this section, we discuss line icons of 2-D symmetric tensor fields. The data are equivalent to two orthogonal eigenvector fields $\vec{v}_i$, $i = 1, 2$ (Equation 1.5). Instead of drawing point icons at coarsely spaced points, we render two orthogonal families of curves (Figure 3.2) together with the corresponding eigenvalues.

We select one eigenvector field—which we refer to as the longitudinal eigenvector, $\vec{v}_l$—and we render its tangent curves. We call these curves "hyperstreamline trajectories" for consistency with the 3-D icons to be discussed in Section 3.3. By using color to encode the longitudinal eigenvalue, we represent $\vec{v}_l$ completely. We can similarly process the other eigenvector field to obtain a complementary set of orthogonal trajectories.

Hyperstreamline trajectories integrate a continuous distribution of point icons, such as the cross in Figure 3.1 (left); they show, for example, how forces are transmitted in a stress-tensor field and how momentum is transferred in a momentum-flux-density tensor field.

3.2.1 Texture Generation

To draw hyperstreamline trajectories, we can use numerical techniques to integrate the longitudinal eigenvector, get a list of points that define the trajectories, and scan-convert the resulting line segments. In the following, we discuss yet another technique which consists of generating anisotropic textures to render a continuous distribution of hyperstreamline trajectories. Compared to numerical integration, the resolution of the display is not improved. Textures, however, have considerable advantages.

- Textures are space filling. Numerical integration of the longitudinal eigenvector field yields only a few trajectories that are essentially determined by the location of the starting points; integrating trajectories merely samples the tensor field, bearing the risk of missing important data features. Conversely, we generate textures by sequentially processing each pixel, yielding a complete picture of the data (at texture resolution).

- Textures do not require an integration of the eigenvector fields, a process significantly complicated by the eigenvectors' sign indeterminacy and by degenerate eigenvalues (see 3-D hyperstreamlines in Section 3.3).

- Textures create visually appealing images, which are among other uses suitable for presentations outside of the scientific community.

A drawback of textures, however, is that they are viewpoint dependent. This makes otherwise straightforward geometric operations costly—such as translating, rotating, and zooming.

To create a texture, we assign to each pixel (x, y) a color $\vec{\mathcal{C}}(x, y)$ and an opacity $\mathcal{O}(x, y)$. We then blend the color on a black background to yield a pixel value $\vec{\mathcal{P}}(x, y) = \mathcal{O}(x, y)\vec{\mathcal{C}}(x, y)$. The color $\vec{\mathcal{C}}(x, y)$ is determined by the longitudinal eigenvalue (or by any other user-defined function of the tensor field). The opacity $\mathcal{O}(x, y)$ is computed by convolving a 2-D band-limited noise with a spatial filter kernel.

The band-limited noise is a 2-D version of Perlin's *noise* function (Reference [63])—i.e., a sum of pseudorandom spline knots, one for each vertex of an integer lattice of $\mathbf{R}^2$. Let Δ_x and Δ_y be the lattice interspacing in x and y directions, respectively. The knot Ω_{ij} at lattice point $(i\Delta_x, j\Delta_y)$ is a pseudorandom linear gradient $\vec{\mathcal{G}}_{ij} = (\mathcal{G}^1_{ij}, \mathcal{G}^2_{ij})$ weighted in each dimension by a smooth drop-off function $\omega(t)$. That is,

$$\Omega_{ij}(u, v) = \omega(u)\omega(v)(\mathcal{G}^1_{ij}u + \mathcal{G}^2_{ij}v)$$

where

$$u = \frac{x - i\Delta_x}{\Delta_x}$$

and

$$v = \frac{y - j\Delta_y}{\Delta_y}$$

$\omega(t)$ is the cubic function

$$\omega(t) = \begin{cases} 2|t|^3 - 3|t|^2 + 1 & |t| < 1 \\ 0 & |t| \geq 1 \end{cases}$$

which is a spline of support 2. Thus, the *noise* function at (x, y) is given by

$$noise(x, y) = \sum_{i=\lfloor \frac{x}{\Delta_x} \rfloor}^{\lfloor \frac{x}{\Delta_x} \rfloor + 1} \sum_{j=\lfloor \frac{y}{\Delta_y} \rfloor}^{\lfloor \frac{y}{\Delta_y} \rfloor + 1} \Omega_{ij}\left(\frac{x - i\Delta_x}{\Delta_x}, \frac{y - j\Delta_y}{\Delta_y}\right)$$

where "$\lfloor \cdots \rfloor$" denotes the floor function. For spatially varying tensor data, the filter kernel to be convolved with the *noise* function is space-variant; its orientation changes across the image. We use for filter kernel a pyramid function of support $2L$

$$\wedge_L(u) = 1 - \frac{\min(|u|, L)}{L}$$

that extends spatially in the direction of the longitudinal eigenvector (L is a user-controlled parameter). Thus, the opacity $\mathcal{O}(x, y)$ at pixel (x, y) is given by

$$\mathcal{O}(x, y) = \int_{-\infty}^{\infty} \wedge_L(u) noise(x - u \cos \alpha(x, y), y - u \sin \alpha(x, y)) du$$

where $\alpha(x, y)$ is the angle between the x-axis and the longitudinal eigenvector at (x, y).

We can use filter kernels with different supports—such as elongated ellipses, rectangles, or curved hyperstreamline segments. The latter adapts to tensor fields Cabral's "Line Integral Convolution" algorithm for vector fields (Reference [23]). This algorithm, however, requires a local integration of the longitudinal eigenvector.

As an example, we consider the Reynolds-stress tensor in a 2-D flow past a circular cylinder. Reynolds stresses are induced by turbulent motion; they represent the net statistical effect of small-scale velocity fluctuations on particles moving with the mean flow. (Modeling turbulence usually involves modeling the Reynolds stresses; most turbulent flow solvers seek solutions to Navier-Stokes equations for the mean flow, with a modified stress-tensor field to account for the Reynolds stresses.)

The textures in Figure 3.3 represent the major ($\vec{v}_1$) and minor ($\vec{v}_2$) eigenvector fields, respectively. Color encodes the longitudinal eigenvalue according to color scale

Figure 3.3: Reynolds-stress tensor in a 2-D flow past a circular cylinder; major (top) and minor (bottom) eigenvector fields. Color scale 2 of Figure A.3 (Appendix A) is used to encode the longitudinal eigenvalue.

2 of Figure A.3 (Appendix A). Both eigenvalues are positive, so $\vec{v}_1$ and $\vec{v}_2$ lie in directions of maximum and minimum tension, respectively. Textures in Figure 3.3 exhibit interesting geometric features which would not appear by simply displaying contour plots of tensor components. Chapter 4 provides the tools necessary for a detailed analysis of these structures.

3.2.2 Trivariate Data Visualization

Equation 1.4 shows that 2-D symmetric tensor data are trivariate. When generating textures of individual eigenvector fields, we visualize this information in two separate images. If the goal is to correlate full tensor information in a single image, one must visualize simultaneously two eigenvalues and the orientation of the eigenvectors.

The "Natural Scene Paradigm" is useful to choose an adequate representation. This paradigm stipulates that bivariate data are best represented by using two information channels which we perceive as being mutually orthogonal—such as the height of terrain and its color (Reference [22]).

Here we apply the same paradigm to trivariate data, using texture as a third perceptual dimension. The tensor field in Figure 3.3 is shown again in Figure 3.4, where texture, color, and elevation of a surface are used as independent information channels that encode eigenvector direction, longitudinal eigenvalue, and transverse eigenvalue, respectively.[2] The display allows us to decouple information relevant to each eigenvalue and to each eigenvector direction, and provides a simple and integrated view of tensor data at the same time. It is interesting to note that much of the geometric structure (i.e., the singularities in the direction of the eigenvectors) correlates with high values of the minor eigenvalue (color), while it does not seem to depend much on the major eigenvalue (height).

[2]The vertical stretching creates an unwanted distortion of the texture which can be compensated for by techniques such as those described in Reference [64].

Figure 3.4: Trivariate data visualization to fully represent the Reynolds-stress tensor field corresponding to Figure 3.3.

3.3 3-D Symmetric Tensor Fields

In this section, we discuss line icons of 3-D symmetric tensor fields (Equation 1.6) to which correspond three orthogonal eigenvector fields $\vec{v}_i$, $i = 1, 2, 3$ (Equation 1.7). Away from degenerate points, the data consist of three eigenvalues and three orthogonal families of continuous, smooth, and non-intersecting curves. We seek visualization mappings that embed this multivariate information along trajectories in 3-D space.

3.3.1 3-D Hyperstreamlines

As for 2-D data, we select a longitudinal eigenvector field, $\vec{v}_l$, and we integrate its tangent curves. We surround the trajectories by tubular surfaces, which we call "hyperstreamlines," so as to encode the two transverse eigenvectors, $\vec{v}_{t_1}$ and $\vec{v}_{t_2}$. We build hyperstreamlines as follows:

Definition 3 (Hyperstreamline) *A geometric primitive of finite size sweeps along the longitudinal eigenvector field, $\vec{v}_l$, while stretching in the transverse plane under the combined action of the two transverse eigenvectors, $\vec{v}_{t_1}$ and $\vec{v}_{t_2}$. Hyperstreamlines are surfaces that envelop the stretched primitives along the trajectories. We color hyperstreamlines by means of a user-defined function of the three eigenvalues, usually the amplitude of the longitudinal eigenvalue.*

Color and trajectory of hyperstreamlines represent the longitudinal eigenvector field and cross-sections encode the transverse eigenvectors. Thus, hyperstreamlines fully represent tensor data along continuous trajectories. We refer to hyperstreamlines as "major," "medium," or "minor," depending on the corresponding longitudinal eigenvector field that defines their trajectories.

Hyperstreamline Trajectories

Figure 3.5 shows hyperstreamline trajectories in the elastic stress tensor induced by two compressive forces on the top surface of a cube. (Calculations are carried assuming a semi-infinite cube.) The trajectories show the transmission of forces inside the material. The curves directed upward are along the most compressive direction,

Figure 3.5: Stress tensor induced by two compressive forces; hyperstreamline trajectories. Color scale 1 of Figure A.3 is used.

the minor eigenvector $\vec{v}_3$, and converge towards regions of high stresses where forces are applied. Their color encodes the magnitude of the most compressive eigenvalue, λ_3, according to color scale 1 of Figure A.3 (Appendix A). Note the sudden divergence of close trajectories on each side of the plane of symmetry. Similarly, trajectories along the two other eigenvector fields delineate a surface shown near the bottom face of the cube. This surface is everywhere perpendicular to the most compressive direction.

The tensor field in Figure 3.6 is an example of "solenoidal" tensor field; its hyperstreamline trajectories obey specific geometric rules to be discussed in Section 3.4.

Hyperstreamline Cross-Sections

A hyperstreamline is further characterized by its cross-section, the geometric primitive that sweeps along the trajectory to encode transverse eigenvectors. We consider two types of primitives:

- a circle that stretches into an ellipse while sweeping along the longitudinal eigenvector field, and that generates a hyperstreamline called a "tube"; and
- a cross that generates a hyperstreamline called a "helix."

For example, Figure 3.6 shows two minor tubes that propagate upward and four medium and major helices of the stress-tensor field corresponding to Figure 3.5. In a tube, the principal axes of each elliptical cross-section lie along the transverse eigenvectors, $\vec{v}_{t_1}$ and $\vec{v}_{t_2}$; their length is proportional to the magnitude of the transverse eigenvalues, λ_{t_1} and λ_{t_2}. The same property holds for a helix, whose arms are proportional to the transverse eigenvectors. (Helices owe their name to the spiraling pattern of their arms that can be observed in some cases.) In this manner, both directional and amplitude information are encoded along the trajectory. The local sign of the transverse eigenvalues can be comprehended by examining the singularities of the cross-sections; wherever a transverse eigenvalue changes sign, the cross-section is reduced to a single line or to a point.

Tubes and helices encode the same information about the tensor field, but some aspects of the data are better perceived with one hyperstreamline type than with the other. Tubes, for instance, are superior at indicating locations where the tensor is

Figure 3.6: Stress tensor induced by two compressive forces; minor tubes, medium and major helices. Color scale 1 of Figure A.3 is used.

degenerate in the transverse plane, since recognizing that an ellipse is circular is easier than comparing the length of two perpendicular line segments. Further, if the tensor field is transversely degenerate in a whole region of space, helices are not adequate since the direction of transverse eigenvectors is not determined. Helices, however, provide better precision for perceiving the direction of the transverse eigenvectors.

To illustrate the type of information that is embedded in a hyperstreamline cross-section, Figure 3.7 displays four different stages of a minor tube in a stress-tensor field. The data are similar to the tensor represented in Figures 3.5 and 3.6, but we added an extra tension force to the surface of the cube. In the top-left, the cross-section is circular, showing that the transverse stresses have uniform magnitude. The top-right shows an increasing anisotropy of the transverse stresses, together with a decrease of the longitudinal eigenvalue (color). In the bottom-left, the cross-section is reduced to a straight line; one transverse eigenvalue vanishes and stresses are locally two-dimensional. In the bottom-right, stresses are three-dimensional once again; the eigenvectors undergo a rapid rotation and a substantial stretching revealing important gradients of shear and pressure in the region.

Integrating Hyperstreamlines

To compute hyperstreamline trajectories, we integrate the longitudinal eigenvector field using an adaptive Runge-Kutta algorithm (Reference [65]). A series of factors must be taken into account in order to perform this integration correctly:

- Trilinear interpolation of tensor data. For tensor data defined across a regular grid, the integration algorithm often requests the longitudinal eigenvector at locations in between vertices. However, we cannot simply interpolate eigenvectors because of their sign indeterminacy. So, we first perform a trilinear interpolation of tensor components, and then we diagonalize the interpolated data to yield the requested eigenvector.

Figure 3.7: Four different stages of a minor tube in an elastic stress-tensor field. Color scale 1 of Figure A.3 (Appendix A) is used.

- Degenerate eigenvalues. Degenerate eigenvalues can occur along a computed trajectory, at and in between sampling points requested by the integration algorithm. The longitudinal eigenvector is not defined at points where the longitudinal eigenvalue equals one of the transverse eigenvalues. Dealing with such points is a complex issue. The best approach consists of using the techniques to be discussed in Chapter 4, namely detecting beforehand points where the longitudinal eigenvalue is degenerate, classifying eigenvector patterns around these points, and deciding whether to terminate hyperstreamline trajectories at these points or not. (See Section 4.4 for details.)

- Sign indeterminacy of eigenvectors. The integration algorithm avoids jagged trajectories by selecting the sign of the longitudinal eigenvector that minimizes the angle between eigenvectors at consecutive points in the trajectory.

- Singularities of the cross-section. We also detect points where the transverse eigenvalues vanish so we do not miss singular hyperstreamline cross-sections (line segments or points).

3.3.2 Correlating Vector and Scalar data

An example of fluid flow visualization illustrates how hyperstreamlines may be used to correlate several different physical quantities. For the reversible part of the momentum-flux-density tensor, Π^r (Table 1.2), one may correlate pressure p, velocity direction, and kinetic energy density $\frac{1}{2}\rho v^2$ (ρ is the mass density and v is the velocity magnitude). Indeed, the tensor field Π^r can be diagonalized as

$$\Pi^r = \begin{pmatrix} p + \rho v^2 & 0 & 0 \\ 0 & p & 0 \\ 0 & 0 & p \end{pmatrix}$$

The major eigenvalue of Π^r is $\lambda_1 = p + \rho v^2$ and the associated unit eigenvector is the velocity direction. The other eigenvalues are degenerate and equal to pressure ($\lambda_2 = \lambda_3 = p$) in the whole space. It follows that only major tubes can be used. Their trajectories are everywhere tangent to the velocity field and correspond to

streamlines of the velocity field. The tubes' cross-sections are circular with a diameter proportional to the pressure p. In addition, we determine the tubes' color by the function

$$\text{color} \sim \frac{\lambda_1 - 0.5(\lambda_2 + \lambda_3)}{2} = \frac{1}{2}\rho v^2 \tag{3.4}$$

which is the kinetic energy density. Thus, trajectory, diameter, and color of major tubes encode velocity direction, pressure, and kinetic energy density, respectively.

Figure 3.8 shows Π^r in the flow past a hemisphere cylinder. The direction of the incoming flow is 5° to the left of the hemisphere axis. The detachment at the end of the cylinder is clearly visible. The pattern of hyperstreamlines indicates that momentum is transferred from the tip of the body to the end fairly uniformly with a globally decreasing kinetic energy, as shown by color variations. However, there is a sudden change of kinetic energy (color) and pressure (diameter) associated with a significant variation of the direction of the first five tubes.

3.3.3 Color Coding Schemes

Usually we encode the longitudinal eigenvalue as color in order to fully represent symmetric tensor data along hyperstreamline trajectories. Sometimes we can modify the color coding scheme to reveal other aspects of the data. An example is the color coding function of Equation 3.4 which decouples pressure and kinetic energy density when visualizing reversible momentum transfers in a flow. For stresses in solids or viscous stresses in fluids, color can be used to discriminate between compressive and tensile directions in the cross-section of a tube. This is done by coloring the tube according to

$$\text{color} \sim \cos\varphi \tag{3.5}$$

where φ is the angle between the normal $\vec{n}$ to the elliptical cross-section of a tube and the force $\vec{f} = \mathbf{T}\vec{n}$ acting on it—i.e.,

$$\cos\varphi = \frac{\vec{n} \cdot (\mathbf{T}\vec{n})}{|\vec{n}||\mathbf{T}\vec{n}|}$$

Figure 3.9 represents the same minor tube as in Figure 3.7, but colored according to Equation 3.5. Red corresponds to $\varphi = 0°$; it indicates that the corresponding

Figure 3.8: Reversible momentum flux density tensor in the flow past a hemisphere cylinder. Color scale 1 of Figure A.3 is used.

Figure 3.9: The minor tube of Figure 3.7 colored as a function of the normal stress. Color scale 2 of Figure A.3 is used.

directions $\vec{n}$ are in pure tension. Green reveals pure shear ($\varphi = 90°$), and blue indicates purely compressive directions ($\varphi = 180°$).

When using the color function of Equation 3.5 for other tensor data, the meaning of compressive and tensile directions is lost. However, this scheme still encodes the sign of the transverse eigenvalues; a principal direction of the elliptical cross-section is red if the corresponding eigenvalue is positive, and blue if otherwise.

3.4 Solenoidal Tensor Fields

In this section, we consider hyperstreamlines colored in function of the longitudinal eigenvalue. In some tensor fields color then captures the behavior of neighboring trajectories; variations of the longitudinal eigenvalue along a trajectory reflect the local geometry of a surrounding hyperstreamline bundle. We call these tensor fields "solenoidal" because their hyperstreamlines have properties similar to those of streamlines in solenoidal vector fields.

A n-dimensional vector field $\vec{v}(\vec{x}) : E \subset \mathbf{R}^n \to \mathbf{R}^n$ is solenoidal iff it is divergence-free—i.e.,

$$\sum_{i=1}^{n} \frac{\partial v_i}{\partial x_i} = 0$$

Examples of 3-D solenoidal vector fields include the velocity in incompressible flows (conservation of mass) and the vorticity. Much of the structure of solenoidal vector fields derives from their property of having a constant flux inside a streamtube; the vector magnitude increases in regions where streamlines converge towards each other and decreases where streamlines diverge from each other. A similar property holds for hyperstreamlines of solenoidal tensor fields, which we define as follows:

Definition 4 (Solenoidal Tensor Fields) *Let* $\mathbf{T} \in C^1(E)$*, where* E *is an open subset of* $\mathbf{R}^n$*, be a symmetric tensor field with Cartesian components* $T_{ij} = T_{ji}$*,* $i, j = 1, \ldots, n$*.* $\mathbf{T}$ *is a solenoidal tensor field iff the* n *conditions*

$$\sum_{i=1}^{n} \frac{\partial T_{ij}}{\partial x_i} = 0 \quad j = 1, \ldots, n \tag{3.6}$$

are satisfied across E*.*

Equations 3.6 imply that the n vector fields obtained by multiplying $\mathbf{T}$ with n constant, orthogonal directions, are solenoidal vector fields.

Solenoidal tensor fields are not rare mathematical objects. Rather they are fundamental to fluid and solid-state mechanics. For example, the stress tensor σ_{ij} in solids at rest (in regions where no external forces are applied) and the momentum-flux-density tensor Π_{ij} in gravity-free,[3] steady-state flows (Table 1.2) both satisfy Equations 3.6 and are solenoidal tensor fields. In the latter case, Equations 3.6 are equivalent to the Navier-Stokes equations expressing the conservation of momentum (Equations 1.2). In ideal flows, Equations 3.6 reduce to the Euler's equations (Equation 1.1) that govern the reversible momentum-flux-density tensor, Π^r_{ij} (Table 1.2). Stresses and viscous stresses in flows, however, are not solenoidal.

Hyperstreamlines of solenoidal tensor fields have a convergence/divergence property similar to the property of streamlines in solenoidal vector fields. We analyze this property in two and three dimensions, respectively.

3.4.1 2-D Solenoidal Tensor Fields

The following theorem rules the behavior of hyperstreamlines in 2-D solenoidal tensor fields.

Theorem 1 *Let $\mathbf{T} \in C^1(E)$ be a 2-D solenoidal tensor field, where E is an open subset of $\mathbf{R}^2$. Consider the set $\mathcal{HS}_l$ of hyperstreamlines propagating along the eigenvector field $\vec{v}_l = \lambda_l \vec{e}_l$. Then, in regions of E where it is possible to continuously confer a sign to the eigenvectors,*

$$\frac{\partial \lambda_l}{\partial s_l} = K_{lt}(\lambda_l - \lambda_t) \tag{3.7}$$

where λ_l is the longitudinal eigenvalue, λ_t the transverse eigenvalue, and $\frac{\partial \lambda_l}{\partial s_l}$ represents variations of the longitudinal eigenvalue along trajectories in $\mathcal{HS}_l$. K_{lt} is positive in regions where hyperstreamlines in $\mathcal{HS}_l$ converge towards each other and negative in regions where they diverge from each other (Figure 3.10).

[3] Assuming no gravity is common practice when computing gas flows.

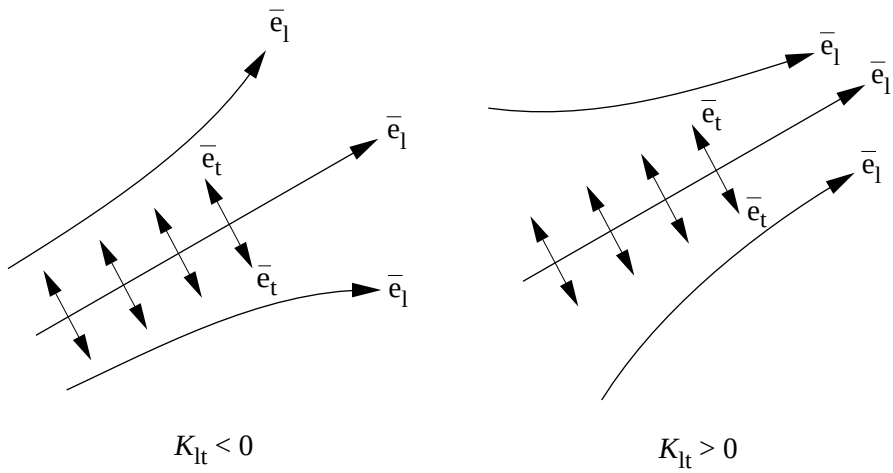

Figure 3.10: Sign of the geometric factor K_{lt} for 2-D solenoidal tensor fields.

We do not provide an explicit proof here, as Theorem 1 is a particular case of Theorem 2 that handles 3-D solenoidal tensor fields. The proof of Theorem 2, which is to be given in Section 3.4.2, requires the ability to continuously confer a sign to the eigenvectors. Equation 3.7, however, is consistent with the sign indeterminacy of eigenvectors: inverting the direction of propagation of the hyperstreamlines in $\mathcal{HS}_l$ changes the sign both of the partial derivative and of K_{lt} (converging hyperstreamlines become diverging, and vice versa).

Equation 3.7 explains some of the structure of 2-D solenoidal tensor fields, showing behavioral analogies between hyperstreamlines of solenoidal tensor fields and streamlines of solenoidal vector fields. Indeed, major hyperstreamlines are characterized by $\lambda_l - \lambda_t > 0$; they converge towards each other ($K_{lt} > 0$) in regions where the longitudinal (major) eigenvalue increases during propagation ($\frac{\partial \lambda_l}{\partial s_l} > 0$), and they diverge ($K_{lt} < 0$) where the longitudinal eigenvalue decreases ($\frac{\partial \lambda_l}{\partial s_l} < 0$). Conversely, minor hyperstreamlines, which are characterized by $\lambda_l - \lambda_t < 0$, converge where the longitudinal (minor) eigenvalue decreases and diverge where the longitudinal eigenvalue increases. This behavior is summarized in Table 3.1.

Figure 3.11: Major (left) and minor (right) eigenvectors of a solenoidal tensor field. Color encodes the longitudinal eigenvalue. Increasing values correspond to color shifts from blue to green, yellow, orange, and red (color scale 2 of Figure A.3).

Longitudinal Eigenvalue	Hyperstreamline Type major	minor
increasing	converging	diverging
decreasing	diverging	converging

Table 3.1: Behavior of hyperstreamlines in 2-D solenoidal tensor fields.

Figure 3.11 shows an example. Textures visualize the solenoidal behavior of

$$\mathbf{T}(x,y) = \begin{pmatrix} \cos y(\sin x + \cos y) & \cos x(\frac{1}{\pi}\sin x - \sin y) \\ \cos x(\frac{1}{\pi}\sin x - \sin y) & \sin x \cos y - \frac{1}{\pi} y \cos 2x \end{pmatrix}$$

for $-\pi \leq x, y \leq \pi$. Major trajectories (left texture) converge in regions of increasing major eigenvalue (color shifts from blue to red) and diverge where the major eigenvalue decreases (color shifts from red to blue). The minor eigenvector field (right texture) adopts an opposite behavior in accordance with Equation 3.7.

A topological consequence of Theorem 1 is that limit cycles cannot occur in solenoidal tensor fields—a result to be proven in Section 4.3.5.

3.4.2 3-D Solenoidal Tensor Fields

The following theorem establishes a corresponding property for hyperstreamlines of 3-D solenoidal tensor fields.

Theorem 2 *Let $\mathbf{T} \in C^1(E)$ be a 3-D solenoidal tensor field, where E is an open subset of $\mathbf{R}^3$. Consider the set $\mathcal{HS}_l$ of hyperstreamlines propagating along the eigenvector field $\vec{v}_l = \lambda_l \vec{e}_l$. Then, in regions of E where it is possible to continuously confer a sign to the eigenvectors,*

$$\frac{\partial \lambda_l}{\partial s_l} = K_{lt_1}(\lambda_l - \lambda_{t_1}) + K_{lt_2}(\lambda_l - \lambda_{t_2}) \tag{3.8}$$

where λ_l is the longitudinal eigenvalue, λ_{t_1} and λ_{t_2} are the transverse eigenvalues, and $\frac{\partial \lambda_l}{\partial s_l}$ represents variations of the longitudinal eigenvalue along hyperstreamline trajectories in $\mathcal{HS}_l$. As shown in Figure 3.12, the factor K_{lt_i}, $i = 1$ or 2, is positive in regions where neighboring hyperstreamlines that belong to $\mathcal{HS}_l$ and that are located

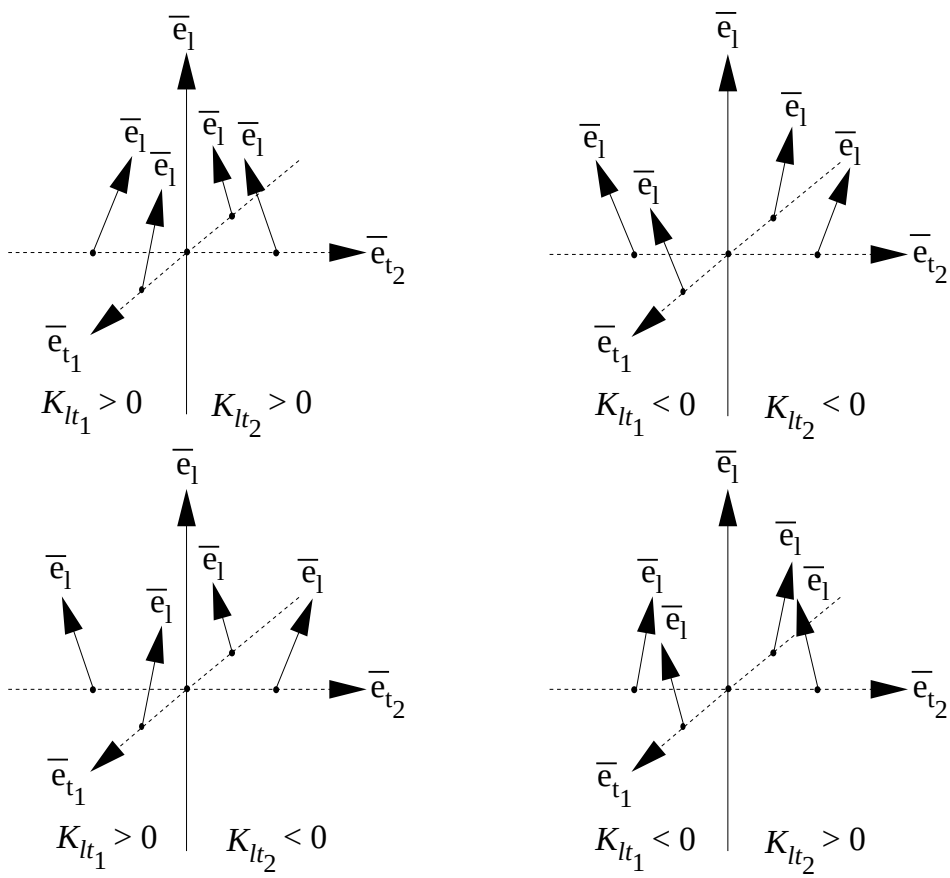

Figure 3.12: Sign of the geometric factors K_{lt_i}, $i = 1, 2$.

a small distance away along the transverse eigendirection $\vec{e}_{t_i}$, converge towards each other. Likewise, K_{lt_i} is negative if these hyperstreamlines diverge from each other.

Proof. Consider a solenoidal tensor field $\mathbf{T}$ whose components T_{ij}, $i,j = 1,2,3$, obey Equations 3.6. Let β_{ij}, $i,j = 1,2,3$, be the orthonormal transformation that diagonalizes $\mathbf{T}$. The coefficients β_{ij} obey

$$\sum_{i=1}^{3} \beta_{ip}\beta_{iq} = \sum_{i=1}^{3} \beta_{pi}\beta_{qi} = \delta_{pq} \tag{3.9}$$

The components of $\mathbf{T}$ transform according to Equation 1.3, so

$$T'_{ij} = \sum_{p,q=1}^{3} \beta_{ip}\beta_{jq}T_{pq}$$

This relation can be inverted using Equations 3.9 to yield

$$T_{ij} = \sum_{p,q=1}^{3} \beta_{pi}\beta_{qj}T'_{pq}$$

After differentiating with respect to the coordinate x_i and summing over the index i, we obtain

$$\sum_{i=1}^{3} \frac{\partial T_{ij}}{\partial x_i} = \sum_{i,p,q=1}^{3} \frac{\partial \beta_{pi}}{\partial x_i}\beta_{qj}T'_{pq} + \sum_{i,p,q=1}^{3} \beta_{pi}\frac{\partial \beta_{qj}}{\partial x_i}T'_{pq} + \sum_{i,p,q=1}^{3} \beta_{pi}\beta_{qj}\frac{\partial T'_{pq}}{\partial x_i}$$

The left-hand side vanishes identically because $\mathbf{T}$ is solenoidal (Equations 3.6). Also, since the transformation β_{ij} diagonalizes $\mathbf{T}$,

$$T'_{pq} = \lambda_p \delta_{pq}$$

where λ_p, $p = 1,2,3$, are the eigenvalues. (No specific ordering of the eigenvalues is assumed yet.) It follows that

$$0 = \sum_{i,p=1}^{3} \frac{\partial \beta_{pi}}{\partial x_i}\beta_{pj}\lambda_p + \sum_{i,p=1}^{3} \beta_{pi}\frac{\partial \beta_{pj}}{\partial x_i}\lambda_p + \sum_{i,p=1}^{3} \beta_{pi}\beta_{pj}\frac{\partial \lambda_p}{\partial x_i}$$

After multiplying both sides by β_{qj}, summing over the index j, and using Equations 3.9, we obtain

$$0 = \sum_{i,p=1}^{3} \frac{\partial \beta_{pi}}{\partial x_i}\delta_{pq}\lambda_p + \sum_{i,p=1}^{3} \beta_{pi}\frac{\partial \beta_{pj}}{\partial x_i}\beta_{qj}\lambda_p + \sum_{i,p=1}^{3} \beta_{pi}\delta_{pq}\frac{\partial \lambda_p}{\partial x_i}$$

which is equivalent to

$$\sum_{i=1}^{3} \beta_{qi} \frac{\partial \lambda_q}{\partial x_i} = -\sum_{i=1}^{3} \frac{\partial \beta_{qi}}{\partial x_i} \lambda_q - \sum_{i,j,p=1}^{3} \beta_{pi} \beta_{qj} \frac{\partial \beta_{pj}}{\partial x_i} \lambda_p \tag{3.10}$$

Consider hyperstreamlines that belong to the set $\mathcal{HS}_l$—i.e., hyperstreamlines that propagate along the eigenvector field $\vec{e}_l$. Let $\vec{e}_{t_1}$ and $\vec{e}_{t_2}$ be the transverse eigenvectors. The sign of the eigenvectors is fundamentally indeterminate but we assume that, in the region of interest, we can confer a sign to the eigenvectors such that the resulting, signed vectors are continuous. The net effect is to impose a direction of propagation on the hyperstreamlines in $\mathcal{HS}_l$ and to orient the transverse eigendirections. Without loss of generality, we select the sign of the eigenvectors such that the orthonormal basis $\{\vec{e}_{t_1}, \vec{e}_{t_2}, \vec{e}_l\}$ is right-handed; that is,

$$\begin{aligned} \vec{e}_{t_1} &= \vec{e}_{t_2} \times \vec{e}_l \\ \vec{e}_{t_2} &= \vec{e}_l \times \vec{e}_{t_1} \\ \vec{e}_l &= \vec{e}_{t_1} \times \vec{e}_{t_2} \end{aligned} \tag{3.11}$$

The coefficients β_{ij} are the Cartesian components of the eigenvector fields, so

$$\vec{e}_p = \sum_{i=1}^{3} \beta_{pi} \vec{1}_i$$

where the vectors $\vec{1}_i$ are unit vectors lying along the coordinate axes. Equation 3.10 is therefore equivalent to

$$\vec{e}_q \cdot \vec{\nabla} \lambda_q = -\lambda_q \vec{\nabla} \cdot \vec{e}_q - \sum_{p=1}^{3} \lambda_p \vec{e}_q \cdot (\vec{e}_p \cdot \vec{\nabla}) \vec{e}_p$$

In particular, for $q = l$ and for p running across t_1, t_2, and l,

$$\vec{e}_l \cdot \vec{\nabla} \lambda_l = -\lambda_l \vec{\nabla} \cdot \vec{e}_l - \lambda_{t_1} \vec{e}_l \cdot (\vec{e}_{t_1} \cdot \vec{\nabla}) \vec{e}_{t_1} - \lambda_{t_2} \vec{e}_l \cdot (\vec{e}_{t_2} \cdot \vec{\nabla}) \vec{e}_{t_2} - \lambda_l \vec{e}_l \cdot (\vec{e}_l \cdot \vec{\nabla}) \vec{e}_l \tag{3.12}$$

The left-hand side is the derivative of the longitudinal eigenvalue, λ_l, along trajectories in $\mathcal{HS}_l$. We can rewrite it as

$$\frac{\partial \lambda_l}{\partial s_l}$$

where s_l is the arc length along hyperstreamline trajectories in $\mathcal{HS}_l$. The three vectors $\vec{e}_p$, $p = t_1, t_2, l$, have constant magnitude, so

$$\vec{e}_p \cdot \vec{e}_p = 1$$

and the following identity holds true:[4]

$$0 = \vec{\nabla}(\vec{e}_p \cdot \vec{e}_p) = 2\vec{e}_p \times (\vec{\nabla} \times \vec{e}_p) + 2(\vec{e}_p \cdot \vec{\nabla})\vec{e}_p$$

That is,

$$(\vec{e}_p \cdot \vec{\nabla})\vec{e}_p = (\vec{\nabla} \times \vec{e}_p) \times \vec{e}_p$$

It follows that

$$\vec{e}_l \cdot (\vec{e}_l \cdot \vec{\nabla})\vec{e}_l = 0$$

so Equation 3.12 is reduced to

$$\frac{\partial \lambda_l}{\partial s_l} = -\lambda_l \vec{\nabla} \cdot \vec{e}_l - \lambda_{t_1} \vec{e}_l \cdot (\vec{e}_{t_1} \cdot \vec{\nabla})\vec{e}_{t_1} - \lambda_{t_2} \vec{e}_l \cdot (\vec{e}_{t_2} \cdot \vec{\nabla})\vec{e}_{t_2} \tag{3.13}$$

Next, we transform the first term on the right-hand side by using Equations 3.11:[5]

$$\begin{aligned}
\vec{\nabla} \cdot \vec{e}_l &= \vec{\nabla} \cdot (\vec{e}_{t_1} \times \vec{e}_{t_2}) \\
&= \vec{e}_{t_2} \cdot (\vec{\nabla} \times \vec{e}_{t_1}) - \vec{e}_{t_1} \cdot (\vec{\nabla} \times \vec{e}_{t_2}) \\
&= (\vec{e}_l \times \vec{e}_{t_1}) \cdot (\vec{\nabla} \times \vec{e}_{t_1}) - (\vec{e}_{t_2} \times \vec{e}_l) \cdot (\vec{\nabla} \times \vec{e}_{t_2}) \\
&= -\vec{e}_l \cdot ((\vec{\nabla} \times \vec{e}_{t_1}) \times \vec{e}_{t_1}) - \vec{e}_l \cdot ((\vec{\nabla} \times \vec{e}_{t_2}) \times \vec{e}_{t_2}) \\
&= -\vec{e}_l \cdot (\vec{e}_{t_1} \cdot \vec{\nabla})\vec{e}_{t_1} - \vec{e}_l \cdot (\vec{e}_{t_2} \cdot \vec{\nabla})\vec{e}_{t_2}
\end{aligned}$$

Thus, Equation 3.13 is reduced to

$$\frac{\partial \lambda_l}{\partial s_l} = (\lambda_l - \lambda_{t_1})\vec{e}_l \cdot (\vec{e}_{t_1} \cdot \vec{\nabla})\vec{e}_{t_1} + (\lambda_l - \lambda_{t_2})\vec{e}_l \cdot (\vec{e}_{t_2} \cdot \vec{\nabla})\vec{e}_{t_2}$$

---

[4] We use the vector identity:

$$\vec{\nabla}(\vec{a} \cdot \vec{b}) = \vec{a} \times (\vec{\nabla} \times \vec{b}) + \vec{b} \times (\vec{\nabla} \times \vec{a}) + (\vec{a} \cdot \vec{\nabla})\vec{b} + (\vec{b} \cdot \vec{\nabla})\vec{a}$$

[5] We use the vector identity

$$\vec{\nabla}(\vec{a} \times \vec{b}) = \vec{b} \cdot (\vec{\nabla} \times \vec{a}) - \vec{a} \cdot (\vec{\nabla} \times \vec{b})$$

which is equivalent to Equation 3.8. The geometric factors K_{lt_i} are given by

$$K_{lt_i} = \vec{e}_l \cdot (\vec{e}_{t_i} \cdot \vec{\nabla})\vec{e}_{t_i} \quad (i = 1, 2) \tag{3.14}$$

To complete the proof of Theorem 2, it remains that we elicit the relation between the sign of the geometric factors K_{lt_i} and the convergence/divergence of neighboring hyperstreamlines (Figure 3.12). The eigenvectors have a constant magnitude ($\vec{e}_p \cdot \vec{e}_p = 1$) so $\vec{e}_p \cdot \vec{d}e_p = 0$ for $p = t_1, t_2, l$. It follows that we can express the differential of $\vec{e}_p$ as

$$\vec{d}e_p = \vec{d}\omega \times \vec{e}_p$$

where $\vec{d}\omega$ is the differential rotation vector of the basis $\{\vec{e}_{t_1}, \vec{e}_{t_2}, \vec{e}_l\}$. ($\vec{d}\omega$ is the same vector for all three eigenvectors because they must remain orthogonal to each other.) The factors in Equation 3.14 become

$$\begin{aligned} K_{lt_i} &= \vec{e}_l \cdot \frac{\partial \vec{e}_{t_i}}{\partial s_{t_i}} \\ &= \vec{e}_l \cdot (\frac{\partial \vec{\omega}}{\partial s_{t_i}} \times \vec{e}_{t_i}) \\ &= (\vec{e}_{t_i} \times \vec{e}_l) \cdot \frac{\partial \vec{\omega}}{\partial s_{t_i}} \end{aligned}$$

where s_{t_i} stands for the arc length in the direction of the transverse eigenvector $\vec{e}_{t_i}$. Using Equations 3.11,

$$K_{lt_1} = -\frac{\partial \omega_{t_2}}{\partial s_{t_1}} \tag{3.15}$$

and

$$K_{lt_2} = \frac{\partial \omega_{t_1}}{\partial s_{t_2}} \tag{3.16}$$

where $d\omega_{t_1}$ and $d\omega_{t_2}$ are differential rotation components along the transverse eigenvectors $\vec{e}_{t_1}$ and $\vec{e}_{t_2}$, respectively. Equations 3.15 and 3.16 clarify the relation between the sign of the factors K_{lt_i} and the convergence/divergence of neighboring hyperstreamlines. As shown in Figure 3.13, the coefficients K_{lt_i}, $i = 1, 2$, are positive if neighboring hyperstreamlines that belong to $\mathcal{HS}_l$ and that are located a small distance away along the transverse eigendirection $\vec{e}_{t_i}$, are converging. Likewise, other cases in

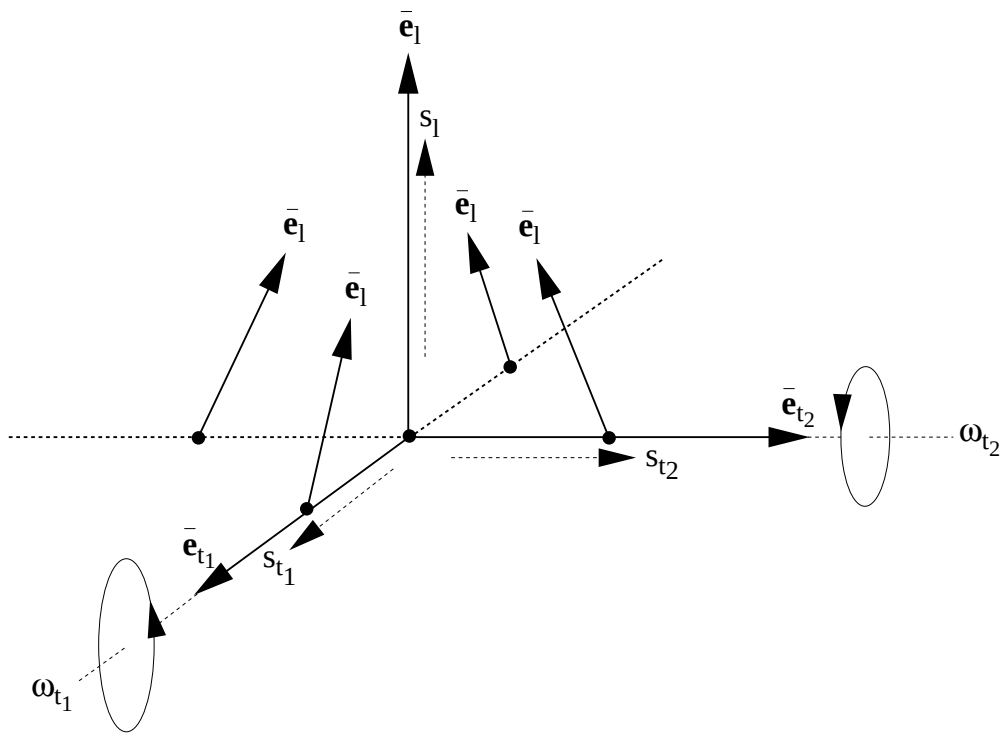

Figure 3.13: Rotation of the orthonormal eigenvector basis.

Figure 3.12, where hyperstreamlines diverge in at least one transverse eigendirection, correspond to at least one negative K_{lt_i} factor.

This completes the proof. □

Practical consequences of Equation 3.8 are as follows. In regions where the longitudinal eigenvalue of major hyperstreamlines increases during propagation ($\frac{\partial \lambda_l}{\partial s_l} > 0$), neighboring major hyperstreamlines converge towards each other. Any divergence in a transverse eigendirection, $\vec{e}_{t_1}$ or $\vec{e}_{t_2}$, must be compensated by a stronger convergence in the other transverse eigendirection. Conversely, a decreasing longitudinal eigenvalue is associated with globally diverging major hyperstreamlines. The opposite property holds true for minor hyperstreamlines: an increasing longitudinal eigenvalue correlates with a global divergence of neighboring minor hyperstreamlines; if they converge in a transverse eigendirection, then they even more strongly diverge in the other transverse eigendirection. Conversely, a decreasing longitudinal eigenvalue corresponds to globally converging minor hyperstreamlines. The behavior of medium

hyperstreamlines is intermediate, the two eigenvalue differences in the right-hand side of Equation 3.8 having a different sign. Here, variations of the longitudinal eigenvalue are determined by the strength of the convergence/divergence of neighboring hyperstreamlines (i.e., the coefficients K_{lt_1} and K_{lt_2}) measured against the eigenvalue differences $\lambda_l - \lambda_{t_1}$ and $\lambda_l - \lambda_{t_2}$.

Figure 3.14 illustrates the solenoidal property of major tubes of the momentum-flux-density tensor in one region of the flow past a hemisphere cylinder. The decrease of the longitudinal eigenvalue (color) is accompanied by diverging trajectories, in accordance to Equation 3.8.

The solenoidal character of the stress-tensor in solids at rest explains why minor hyperstreamlines in Figure 3.6 converge towards the applied forces (quickly decreasing longitudinal eigenvalue) and why major hyperstreamlines propagate mostly parallel to each other with an almost constant color. A close view of the sudden divergence of minor hyperstreamlines on one side of the plane of symmetry is given in Figure 3.15. The local divergence of minor trajectories creates a sudden increase of the longitudinal eigenvalue— a fact that is counterintuitive to the assumption that the minor eigenvalue should decrease uniformly when approaching one of the two applied compressive forces.

Another example is given in Figure 3.16 that shows a rake of major tubes of the momentum-flux-density tensor Π in the flow past an ogive cylinder. The air flow comes in from a direction 5° to the left of the ogive axis, inducing vortices in the wake of the body. Major tubes that become entangled in the vortices undergo a fast decrease in color while diverging from each other. In other regions of the flow, the color is constant and, in some places, it even increases slightly from orange to red. In these regions, the apparent divergence of the tubes in the direction parallel to the surface of the body is compensated by a stronger convergence in the perpendicular direction. Both divergence and convergence compensate each other exactly in the tail between the two vortices.

Figure 3.14: Major tubes illustrating the solenoidal property of the momentum-flux-density tensor in one region of the flow past a hemisphere cylinder. Color scale 1 of Figure A.3 is used.

Figure 3.15: Close view of the sudden divergence of minor hyperstreamlines on one side of the plane of symmetry in Figure 3.6. Color scale 1 of Figure A.3 is used.

Figure 3.16: Rake of major tubes of the momentum-flux-density tensor in the flow past an ogive cylinder. Color scale 1 of Figure A.3 is used.

3.5 Asymmetric Tensor Fields

Hyperstreamlines are useful to visualize symmetric tensor fields whose eigenvectors $\vec{v}_i$ are real and orthogonal. Visualizing asymmetric tensor fields is more challenging because of the possible occurrence of complex and non-orthogonal eigenvectors.

In this section, we design line icons for continuous, 3-D asymmetric tensor data. (The same methodology can be applied for 2-D asymmetric tensor fields.) The underlying philosophy is similar to hyperstreamlines of symmetric tensor data, and the goal is to fully render asymmetric tensor information along continuous trajectories. Although local vector icons—such as streamribbons and streamtubes—reveal some aspects of vector gradients (Section 2.2.2), they can not be used for more general asymmetric tensor data. (Even with vector gradients, they render tensor information only partially.) In the following, we discuss line icons obtained by decomposing asymmetric tensor data into two components—a symmetric tensor field and a vector field. We visualize the symmetric tensor component with hyperstreamlines as before, but we encode the additional vector field along the trajectory. Depending on the nature of the data, two reductions are possible: symmetric/antisymmetric or polar decomposition.

3.5.1 Symmetric/Antisymmetric Decomposition

A asymmetric tensor field can be decomposed into the sum of symmetric and antisymmetric components according to

$$\mathbf{T} = \frac{\mathbf{T} + \mathbf{T}^t}{2} + \frac{\mathbf{T} - \mathbf{T}^t}{2}$$

where $\mathbf{T}^t$ is the transpose of $\mathbf{T}$. The antisymmetric tensor has only three independent components that form a vector known as "axial vector."[6]

Figure 3.17 (top) shows a line icon for asymmetric data based on this decomposition. A hyperstreamline is integrated along one eigenvector of the symmetric tensor

[6]The antisymmetric tensor field

$$\mathbf{T} = \begin{pmatrix} 0 & -\omega_3 & \omega_2 \\ \omega_3 & 0 & -\omega_1 \\ -\omega_2 & \omega_1 & 0 \end{pmatrix}$$

Figure 3.17: Examples of line icons for 3-D asymmetric tensor fields. Symmetric/anti-symmetric decomposition (top) and polar decomposition (bottom). Color scales 1 and 2 of Figure A.3 are used for tubes and ribbons, respectively.

component; it can be color-coded either according to the longitudinal eigenvalue, or as in Equation 3.5. An additional ribbon is added outside the tube's surface so as to represent the axial vector. The ribbon position and width locally encode the vector component which is perpendicular to the trajectory. The ribbon color maps the angle between the axial vector and the direction of propagation according to color scale 2 of Figure A.3 (red is parallel, green is perpendicular, and blue is antiparallel). In Figure 3.17 (top), for example, the vector field is everywhere close to alignment with the direction of propagation. It is not, however, exactly aligned because the ribbon has a finite width.

In fluid flows, this icon may be used to visualize velocity gradients, which are the sum of the rate-of-strain tensor ϵ_{ik} (symmetric) and the rate-of-rotation tensor (antisymmetric). The latter corresponds to half the vorticity vector (Table 1.2). In this case, the ribbon shows the position of vorticity with respect to principal strains—a parameter allegedly important for understanding turbulence (Reference [66]).

3.5.2 Polar Decomposition

An alternative way of reducing asymmetric data is the polar decomposition (Reference [67]), which generalizes to tensors (or matrices in general) the decomposition of complex numbers into the product of their amplitude and phase factor. Assume as in Figure 3.18 that the tensor $\mathbf{T}$ at a given point $\vec{x}$ maps the vertices of a cube from an initial state to a final, deformed state. This global deformation can be decomposed into more elementary transformations. For example, one can reach the final state by first stretching the cube by a deformation $\mathbf{U}$ and then rotating the stretched rhomboid by an isometric transformation $\mathbf{Q}$. Alternatively, one can first rotate the cube and then stretch it by a tensor $\mathbf{V}$.

Mathematically, there are two equivalent ways of decomposing asymmetric tensor

---

is equivalent to the vector field

$$\vec{v} = \begin{pmatrix} \omega_1 \\ \omega_2 \\ \omega_3 \end{pmatrix}$$

in the sense that ω_1, ω_2, and ω_3 transform as the components of a vector field.

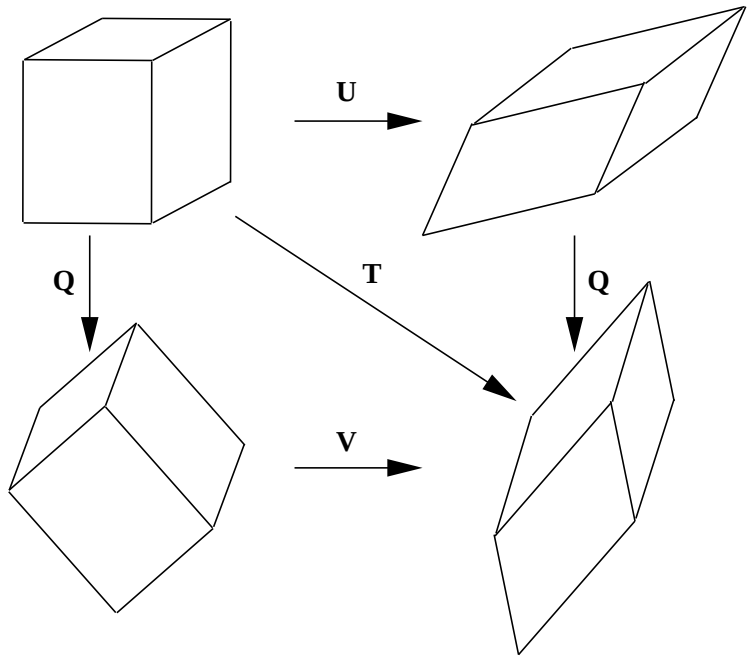

Figure 3.18: Polar Decomposition of asymmetric data.

data into the product of a stretch tensor (amplitude) and an isometric transformation (phase):

$$\mathbf{T} = \mathbf{Q}\mathbf{U} = \mathbf{V}\mathbf{Q} \tag{3.17}$$

where both $\mathbf{U} = \sqrt{\mathbf{T}^t\mathbf{T}}$ and $\mathbf{V} = \sqrt{\mathbf{T}\mathbf{T}^t}$ are symmetric positive definite tensors, and $\mathbf{Q} = \mathbf{T}\mathbf{U}^{-1}$ is an orthonormal tensor ($\mathbf{Q}^{-1} = \mathbf{Q}^t$). This decomposition is unique (i.e., there is a one-to-one correspondence between the matrix $\mathbf{T}$ and the set of matrices $\{\mathbf{Q}, \mathbf{U}, \mathbf{V}\}$) wherever $\det \mathbf{T} \neq 0$. We explain below how we handle points where $\det \mathbf{T} = 0$.

We can focus on the first decomposition in Equation 3.17 without losing generality. Figure 3.17 (bottom) shows a line icon based on this decomposition. The symmetric tensor $\mathbf{U}$ is represented by a tube along one of its eigenvectors. In regions where $\det \mathbf{T} > 0$, the isometric transformation $\mathbf{Q}$ is simply a rotation; it is characterized by an angle θ ($0 \leq \theta \leq \pi$) and a unit axis of rotation $\vec{u}$. Thus, $\mathbf{Q}$ can be represented by the vector

$$\vec{r}_1 = \theta\vec{u}$$

A rotation of angle θ about the axis $\vec{u}$ is physically identical to a rotation of angle $2\pi - \theta$ about the axis $-\vec{u}$. Thus, $\mathbf{Q}$ is also equivalent to the vector

$$\vec{r}_2 = (2\pi - \theta)(-\vec{u})$$

To visualize $\mathbf{Q}$, we add two ribbons that represent the vectors $\vec{r}_1$ and $\vec{r}_2$, respectively. In regions where $\det \mathbf{T} < 0$, the transformation $\mathbf{Q}$ involves an additional inversion in the direction of the rotation axis. A row of white pearls across the ribbons marks the onset of the inversion during propagation, and a row of black pearls indicates its cancellation.

In some points of the trajectory, vectors $\vec{r}_1$ and $\vec{r}_2$ may not be defined. We then simply interpolate them between adjacent points in order to avoid discontinuities of the ribbons. These singular points occur at the pearls, where $\det \mathbf{U} = |\det \mathbf{T}| = 0$ ($\mathbf{U}$ is defined but not invertible and $\mathbf{Q}$ can not be computed), and at points where $\mathbf{Q}$ reduces to plus or minus the identity matrix (the rotation axis $\vec{u}$ is undefined and $\mathbf{T}$ is locally symmetric with all eigenvalues having the same sign). Using polar decomposition to visualize asymmetric tensor data therefore assumes that these singularities

are isolated points along the trajectories.

3.6 Chapter Summary

In this chapter, we discuss elementary icons of tensor fields. After observing the inadequacy of point icons for continuous data, mainly because using them results in severe visual clutter, we design line icons. (Surface icons are yet to be developed.)

First, we consider symmetric tensor fields, which have real and orthogonal eigenvectors. We prove that, if tensor components are continuous and differentiable functions of space, eigenvalues and eigenvectors are continuous and smooth at most points. The only discontinuities arise at points where two or more eigenvalues are degenerate—a topic to be fully discussed in Chapter 4. It follows, then, that in most regions, n-dimensional, continuous, symmetric tensor data are equivalent to a set of n orthogonal families of smooth curves tangent to the eigenvectors. From this observation, we develop line icons that continuously represent eigenvectors, embedding in their very design the underlying continuity of the data.

For 2-D symmetric tensor fields, we generate textures that visualize curves tangent to the eigenvectors. Textures are created by convolving the eigenvector fields with a band-limited noise. They do not require to integrate the eigenvectors, avoiding difficulties related to degenerate eigenvalues. Textures are also space-filling and guarantee the visualization of all data features larger than the noise cutoff frequency. Then, we display full (trivariate) tensor information in a single image, using elevation, color, and texture of a surface, as independent visualization channels.

For 3-D symmetric tensor fields, we define hyperstreamlines—i.e., line icons that encode full tensor information along continuous trajectories (curves tangent to an eigenvector). Hyperstreamlines are obtained by sweeping a geometric primitive along the longitudinal eigenvector, stretching it under the combined action of the transverse eigenvectors, and computing the envelope of the stretched primitives. Tubes and helices are two different types of hyperstreamlines that are obtained by sweeping ellipses and crosses, respectively. The trajectories and color of hyperstreamlines encode the longitudinal eigenvector, and their geometric cross-sections represent the

two transverse eigenvectors. In fluid flows, hyperstreamlines of the reversible momentum-flux-density tensor correlate various quantities—such as velocity direction, pressure, and kinetic energy density. We discuss different color-coding schemes that can reveal other aspects of the data.

Then, we analyze solenoidal tensor fields—such as stresses in solids or momentum flux density in steady-state, gravity-free fluids. Hyperstreamlines of solenoidal tensor fields have geometric properties similar to streamlines of solenoidal vector fields. In short, major (minor) hyperstreamline trajectories globally converge (diverge) when propagating towards regions of increasing longitudinal eigenvalue.

Finally, we design line icons for 3-D asymmetric tensor fields, a case further complicated by the possible occurrence of complex, non-orthogonal eigenvectors. We suggest to use line icons that are obtained by decomposing the data into the sum or the product of a symmetric tensor component and a vector field. Full tensor information can then be continuously represented by adding to hyperstreamlines of the symmetric tensor component, a ribbon that encodes the additional vector field.

Chapter 4

Local and Global Tensor Icons

4.1 Introduction

Visualizing continuous, multivariate data is a difficult challenge mainly because of the necessity to render the underlying continuity of the data while avoiding problems related to visual clutter. We discuss in Chapter 2 the importance of this dichotomy for our ability to understand graphical displays of vector fields. Due to the greater multivariate nature of tensor fields, difficulties associated with visual clutter are enhanced.

In Chapter 3, we define hyperstreamlines—i.e., icons geometrically encoding tensor data along continuous trajectories—and we show that, when compared to point icons, hyperstreamlines greatly improve the perception of the continuity in the data. However, hyperstreamlines merely sample the tensor field along their trajectories. In general, too many hyperstreamlines are required for understanding the global structure of tensor fields without ambiguity, and the display becomes overly cluttered.

In this chapter, we define and analyze the topology of second-order tensor fields. As with vector fields, we derive a set of carefully chosen points and lines that embed global information about tensor fields—i.e., we represent schematically the collective behavior of an infinite collection of (undrawn) hyperstreamlines. The goal is to reveal the global structure of tensor data that is otherwise buried within excessive multivariate information. It results in a simple and austere depiction that allows an

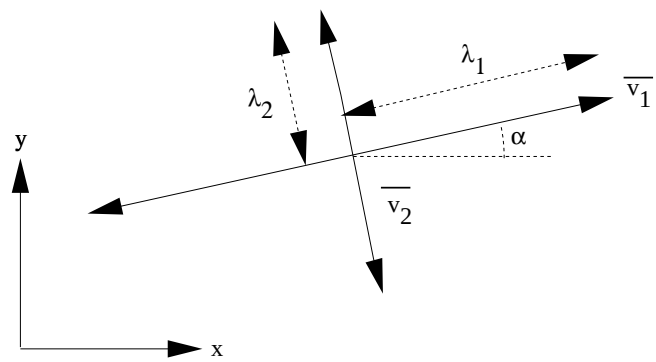

Figure 4.1: The two orthogonal eigenvector fields $\vec{v}_i$, represented as bidirectional arrows.

observer to infer the behavior of any hyperstreamlines in the field and comprehend the structure of the entire data set.

The present work is to our knowledge the first attempt at defining and analyzing the topology of second-order tensor fields; all the concepts to be developed in the course of this chapter are original. However, fields such as dynamical systems and geometric approaches to solving differential equations provide some guidance and appropriate vocabularies. In particular, the texts by A. A. Andronov et *al.* (Reference [68]) and L. Perko (Reference [69]) have been influential in structuring our thinking.

4.1.1 Investigated Data

We discuss the topology of 2-D symmetric tensor fields in all but the last sections of this chapter. That is, we analyze trivariate data that are similar to Equation 1.4 (Section 1.2). These data are fully equivalent to two orthogonal eigenvector fields

$$\vec{v}_i = \lambda_i \vec{e}_i \tag{4.1}$$

where $i = 1, 2$ (Figure 4.1). λ_i, $i = 1, 2$, are the eigenvalues and $\vec{e}_i$, $i = 1, 2$, the associated unit eigenvectors. As usual, the eigenvalues are numbered as $\lambda_1 \geq \lambda_2$. Figure 4.1

represents $\vec{v}_1$ and $\vec{v}_2$ as bidirectional arrows because of the sign indeterminacy of the eigenvectors.

At the end of this chapter, we discuss 3-D symmetric tensor data, such as Equation 1.6 (Section 1.2), to which correspond three orthogonal eigenvectors

$$\vec{v}_i = \lambda_i \vec{e}_i$$

where $i = 1, 2, 3$. Again, the three eigenvalues are numbered as $\lambda_1 \geq \lambda_2 \geq \lambda_3$.

Although we focus the discussion on symmetric tensor fields, we can use the results of this chapter and the decomposition schemes of Section 3.5 to analyze the structure of asymmetric data.

4.1.2 Degenerate Points

In Section 3.1, we show the analogy between a symmetric tensor field and a set of orthogonal families of trajectories that are continuous, smooth, and that do not intersect each other. This analogy was shown to hold "almost everywhere." Here, we focus on those very points where the analogy ceases to exist. We call these points "degenerate points."

Definition 5 (Degenerate Point) *A degenerate point of a tensor field* $\mathbf{T} : E \rightarrow \mathcal{L}(\mathbf{R}^n, \mathbf{R}^n)$*, where* E *is an open subset of* $\mathbf{R}^n$*, is a point* $\vec{x}_0 \in E$ *where at least two of the* n *eigenvalues of* $\mathbf{T}$ *are equal to each other.*

In the case of 2-D tensor fields, $\vec{x}_0$ is a degenerate point iff $\lambda_1(\vec{x}_0) = \lambda_2(\vec{x}_0)$. For 3-D tensor fields, various types of degenerate points exist, corresponding to the conditions $\lambda_1(\vec{x}_0) = \lambda_2(\vec{x}_0)$, $\lambda_2(\vec{x}_0) = \lambda_3(\vec{x}_0)$, or $\lambda_1(\vec{x}_0) = \lambda_2(\vec{x}_0) = \lambda_3(\vec{x}_0)$.

Degenerate points play a similar role as critical points in vector fields; they are the basic singularities underlying the topology of tensor fields. Indeed, streamlines in vector fields never cross each other except at critical points. Likewise, hyperstreamlines in tensor fields meet each other only at degenerate points. To show this, consider a 2-D tensor field and denote by λ the common eigenvalue at a degenerate point $\vec{x}_0$.

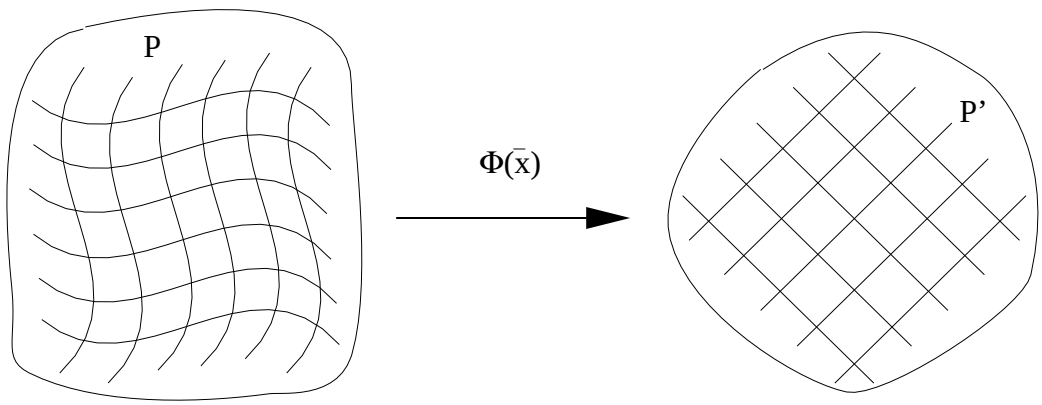

Figure 4.2: Away from degenerate points, continuous and symmetric tensor fields are diffeomorphic to constant data.

At $\vec{x}_0$, the tensor field is proportional to the identity matrix:

$$\mathbf{T}(\vec{x}_0) = \begin{pmatrix} \lambda & 0 \\ 0 & \lambda \end{pmatrix} \tag{4.2}$$

which implies that $\mathbf{T}(\vec{x}_0)\vec{e} = \lambda\vec{e}$ for every vector $\vec{e}$. At most points, there is only one eigenvector associated with each eigenvalue, but at degenerate points, there are an infinity of eigenvectors corresponding to the degenerate eigenvalues. So degenerate points are the only places where hyperstreamlines cross each other. As shown by Equation 4.2, degenerate points of 2-D symmetric tensor fields satisfy the conditions[1]

$$\begin{cases} T_{11}(\vec{x}_o) - T_{22}(\vec{x}_o) = 0 \\ T_{12}(\vec{x}_o) = 0 \end{cases} \tag{4.3}$$

which we use to locate them. (More on this topic in Appendix B.)

The reader may wonder why do degenerate points matter so much? Because nothing topologically interesting is really happening elsewhere. To see this, recall the analogy between continuous and symmetric tensor fields, and orthogonal families of smooth, continuous, and non-intersecting trajectories. This analogy is shown to hold within regions that do not comprise degenerate points. Within such a region, we can find a diffeomorphism $\Phi(\vec{x})$ that transforms the tensor data into a constant field (Figure 4.2).[2]

[1] Valid in any coordinate system.

[2] For example, $\Phi(\vec{x}) = \beta(\vec{x})\vec{x}$ where $\beta(\vec{x})$ is the orthonormal transformation that diagonalizes the tensor at $\vec{x}$.

4.1.3 Tensor Field Topology

We define the topology of symmetric tensor fields as follows:

Definition 6 (Tensor Field Topology) *The topology of a symmetric tensor field* $\mathbf{T} : E \to \mathcal{L}(\mathbf{R}^n, \mathbf{R}^n)$*, where* E *is an open subset of* $\mathbf{R}^n$*, is the set of* n *topologies of the eigenvector fields* $\vec{v}_i(\vec{x})$*,* $i = 1, \ldots, n$*.*

The primary objects of our study are therefore the eigenvector fields, $\vec{v}_i(\vec{x})$, $i = 1, \ldots, n$. The n related vector topologies are not fully independent as they "connect" at degenerate points. It will also be demonstrated that the sign indeterminacy of the eigenvector fields engenders unfamiliar topological features that cannot be observed in more common, signed, continuous vector fields.

4.1.4 Chapter Content

In the first sections of this chapter, we analyze 2-D symmetric tensor fields (Equation 1.4). In Section 4.2, we develop the topological concept of a "tensor index," which we use in Section 4.3 to analyze local hyperstreamline patterns in the vicinity of degenerate points. We also define in Section 4.3 separatrices and limit cycles of tensor fields—both concepts having their equivalents in vector field topology. We analyze time-dependent tensor data in Section 4.4. In Section 4.5 we consider those particular 3-D tensor fields that are "tangent" to 2-D surfaces embedded in a 3-D space. We derive a rule constraining the topology of such tensors, thereby extending to tensor fields the Poincaré-Hopf theorem for vector fields. In Section 4.6, we develop a theory for general, 3-D symmetric tensor fields (Equation 1.6). Finally, we summarize the results in Section 4.7.

4.2 Theory of the Tensor Index

In order to understand the topology of tensor fields, it is necessary to characterize the local behavior of the data in the vicinity of degenerate points. This is the topic of Section 4.3. As a preliminary step, we study in this section the eigenvector fields along

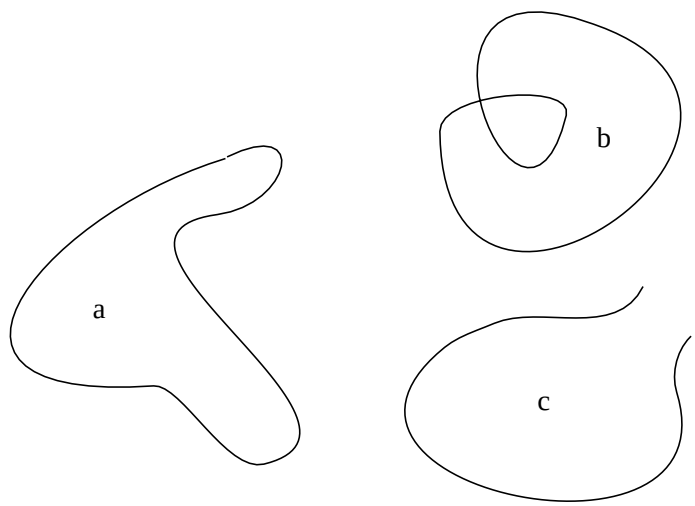

Figure 4.3: a: Jordan curve; b and c: non-Jordan curves.

closed curves surrounding the singularities. We define in Section 4.2.1 the notion of a "tensor index of a curve," and from there on, we derive in Section 4.2.2 the concept of "tensor index at a degenerate point." This concept, which plays a central role in analyzing tensor field topology, extends to tensor fields a familiar notion from vector field topology (References [68, 69]).

The curves under consideration are Jordan curves which are defined below.

Definition 7 (Jordan Curve) *A Jordan curve is a curve which is homeomorphic to a circle—i.e., a piecewise-smooth, simple, closed curve.*

For example, the curve in Figure 4.3 (a) is a Jordan curve. Curves in Figures 4.3 (b) and (c), however, are not Jordan curves because they are not simple and closed, respectively.

4.2.1 Tensor Index of a Jordan Curve

Consider a tensor field $\mathbf{T}(\vec{x})$. We can assign a specific quantity to each Jordan curve lying within $\mathbf{T}$'s domain of definition. We refer to this quantity as the "tensor index

of a curve." A precise definition follows:

Definition 8 (Tensor Index of a Jordan Curve) *Let E be an open set of $\mathbf{R}^2$ and let $L \subset E$ be a Jordan curve. The index $I_{\mathbf{T}}(L)$ of L relative to a tensor field $\mathbf{T} \in C^1(E)$, where $\mathbf{T}$ has no degenerate points on L, is the number of counterclockwise revolutions made by the eigenvectors of $\mathbf{T}$ when traveling once in a counterclockwise direction along L.*

The angle α between the eigenvectors of $\mathbf{T}$ and the x-axis (Figure 4.1) is given by

$$\tan 2\alpha = \frac{2T_{12}}{T_{11} - T_{22}}$$

which implies

$$\alpha = \frac{1}{2} \arctan \frac{2T_{12}}{T_{11} - T_{22}} \tag{4.4}$$

Equation 4.4 defines α only locally and within an integral multiple of $\frac{\pi}{2}$. The differential of α, however, is a well-defined, smooth, differential form in the whole domain E:

$$d\alpha = \frac{(T_{11} - T_{22})dT_{12} - T_{12}d(T_{11} - T_{22})}{(T_{11} - T_{22})^2 + 4T_{12}^2} \tag{4.5}$$

From Definition 8, the index $I_{\mathbf{T}}(L)$ of a Jordan curve L is equal to the line integral

$$I_{\mathbf{T}}(L) = \frac{1}{2\pi} \oint_{L^+} d\alpha$$

where L^+ means that we traverse the curve L in a counterclockwise direction. Thus,

$$I_{\mathbf{T}}(L) = \frac{1}{2\pi} \oint_{L^+} \frac{(T_{11} - T_{22})dT_{12} - T_{12}d(T_{11} - T_{22})}{(T_{11} - T_{22})^2 + 4T_{12}^2} \tag{4.6}$$

Equation 4.6 will prove extremely useful in analyzing degenerate points (Section 4.3). First, we derive important properties of the tensor index and we show how they lead to the definition of tensor indices at degenerate points (Section 4.2.2).

Theorem 3 *Suppose that $\mathbf{T} \in C^1(E)$ where E is an open subset of $\mathbf{R}^2$ containing a Jordan curve L. Assume that there are no degenerate points of $\mathbf{T}$ on L or in its interior. It then follows that $I_{\mathbf{T}}(L) = 0$.*

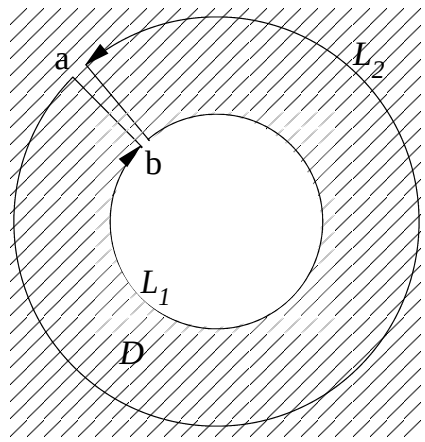

Figure 4.4: Illustration of Theorem 4.

Proof. Let S be the interior of L and let $\overline{S} = L \cup S$ be the closure of L. The assumption that there are no degenerate points in $\overline{S}$ implies that $(T_{11}-T_{22})^2+4T_{12}^2 \neq 0$ in $\overline{S}$. Since $\overline{S} \subset E$ and $\mathbf{T} \in C^1(E)$, we can apply Green's theorem (Reference [62]) to evaluate the tensor index of L. Let

$$\beta_x = \frac{1}{(T_{11}-T_{22})^2+4T_{12}^2}\{(T_{11}-T_{22})\frac{\partial T_{12}}{\partial x} - T_{12}\frac{\partial(T_{11}-T_{22})}{\partial x}\}$$

and

$$\beta_y = \frac{1}{(T_{11}-T_{22})^2+4T_{12}^2}\{(T_{11}-T_{22})\frac{\partial T_{12}}{\partial y} - T_{12}\frac{\partial(T_{11}-T_{22})}{\partial y}\}$$

The line integral in Equation 4.6 becomes

$$I_{\mathbf{T}}(L) = \frac{1}{2\pi}\oint_{L^+} \beta_x dx + \beta_y dy = \frac{1}{2\pi}\int\int_S (\frac{\partial \beta_y}{\partial x} - \frac{\partial \beta_x}{\partial y})dxdy = \frac{1}{2\pi}\int\int_S 0 dxdy = 0$$

This completes the proof. □

Theorem 4 *Suppose that* $\mathbf{T} \in C^1(E)$*, where* E *is an open subset of* $\mathbf{R}^2$*, and that* L_1 *and* L_2 *are Jordan curves contained in* E *with interiors* S_1 *and* S_2 *respectively. If* $L_1 \subset S_2$*, and if there are no degenerate points of* $\mathbf{T}$ *on* L_1*,* L_2*, and in the domain* D *between the two curves, then* $I_{\mathbf{T}}(L_1) = I_{\mathbf{T}}(L_2)$*.*

Proof. Figure 4.4 shows the configuration of the two curves. Suppose that we incise the domain D along a segment ab from L_1 to L_2. (The two line segments joining a

to b in Figure 4.4 lie infinitesimally close to each other.) Consider the Jordan curve $J = L_2^+ + ab + L_1^- + ba$. Applying Theorem 3 to the curve J and its interior,

$$\begin{aligned} 0 = I_{\mathbf{T}}(J) &= \frac{1}{2\pi}\oint_{J^+} d\alpha \\ &= \frac{1}{2\pi}\int_{L_2^+} d\alpha + \frac{1}{2\pi}\int_{ab} d\alpha + \frac{1}{2\pi}\int_{L_1^-} d\alpha + \frac{1}{2\pi}\int_{ba} d\alpha \\ &= I_{\mathbf{T}}(L_2) - I_{\mathbf{T}}(L_1) \end{aligned}$$

This completes the proof. □

4.2.2 Tensor Index at a Degenerate Point

Using Theorems 3 and 4, we associate unequivocally tensor indices to degenerate points by enclosing them with Jordan curves:

Definition 9 (Tensor Index at a Degenerate Point) *Suppose that* $\mathbf{T} \in C^1(E)$ *where* E *is an open subset of* $\mathbf{R}^2$. *Let* $\vec{x}_0 \in E$ *be an isolated degenerate point of* $\mathbf{T}$ *and let* $L \subset E$ *be a Jordan curve encompassing* $\vec{x}_0$ *in its interior and no other degenerate points of* $\mathbf{T}$. *Then the index of* $\mathbf{T}$ *at the degenerate point* $\vec{x}_0$ *is defined as*

$$I_{\mathbf{T}}(\vec{x}_0) = I_{\mathbf{T}}(L)$$

Theorem 4 implies that we can choose any Jordan curve L encompassing $\vec{x}_0$ and no other degenerate points to evaluate the tensor index at $\vec{x}_0$; we obtain the same value independently of a particular choice of L. It is a remarkable fact that the line integral in Equation 4.6 depends only on the nature of the enclosed degenerate point and not on the specific integration path. This very fact grants us considerable freedom in choosing the most appropriate path for computing the index at a degenerate point.

The following corollary results from Definition 9:

Corollary 1 *The tensor index at a degenerate point of a tensor field* $\mathbf{T} \in C^1(E)$, *where* E *is an open subset of* $\mathbf{R}^2$, *is an integer or half-integer quantity.*

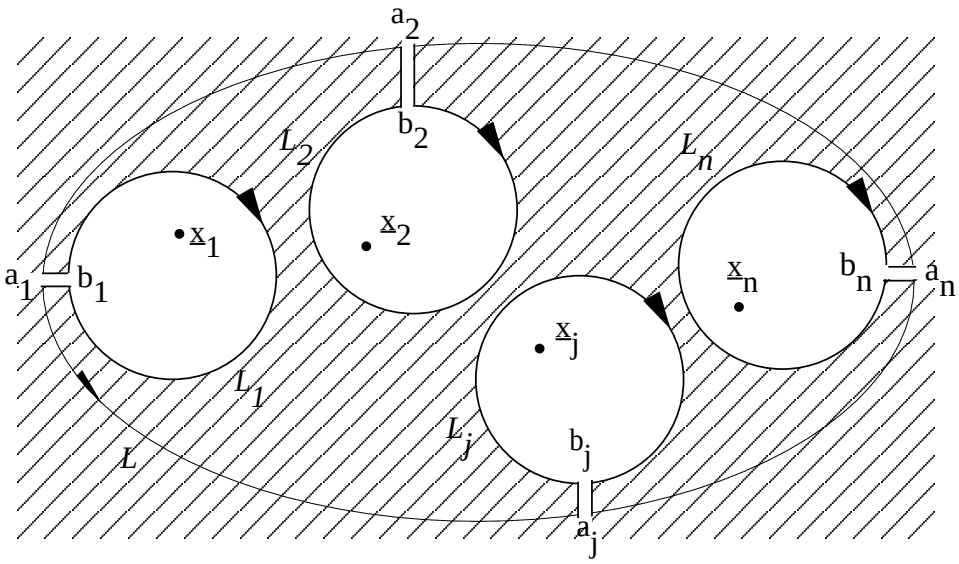

Figure 4.5: Illustration of Theorem 5.

Proof. The index at a degenerate point is equal to the index of an enclosing Jordan curve $L \subset E$. A Jordan curve is by definition piecewise-smooth and continuous, and since $\mathbf{T} \in C^1(E)$, the differential form $d\alpha$ (Equation 4.5) is smooth and continuous along L; there are no angular discontinuities in the position of the eigenvectors along L. It follows that, after one turn along L, the eigenvectors must end up parallel or anti-parallel (sign indeterminacy) to their initial position. Thus, the index is an integer or a half-integer quantity.

This completes the proof. □

The following generalizes Theorem 3 to the case of Jordan curves that encompasses several isolated degenerate points.

Theorem 5 *Suppose that* $\mathbf{T} \in C^1(E)$*, where* E *is an open subset of* $\mathbf{R}^2$ *containing a Jordan curve* L*. Assume that there are no degenerate points on* L *but that there are a finite number of degenerate points,* $\vec{x}_1, \ldots, \vec{x}_n$*, in the interior of* L*. It then follows that*

$$I_{\mathbf{T}}(L) = \sum_{j=1}^{n} I_{\mathbf{T}}(\vec{x}_j) \tag{4.7}$$

Proof. We enclose each degenerate point $\vec{x}_j$ by a circle L_j lying entirely in the interior of L and encompassing no other degenerate point than $\vec{x}_j$ (Figure 4.5). Then we proceed as in Theorem 4 to show that

$$\begin{aligned} 0 &= \frac{1}{2\pi}\int_{L^+} d\alpha + \sum_{j=1}^{n}\{\frac{1}{2\pi}\int_{a_j b_j} d\alpha + \frac{1}{2\pi}\int_{L_j^-} d\alpha + \frac{1}{2\pi}\int_{b_j a_j} d\alpha\} \\ &= I_{\mathbf{T}}(L) - \sum_{j=1}^{n} I_{\mathbf{T}}(\vec{x}_j) \end{aligned}$$

This completes the proof. □

Finally, we consider hyperstreamline cycles—i.e., closed hyperstreamline trajectories that do not pass through any degenerate points. (More to be said on limit cycles in Section 4.3.5.)

Theorem 6 *Suppose that* $\mathbf{T} \in C^1(E)$*, where* E *is an open subset of* $\mathbf{R}^2$*. Let* $L \subset E$ *be a hyperstreamline cycle of* $\mathbf{T}$ *which does not pass through any degenerate points. It then follows that* $I_{\mathbf{T}}(L) = 1$*.*

Proof. The cycle L is closed and, because it does not pass through any degenerate points, it is also not self-intersecting. Thus, L is simple. (It is, in fact, a Jordan curve.) It follows that the normal to L rotates an angle 2π during one counterclockwise revolution. Because one eigenvector field of $\mathbf{T}$ is everywhere tangent to L while the other eigenvector field lies along the normal, we obtain

$$I_{\mathbf{T}}(L) = \frac{1}{2\pi}\oint_{L^+} d\alpha = \frac{1}{2\pi}2\pi = 1$$

This completes the proof. □

Corollary 2 *Under the assumptions of Theorem 6, a hyperstreamline cycle* L *contains at least one degenerate point in its interior. And assuming there are only a finite number of degenerate points on the interior of* L*, the sum of tensor indices at these degenerate points is equal to unity.*

4.3 Degenerate Points and Separatrices

In this section, we analyze degenerate points of 2-D symmetric tensor fields. By using the tensor-index theory developed in Section 4.2, we discuss the local patterns drawn by the hyperstreamlines in the vicinity of degenerate points. (From results such as Corollary 1 in Section 4.2, we can foresee unfamiliar topological features that do not occur in conventional, signed vector fields.)

In Section 4.3.1, we analyze various types of angular sectors that may exist near a degenerate point and we introduce the concept of a hyperstreamline "separatrix." Most importantly, we establish the link between tensor index, number of sectors, and number of separatrices of each eigenvector field. In Section 4.3.2, we define the parameter δ, an invariant of third-order tensor fields that characterizes degenerate points. In Section 4.3.3, we analyze simple degenerate points ($\delta \neq 0$), and in Section 4.3.4, we discuss the more complex case of multiple degenerate points ($\delta = 0$). Finally, we study in Section 4.3.5 limit cycles of tensor fields.

4.3.1 Sectors and Separatrices

Consider an isolated degenerate point $\vec{x}_0$ of a tensor field $\mathbf{T}(\vec{x})$. In most cases, the eigenvector fields in the vicinity of $\vec{x}_0$ can be described in terms of three types of angular sectors (Figure 4.6):

- hyperbolic sectors α_i, where trajectories sweep past the degenerate point;
- parabolic sectors β_j, where trajectories lead away or towards the degenerate point; and
- elliptic sectors γ_k, where trajectories begin and end at the degenerate point.

We denote the number of hyperbolic, parabolic, and elliptic sectors by n_h, n_p, and n_e, respectively. For example, the degenerate point in Figure 4.6 has $n_h = 3$ hyperbolic, $n_p = 3$ parabolic, and $n_e = 2$ elliptic sectors. When moving along a closed curve that encompasses a degenerate point, we pass through sectors of different types within which the eigenvectors rotate in different directions. Table 4.1 shows the direction

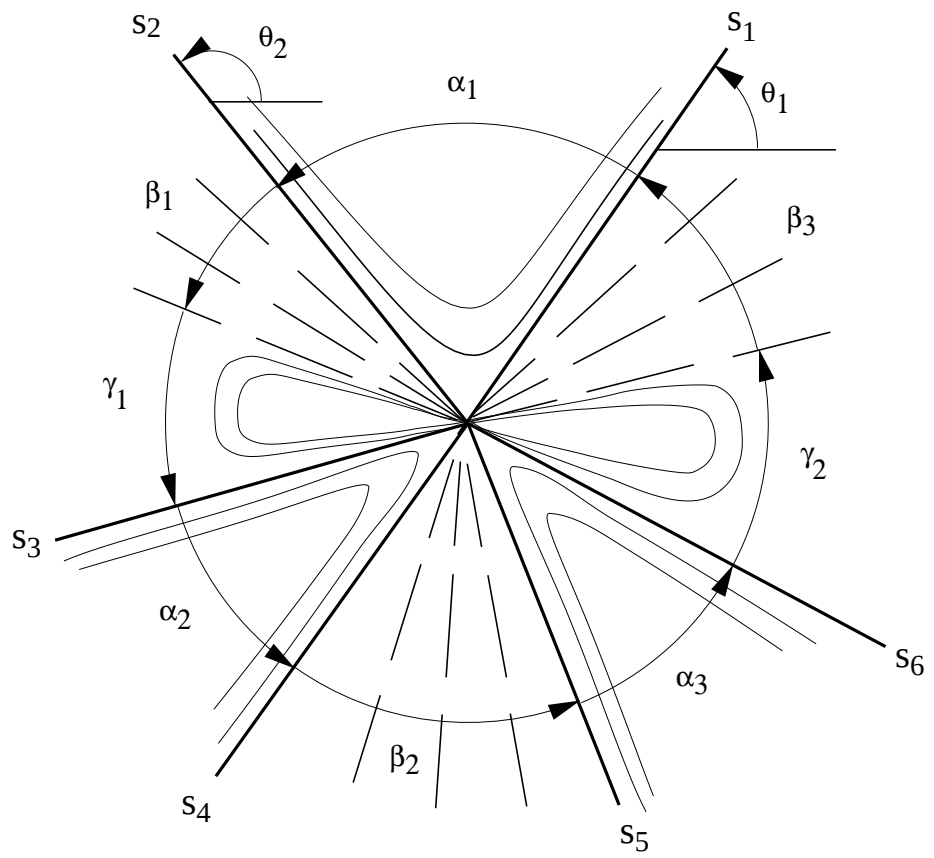

Figure 4.6: Hyperbolic (α_i), parabolic (β_j), and elliptic (γ_k) sectors at a degenerate point.

Sector	Eigenvector Rotation
parabolic	counterclockwise
elliptic	counterclockwise
hyperbolic:	
$\alpha_i > 180°$	counterclockwise
$\alpha_i < 180°$	clockwise

Table 4.1: Rotation of the eigenvectors during a counterclockwise motion around a degenerate point.

in which eigenvectors rotate during a counterclockwise motion around a degenerate point.

Most degenerate points are built from a series of adjacent hyperbolic, parabolic, and elliptic sectors. However, some degenerate points, such as "trisector points" (Section 4.3.3), have only hyperbolic sectors; others, such as "star-nodes" (Section 4.3.4), have only one parabolic sector. Furthermore, some specific points, namely centers and foci (Section 4.3.4), have neither types of sectors. But their most relevant characteristic is this very absence of hyperbolic, parabolic, and elliptic sectors. In other words, we can discuss centers and foci together with any other degenerate points simply by considering that they are made up of $n_h = 0$ hyperbolic, $n_p = 0$ parabolic, and $n_e = 0$ elliptic sectors.

Hyperstreamline trajectories that separate adjacent sectors at a degenerate point play an important topological role. In the following, we define hyperstreamline "separatrices" by analogy with the similar concept from vector field topology (References [68, 69]).

Definition 10 (Separatrices) *A separatrix of a tensor field* $\mathbf{T}$ *is a hyperstreamline trajectory which lies on the boundary of a hyperbolic sector at a degenerate point of* $\mathbf{T}$.[3]

[3]Limit cycles are also to be considered as separatrices, although of another kind, since they do not emanate from degenerate points. We consider limit cycles in Section 4.3.5.

Symbol	Description	Nature
n_h	# hyperbolic sectors	integer
n_p	# parabolic sectors	integer
n_e	# elliptic sectors	integer
n_s	# separatrices	integer
$I_{\mathbf{T}}$	tensor index	integer or half-integer

Table 4.2: Parameters describing the geometry of degenerate points.

Examples of separatrices include s_1 to s_6 in Figure 4.6. Separatrices lie on hyperbolic/hyperbolic, hyperbolic/parabolic, and hyperbolic/elliptic boundaries, but trajectories along parabolic/parabolic, parabolic/elliptic, and elliptic/elliptic boundaries are not to be considered as separatrices. Also, we always merge adjacent parabolic sectors into a unique parabolic sector.

In what follows, we denote by n_s the number of separatrices at a degenerate point. We summarize various parameters characterizing degenerate points in Table 4.2. $I_{\mathbf{T}}$, the tensor index, characteristizes the tensor field as a whole; it is the same for both eigenvector fields. Conversely, n_h, n_p, n_e, and n_s usually differ from one eigenvector field to the other; they must be specified for each eigenvector field separately.

The two following theorems establish relations that exist among the various quantities listed in Table 4.2.

Theorem 7 *Consider an eigenvector field in the vicinity of a degenerate point. Let n_h and n_s be the number of hyperbolic sectors and separatrices, respectively. Then*

$$n_h \leq n_s \leq 2n_h \tag{4.8}$$

Proof. The number of separatrices, n_s, is equal to the total number of hyperbolic/hyperbolic, hyperbolic/parabolic, and hyperbolic/elliptic interfaces among sectors (Figure 4.6). Equation 4.8 results from the fact that isolated hyperbolic sectors generate two separatrices each, but that a boundary that separates adjacent hyperbolic sectors must not be counted twice.

This completes the proof. □

Next, we extend to the degenerate points of tensor fields a famous theorem that was proven by I. Bendixson for the critical points of vector fields (References [68, 70]):

Theorem 8 (Bendixson) *Let $\vec{x}_0$ be an isolated degenerate point of a tensor field* $\mathbf{T}$. *The tensor index at $\vec{x}_0$ is given by*

$$I_{\mathbf{T}}(\vec{x}_0) = 1 + \frac{n_e - n_h}{2} \tag{4.9}$$

where n_e and n_h are the number of elliptic and hyperbolic sectors at $\vec{x}_0$.

Proof. Consider as in Figure 4.6 a hypothetical degenerate point with n_h hyperbolic, n_p parabolic, and n_e elliptic sectors ($n_h = n_p = n_e = 0$ for a center or a focus). Assume that hyperbolic sectors span angles α_i ($i = 1, \ldots, n_h$), that parabolic sectors span angles β_j ($j = 1, \ldots, n_p$), and that elliptic sectors span angles γ_k ($k = 1, \ldots, n_e$). The eigenvectors rotate over an angle $\alpha_i - \pi$ within a hyperbolic sector, β_j within a parabolic sector, and $\gamma_k + \pi$ within an elliptic sector (Figure 4.6). Thus, during one counterclockwise revolution around the degenerate point, the eigenvectors rotate over an angle

$$2\pi I_{\mathbf{T}}(\vec{x}_0) = \sum_{i=1}^{n_h}(\alpha_i - \pi) + \sum_{j=1}^{n_p}\beta_j + \sum_{i=1}^{n_e}(\gamma_k + \pi)$$

Since

$$\sum_{i=1}^{n_h}\alpha_i + \sum_{j=1}^{n_p}\beta_j + \sum_{i=1}^{n_e}\gamma_k = 2\pi$$

the index at the degenerate point is given by

$$I_{\mathbf{T}}(\vec{x}_0) = 1 + \frac{n_e - n_h}{2}$$

This completes the proof. □

This theorem establishes a relation between the tensor index at a degenerate point and the number of elliptic and hyperbolic sectors. It is worth noting that parabolic sectors do not affect the index at a degenerate point.

Corollary 3 *The two eigenvector fields at an isolated degenerate point can have different numbers of hyperbolic, elliptic, and parabolic sectors. The difference $n_e - n_h$ between the number of elliptic and hyperbolic sectors, however, is the same for both eigenvectors.*

Proof. Theorem 8 implies a one-to-one correspondence between the index at a degenerate point and $n_e - n_h$. Since the index characterizes the tensor field—not the eigenvector fields separately (see for example Equation 4.6)—$n_e - n_h$ is identical for both eigenvector fields.

This completes the proof. □

In Sections 4.3.3 and 4.3.4, we thoroughly analyze sectors, separatrices, and tensor index at degenerate points. First, we discuss δ, an invariant that allows us to distinguish between simple and multiple degenerate points.

4.3.2 The Invariant δ

In vector fields, there are various types of critical points—such as nodes, foci, centers, and saddle points—that correspond to different local patterns of the neighboring streamlines. These patterns are characterized by the vector gradients at critical point positions (Section 2.2.1). Likewise in tensor fields, different types of degenerate points can occur that correspond to different local patterns of the neighboring hyperstreamlines. These patterns are determined by the tensor gradients at degenerate point positions.

Let $\vec{x}_0 = (x_0, y_0)$ be an isolated degenerate point. Assuming that the functions $T_{11}(\vec{x}) - T_{22}(\vec{x})$ and $T_{12}(\vec{x})$ are analytic, we can expand tensor components in Taylor series around $\vec{x}_0$ as

$$\begin{aligned} \frac{T_{11} - T_{22}}{2} &= \sum_{k \geq 0}^{\infty} P_{m_p+k}(x - x_0, y - y_0) \\ T_{12} &= \sum_{k \geq 0}^{\infty} Q_{m_q+k}(x - x_0, y - y_0) \end{aligned} \tag{4.10}$$

where $P_m(x, y)$ and $Q_m(x, y)$ are homogeneous polynomials of degree m. The first non-vanishing terms in Equations 4.10 are of degree $m_p \geq 1$ and $m_q \geq 1$, respectively. The polynomials $P_m(x, y)$ and $Q_m(x, y)$ are given by

$$\begin{aligned} P_m(x, y) &= \sum_{i=0}^{m} p_i^{(m)} x^{m-i} y^i \\ Q_m(x, y) &= \sum_{i=0}^{m} q_i^{(m)} x^{m-i} y^i \end{aligned}$$

and the coefficients $p_i^{(m)}$ and $q_i^{(m)}$, $i = 0, \ldots, m$, are equal to the partial derivatives

$$\begin{aligned} p_i^{(m)} &= \frac{1}{m!}\begin{pmatrix} m \\ i \end{pmatrix} \frac{1}{2} \frac{\partial (T_{11} - T_{22})^m}{\partial x^{m-i} \partial y^i}\bigg|_{\vec{x}_0} \\ q_i^{(m)} &= \frac{1}{m!}\begin{pmatrix} m \\ i \end{pmatrix} \frac{\partial {T_{12}}^m}{\partial x^{m-i} \partial y^i}\bigg|_{\vec{x}_0} \end{aligned}$$

evaluated at the position of the degenerate point $\vec{x}_0$.

When it is possible to retain only the first-order terms in Equations 4.10 ($m_p = m_q = 1$), we use the simplified notation

$$\begin{aligned} a \equiv p_0^{(1)} &= \tfrac{1}{2}\tfrac{\partial (T_{11}-T_{22})}{\partial x}\Big|_{\vec{x}_0} & b \equiv p_1^{(1)} &= \tfrac{1}{2}\tfrac{\partial (T_{11}-T_{22})}{\partial y}\Big|_{\vec{x}_0} \\ c \equiv q_0^{(1)} &= \tfrac{\partial T_{12}}{\partial x}\Big|_{\vec{x}_0} & d \equiv q_1^{(1)} &= \tfrac{\partial T_{12}}{\partial y}\Big|_{\vec{x}_0} \end{aligned} \tag{4.11}$$

In this case, Equations 4.10 simply reduce to

$$\begin{aligned} \tfrac{T_{11}-T_{22}}{2} &\approx a(x - x_0) + b(y - y_0) + \cdots \\ T_{12} &\approx c(x - x_0) + d(y - y_0) + \cdots \end{aligned} \tag{4.12}$$

where "$\cdots$" stands for terms of degree higher than one.

An important quantity for characterizing degenerate points is

$$\delta = ad - bc \tag{4.13}$$

The appeal of δ arises from its being invariant under rotation; when rotating the coordinate system, tensor components T_{ij} and a fortiori, partial derivatives $\{a, b, c, d\}$ change, but δ remains constant. In order to show the invariance of δ, we need the following lemma which establishes an invariant of third-order tensor fields:

Lemma 1 *Let α_{ijk} $(1 \leq i, j, k \leq 2)$ be the components of a third-order tensor field. Then, the quantity*

$$\Delta = \sum_{i=1}^{2} \begin{vmatrix} \alpha_{i11} & \alpha_{i12} \\ \alpha_{i21} & \alpha_{i22} \end{vmatrix} \tag{4.14}$$

is invariant under rotation of the coordinate system.

Proof. Cartesian components α_{ijk} of third-order tensor fields transform according to

$$\alpha'_{ijk} = \sum_{p,q,r=1}^{2} \beta_{ip}\beta_{jq}\beta_{kr}\alpha_{pqr}$$

under the orthonormal transformation

$$\beta = \begin{pmatrix} \cos\varphi & \sin\varphi \\ -\sin\varphi & \cos\varphi \end{pmatrix}$$

of the coordinate axes. The explicit transformation formulas are

$$\begin{aligned}
\alpha'_{111} &= \alpha_{111}\cos^3\varphi + (\alpha_{211}+\alpha_{121}+\alpha_{112})\cos^2\varphi\sin\varphi \\
&+ (\alpha_{122}+\alpha_{212}+\alpha_{221})\cos\varphi\sin^2\varphi + \alpha_{222}\sin^3\varphi \\
\alpha'_{112} &= \alpha_{112}\cos^3\varphi + (\alpha_{212}+\alpha_{122}-\alpha_{111})\cos^2\varphi\sin\varphi \\
&+ (\alpha_{121}+\alpha_{211}-\alpha_{222})\cos\varphi\sin^2\varphi - \alpha_{221}\sin^3\varphi \\
\alpha'_{121} &= \alpha_{121}\cos^3\varphi + (\alpha_{221}-\alpha_{111}+\alpha_{122})\cos^2\varphi\sin\varphi \\
&+ (\alpha_{112}-\alpha_{222}+\alpha_{211})\cos\varphi\sin^2\varphi - \alpha_{212}\sin^3\varphi \\
\alpha'_{122} &= \alpha_{122}\cos^3\varphi + (\alpha_{222}-\alpha_{112}-\alpha_{121})\cos^2\varphi\sin\varphi \\
&+ (\alpha_{111}-\alpha_{212}-\alpha_{221})\cos\varphi\sin^2\varphi + \alpha_{211}\sin^3\varphi \\
\alpha'_{211} &= \alpha_{211}\cos^3\varphi - (\alpha_{111}-\alpha_{221}-\alpha_{212})\cos^2\varphi\sin\varphi \\
&- (\alpha_{222}-\alpha_{112}-\alpha_{121})\cos\varphi\sin^2\varphi - \alpha_{122}\sin^3\varphi \\
\alpha'_{212} &= \alpha_{212}\cos^3\varphi - (\alpha_{112}-\alpha_{222}+\alpha_{211})\cos^2\varphi\sin\varphi \\
&- (\alpha_{221}-\alpha_{111}+\alpha_{122})\cos\varphi\sin^2\varphi + \alpha_{121}\sin^3\varphi \\
\alpha'_{221} &= \alpha_{221}\cos^3\varphi - (\alpha_{121}+\alpha_{211}-\alpha_{222})\cos^2\varphi\sin\varphi \\
&- (\alpha_{212}+\alpha_{122}-\alpha_{111})\cos\varphi\sin^2\varphi + \alpha_{112}\sin^3\varphi \\
\alpha'_{222} &= \alpha_{222}\cos^3\varphi - (\alpha_{122}+\alpha_{212}+\alpha_{221})\cos^2\varphi\sin\varphi \\
&- (-\alpha_{211}-\alpha_{121}-\alpha_{112})\cos\varphi\sin^2\varphi - \alpha_{111}\sin^3\varphi
\end{aligned}$$

Let Δ and Δ' be defined as

$$\Delta = \begin{vmatrix} \alpha_{111} & \alpha_{112} \\ \alpha_{121} & \alpha_{122} \end{vmatrix} + \begin{vmatrix} \alpha_{211} & \alpha_{212} \\ \alpha_{221} & \alpha_{222} \end{vmatrix}$$

and

$$\Delta' = \begin{vmatrix} \alpha'_{111} & \alpha'_{112} \\ \alpha'_{121} & \alpha'_{122} \end{vmatrix} + \begin{vmatrix} \alpha'_{211} & \alpha'_{212} \\ \alpha'_{221} & \alpha'_{222} \end{vmatrix}$$

respectively. Using the transformation formulas for the components α_{ijk}, and after a lengthy calculation, one can demonstrate that

$$\begin{aligned} \Delta' &= \Delta(\cos^6\alpha + \cos^4\alpha\sin^2\alpha + \cos^2\alpha\sin^4\alpha + \sin^6\alpha) \\ &= \Delta(\cos^2\alpha + \sin^2\alpha)^3 \\ &= \Delta \end{aligned}$$

Thus, Δ is a third-order tensor invariant.

This completes the proof. □

Invariants of second-order tensor fields—such as eigenvalues, trace, or determinant—are familiar quantities, but these concepts are without equivalents for third-order tensor fields. (It is difficult to conceptualize, for example, eigenvalues of third-order tensor fields.) However, Lemma 1 establishes that Δ is a third-order invariant. Although both determinants in Equation 4.14 vary under rotation, their sum remains invariably constant.

The invariance of $\delta = ad - bc$ is closely related to Lemma 1, as discussed below.

Theorem 9 *The parameter δ defined by Equation 4.13 is invariant under rotation of the coordinate system.*

Proof. Partial derivatives $\alpha_{ijk} = \frac{\partial T_{ij}}{\partial x_k}$ of components T_{ij} of second-order tensor fields are, themselves, components of third-order tensor fields. It follows from Lemma 1 that

$$\Delta = \begin{vmatrix} \frac{\partial T_{11}}{\partial x} & \frac{\partial T_{11}}{\partial y} \\ \frac{\partial T_{12}}{\partial x} & \frac{\partial T_{12}}{\partial y} \end{vmatrix} + \begin{vmatrix} \frac{\partial T_{21}}{\partial x} & \frac{\partial T_{21}}{\partial y} \\ \frac{\partial T_{22}}{\partial x} & \frac{\partial T_{22}}{\partial y} \end{vmatrix}$$

is a third-order invariant. In the case of symmetric tensor fields, $T_{12} = T_{21}$, and

$$\begin{aligned} \Delta &= \frac{\partial(T_{11} - T_{22})}{\partial x}\frac{\partial T_{12}}{\partial y} - \frac{\partial(T_{11} - T_{22})}{\partial y}\frac{\partial T_{12}}{\partial x} \\ &= 2(ad - bc) \\ &= 2\delta \end{aligned}$$

Thus, δ is invariant under rotation of the coordinate axes.

This completes the proof. □

The invariant δ at a degenerate point allows us to distinguish simple from multiple degenerate points. We define these two classes of degenerate points below.

Definition 11 (Simple and Multiple Degenerate Points) *Let $\vec{x}_0$ be an isolated degenerate point of a tensor field $\mathbf{T} \in C^1(E)$, where E is an open subset of $\mathbf{R}^2$, and let $\delta = ad - bc$ be the corresponding third-order invariant. Then, $\vec{x}_0$ is*

- *a simple degenerate point iff $\delta \neq 0$, or*
- *a multiple degenerate point iff $\delta = 0$.*

In Section 4.3.3, we discuss in detail simple degenerate points. Since $\delta \neq 0$ in this case, we can limit Taylor expansions of tensor components to first-order terms, and use Equations 4.12 as a starting point for the analysis. Then, we discuss the more complex multiple degenerate points in Section 4.3.4. In this case, the analysis is complicated by the necessity of keeping higher-order terms in Equations 4.10.[4]

4.3.3 Simple Degenerate Points

From now on we assume that the functions $T_{11} - T_{22}$ and T_{12} are analytic in an open neighborhood of the degenerate point under study. That is, we assume that both functions have converging Taylor expansions at each point of the neighborhood. Following Definition 11, simple degenerate points are characterized by $\delta = ad - bc \neq 0$ and tensor components can be expressed as Taylor expansions limited to first-order terms (Equation 4.12). Hence the following theorem:

[4] If $\delta = 0$, the gradients of $T_{11} - T_{22}$ and T_{12} are colinear. To first-order approximation, the tensor components do not vary in the direction perpendicular to the gradients, and a multiple degenerate point appears as a "row" of adjacent simple degenerate points. Thus, we need higher-order terms to accurately depict multiple degenerate points.

Theorem 10 *Let* $\mathbf{T}$ *be an analytic tensor field in an open subset* E *of* $\mathbf{R}^2$ *and let* $\vec{x}_0 \in E$ *be a simple degenerate point of* $\mathbf{T}$. *Let* $\delta = ad - bc \neq 0$ *be the third-order invariant computed at* $\vec{x}_0$. *Then,*

$$I_{\mathbf{T}}(\vec{x}_0) = \frac{1}{2} sign(\delta) = \pm\frac{1}{2} \tag{4.15}$$

Proof. Let $\vec{x}_0 \equiv (x_0, y_0)$. To compute $I_{\mathbf{T}}(\vec{x}_0)$, we evaluate the line integral in Equation 4.6 along a Jordan curve L encompassing $\vec{x}_0$ and no other degenerate points. L is chosen to be small enough so that tensor components can be approximated along L by their first-order terms (Equations 4.12). Let $u \equiv x - x_0$ and $v \equiv y - y_0$. Equation 4.6 leads to

$$I_{\mathbf{T}}(\vec{x}_0) = \frac{1}{4\pi} \oint_{L+} \frac{(au + bv)d(cu + dv) - (cu + dv)d(au + bv)}{(au + bv)^2 + (cu + dv)^2}$$

Theorem 4 grants considerable freedom in choosing the most appropriate curve L. For example, consider the ellipse L_0 satisfying the equation

$$(au + bv)^2 + (cu + dv)^2 = 1$$

The expression for the tensor index at $\vec{x}_0$ becomes

$$I_{\mathbf{T}}(\vec{x}_0) = \frac{1}{4\pi} \oint_{L_0^+} (au + bv)d(cu + dv) - (cu + dv)d(au + bv)$$

Adopting new variables $P \equiv au + bv$ and $Q \equiv cu + dv$, replaces integrating along the ellipse L_0 in uv-plane by integrating along a circle $C_0 : P^2 + Q^2 = 1$ in PQ-plane. The motion along L_0 must be counterclockwise, which corresponds to either a counterclockwise or a clockwise motion along C_0, depending on whether the determinant of the Jacobian

$$\begin{vmatrix} \frac{\partial P}{\partial u} & \frac{\partial P}{\partial v} \\ \frac{\partial Q}{\partial u} & \frac{\partial Q}{\partial v} \end{vmatrix} = \begin{vmatrix} a & b \\ c & d \end{vmatrix} = \delta$$

is positive or negative. It follows that

$$I_{\mathbf{T}}(\vec{x}_0) = \frac{sign(\delta)}{4\pi} \oint_{C_0^+} PdQ - QdP$$

Letting $P \equiv \cos\varphi$ and $Q \equiv \sin\varphi$,

$$I_{\mathbf{T}}(\vec{x}_0) = \frac{sign(\delta)}{4\pi}\int_0^{2\pi} \cos\varphi d\sin\varphi - \sin\varphi d\cos\varphi = \frac{sign(\delta)}{4\pi}\int_0^{2\pi} d\varphi = \frac{1}{2}sign(\delta)$$

This completes the proof. □

Corollary 4 *When moving along a closed curve encompassing a simple degenerate point, eigenvectors rotate in a constant direction, clockwise or counterclockwise.*

Proof. Let α be the angle between the eigenvectors and the x-axis. From the proof of Theorem 10,

$$\frac{d\alpha}{d\varphi} = \frac{1}{2}sign(\delta)$$

where φ is the polar angle running along the circle C_0 in PQ-plane. $\frac{d\alpha}{d\varphi}$ may be positive or negative but the important fact is that $\frac{d\alpha}{d\varphi}$ keeps a constant sign for φ ranging from 0 to 2π; when moving along a closed curve encompassing a simple degenerate point, eigenvectors rotate in a constant direction—clockwise or counterclockwise.

This completes the proof. □

Corollary 5 *Each eigenvector field at a simple degenerate point has one or three hyperbolic sectors, and no elliptic sectors. That is,*

$$\begin{cases} n_e = 0 \\ n_h = 2 - sign(\delta) \end{cases} \tag{4.16}$$

at simple degenerate points.

Proof. Theorems 8 and 10 imply that simple degenerate points are characterized by

$$n_h = n_e + 2 - sign(\delta) \tag{4.17}$$

Assume that there is at least one elliptic sector ($n_e \geq 1$). Equation 4.17 implies that there must be $n_h \geq 2$ ($\delta > 0$) or $n_h \geq 4$ ($\delta < 0$) hyperbolic sectors. From Corollary 4, the eigenvectors must rotate in the same direction within both elliptic and hyperbolic

sectors. Table 4.1 then shows that the hyperbolic sectors must be wider than 180°. This is clearly impossible as the angles spanned by elliptic and hyperbolic sectors must add up to less than 360°.

So $n_e = 0$ and $n_h = 2 - sign(\delta)$.

This completes the proof. □

It follows that simple degenerate points with $\delta < 0$ have $n_h = 3$, $n_e = 0$, and $I_{\mathbf{T}}(\vec{x}_0) = -\frac{1}{2}$. Likewise, simple degenerate points with $\delta > 0$ have $n_h = 1$, $n_e = 0$, and $I_{\mathbf{T}}(\vec{x}_0) = \frac{1}{2}$. The following theorem develops these results further.

Theorem 11 *Let* $\mathbf{T}$ *be an analytic tensor field in an open subset* E *of* $\mathbf{R}^2$*, and let* $\vec{x}_0 \in E$ *be an isolated, simple degenerate point of* $\mathbf{T}$*. The invariant* $\delta = ad - bc \neq 0$ *at* $\vec{x}_0$ *determines two classes of simple degenerate points which are shown schematically in Figure 4.7. To* $\delta < 0$ *correspond trisector points* ($I_{\mathbf{T}}(\vec{x}_0) = -\frac{1}{2}$) *and to* $\delta > 0$ *correspond wedge points* ($I_{\mathbf{T}}(\vec{x}_0) = \frac{1}{2}$)*. Neither types of points have elliptic sectors. For each eigenvector field, trisector points have three hyperbolic sectors, no parabolic sectors, and three separatrices—*s_1, s_2*, and* s_3*. Wedge points have either one hyperbolic sector, one parabolic sector, and two separatrices (*s_1 *and* s_2*); or one hyperbolic sector, no parabolic sector, and one separatrix (*$s_1 = s_2$*). The angles* θ_k *between the x-axis and the separatrices* s_k *are obtained by computing the real roots* z_k *(including infinity) of the cubic equation*

$$dz^3 + (c + 2b)z^2 + (2a - d)z - c = 0, \tag{4.18}$$

by inverting the relation $z_k = \tan\theta_k$*, and by keeping only those angles that lie along the boundary of a hyperbolic sector.*

Remark. Figure 4.8 shows textures representing the two eigenvector fields, $\vec{v}_1$ and $\vec{v}_2$, in the vicinity of a trisector and a wedge point. Color encodes the difference between the two eigenvalues. Figure 4.8 emphasizes that the two eigenvector fields have the same number of separatrices and that the separatrices of $\vec{v}_2$ are images of the separatrices of $\vec{v}_1$ under a rotation of $\pm\pi$ (see proof below). These properties

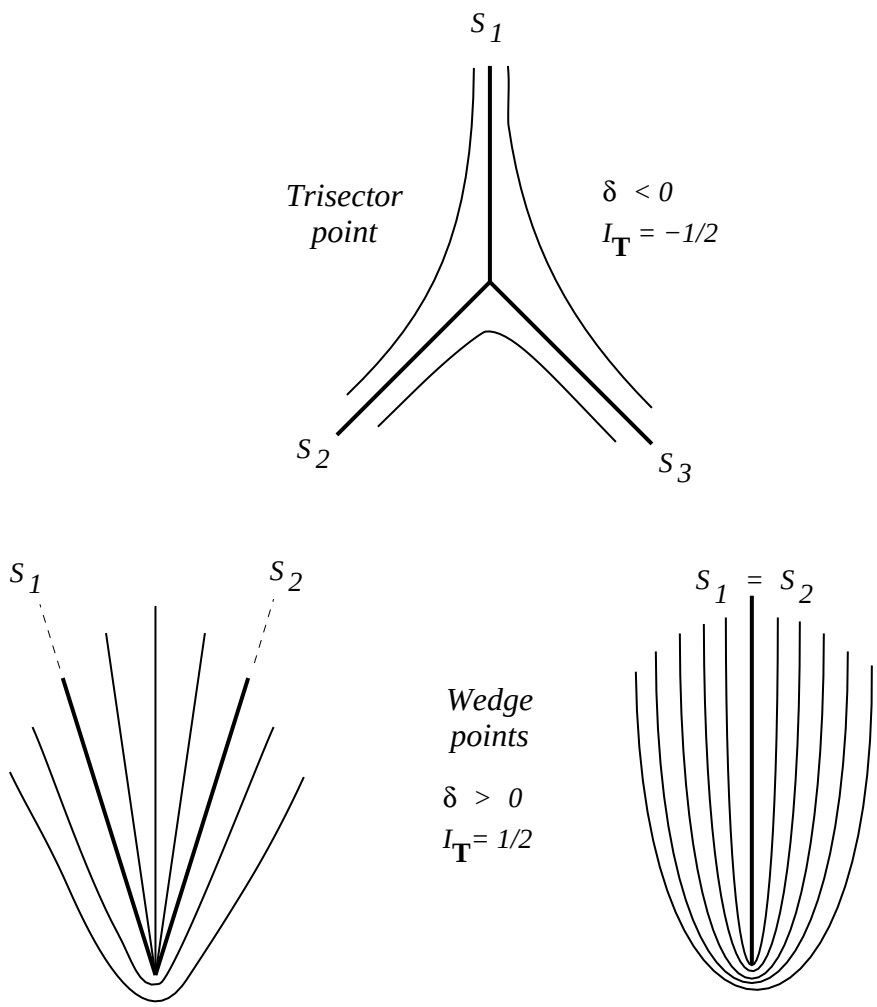

Figure 4.7: Simple degenerate points. $\delta = ad - bc \neq 0$ and $I_{\mathbf{T}}$ = tensor index. Trisector ($\delta < 0$) and wedge ($\delta > 0$) points. Trajectories s_k are separatrices.

Figure 4.8: Textures representing the two eigenvector fields in the vicinity of a trisector point (top) and a wedge point (bottom). Color encodes the difference between the two eigenvalues.

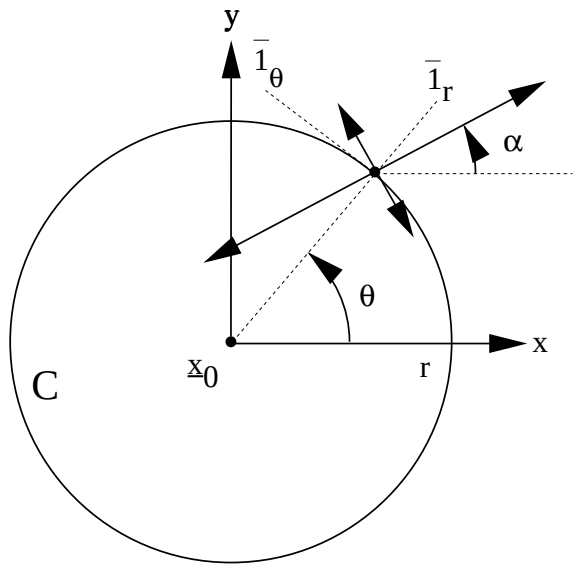

Figure 4.9: Illustration of Theorem 11.

are specific to simple degenerate points and do not, in general, apply to multiple degenerate points.

Proof. Consider a circle C with radius r and center $\vec{x}_0$ (Figure 4.9). Let S be the interior of C. The radius r is chosen to be small enough so that no degenerate points except $\vec{x}_0$ lie in $C \cup S$, and so that tensor components can be approximated by their first-order terms in every point of $C \cup S$ (Equation 4.12). Let θ be the polar angle between the x-axis and the radial vectors joining $\vec{x}_0$ to points on C, and let T_{ij}, $i, j = 1, 2$, be the Cartesian components of $\mathbf{T}$. Then, Equation 1.3 implies that the polar components of $\mathbf{T}$—i.e., the components of $\mathbf{T}$ in the frame $(\vec{1}_r, \vec{1}_\theta)$ (Figure 4.9)—are given by:

$$\begin{aligned}
T_{rr} &= \frac{1}{2}(T_{11} + T_{22}) + \frac{1}{2}(T_{11} - T_{22})\cos 2\theta + T_{12}\sin 2\theta \\
T_{r\theta} &= T_{\theta r} = -\frac{1}{2}(T_{11} - T_{22})\sin 2\theta + T_{12}\cos 2\theta \\
T_{\theta\theta} &= \frac{1}{2}(T_{11} + T_{22}) - \frac{1}{2}(T_{11} - T_{22})\cos 2\theta - T_{12}\sin 2\theta
\end{aligned} \tag{4.19}$$

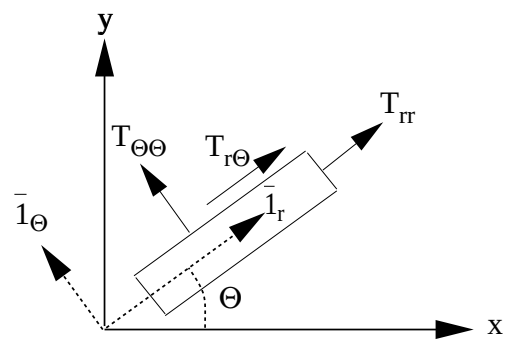

Figure 4.10: Polar components of **T**.

These polar components are shown in Figure 4.10. At the direction of the separatrices, one eigenvector of **T** lies in the radial direction.[5] This happens at angles θ where the polar components of **T** are diagonalized—i.e.,

$$T_{r\theta} = T_{\theta r} = 0 \tag{4.20}$$

which implies that

$$\tan 2\theta = \frac{2T_{12}}{T_{11} - T_{22}}$$

This equation is indeed equivalent to the condition

$$\tan 2\theta = \tan 2\alpha(\theta)$$

where $\alpha(\theta)$ is the angle between the x-axis and the eigenvectors of **T** at position θ along C (Figure 4.9). Expanding tensor components to first order, as in Equations 4.12, leads to

$$\tan 2\theta = \frac{c(x - x_0) + d(y - y_0)}{a(x - x_0) + b(y - y_0)}$$

On the circle C, $x - x_0 = r\cos\theta$ and $y - y_0 = r\sin\theta$. Thus, Equation 4.20 becomes

$$\tan 2\theta = \frac{2\tan\theta}{1 - \tan^2\theta} = \frac{c + d\tan\theta}{a + b\tan\theta}$$

or

$$dz^3 + (c + 2b)z^2 + (2a - d)z - c = 0$$

[5]Not all of these "radial" directions are separatrices because some of them might not lie on the boundary of a hyperbolic sector.

where $z \equiv \tan\theta$.

The direction of the separatrices with respect to the x-axis is, therefore, obtained by computing the real roots z_k (including infinity) of Equation 4.18, by extracting the corresponding angles

$$\theta_k = \arctan z_k \quad (-\frac{\pi}{2} \leq \theta_k \leq \frac{\pi}{2})$$

and

$$\theta'_k = \theta_k + \pi,$$

and by keeping only those directions that lie on the boundary of a hyperbolic sector (this de facto eliminates unwanted parabolic/parabolic boundaries).

Another consequence of Equation 4.19 is that

$$T_{rr}(\theta) > T_{\theta\theta}(\theta) \Leftrightarrow T_{rr}(\theta + \pi) < T_{\theta\theta}(\theta + \pi)$$

and vice versa. In particular, if $\theta = \theta_k$ is a radial direction, $T_{rr}(\theta_k)$ is equal to the eigenvalue $\lambda_r(\theta_k)$ corresponding to the radial eigenvector, and $T_{\theta\theta}(\theta_k)$ is equal to the eigenvalue $\lambda_\theta(\theta_k)$ corresponding to the eigenvector tangent to C. Thus,

$$\lambda_r(\theta_k) > \lambda_\theta(\theta_k) \Leftrightarrow \lambda_r(\theta'_k) < \lambda_\theta(\theta'_k) \tag{4.21}$$

and vice versa. It follows that, if $\vec{v}_1$ is radial at angles $\theta_1, \theta_2, \ldots$, then $\vec{v}_2$ is radial at angles $\theta'_1, \theta'_2, \ldots$ Each real root z_k of Equation 4.18 defines two angles, θ_k and θ'_k, that correspond to radial directions of different eigenvector fields.

Let n_r be the number of real roots z_k of Equation 4.18. A cubic polynomial has at most three real roots (including infinity), so

$$n_r \leq 3$$

These n_r roots define $2n_r$ angles, θ_k and θ'_k, and the former discussion implies that each eigenvector is radial at exactly n_r different angular positions along C. Since every separatrix direction is a radial direction but not every radial direction is a separatrix direction,

$$n_s \leq n_r$$

So,

$$n_s \leq 3 \tag{4.22}$$

and *each eigenvector has at most three separatrices originating from a simple degenerate point.*

If $\delta < 0$, Corollary 5 implies $n_h = 3$ and $n_e = 0$; the degenerate point has three hyperbolic sectors and no elliptic sectors. There are no parabolic sectors or else there would be at least 4 separatrices per eigenvector field, which is incompatible with Equation 4.22. The pattern of hyperstreamlines therefore corresponds to the *trisector point* shown by the texture in Figure 4.8 and represented schematically in Figure 4.7. There are three separatrices, s_1, s_2, and s_3, per eigenvector field. Separatrices are spread fairly evenly as each hyperbolic sector is less than 180° wide, a fact that results from Corollary 4 and Table 4.1.

If $\delta > 0$, Corollary 5 implies $n_h = 1$ and $n_e = 0$; the degenerate point has one hyperbolic sector and no elliptic sector. There can be $n_p = 1$ or $n_p = 0$ parabolic sectors. Assume that $n_p = 1$, so there are $n_s = 2$ separatrices per eigenvector—s_1 and s_2. The local pattern corresponds to the *wedge point* in Figures 4.7 and 4.8. Corollary 4 and Table 4.1 imply that the hyperbolic sector at a wedge point is wider than 180°. In some cases, it may happen that separatrices s_1 and s_2 collapse onto each other, cancelling the parabolic sector and widening the hyperbolic sector to 360°. Such a wedge point is represented in the bottom right corner of Figure 4.7. In this case, there is only one separatrix per eigenvector field ($n_p = 0$ and $n_s = 1$), and Equation 4.18 has one real and two complex conjugate roots.

This completes the proof. □

The characteristics of simple degenerate points are summarized in Table 4.3.

4.3.4 Multiple Degenerate Points

Wedges and trisectors are instances of simple degenerate points. They are the simplest singularities that can arise in continuous tensor fields in the sense that they cannot be broken down into more elementary singularities associated to smaller indices. But

	Trisector Points	Wedge Points		
n_h	3		1	
n_e	0		0	
n_p	0	1	or	0
n_s	3	2	or	1
$I_{\mathbf{T}}$	$-\frac{1}{2}$		$\frac{1}{2}$	
α_i	$< 180°$	$> 180°$	or	$360°$

Table 4.3: Simple degenerate points. α_i is the angle spanned by hyperbolic sectors.

there is more to the story. Definition 11 introduced yet another class of degenerate points: the multiple degenerate points that are characterized by $\delta = ad - bc = 0$.

A mathematical investigation of multiple degenerate points is complicated by the fact that higher-order terms must now be taken into account in the Taylor expansions of Equations 4.10. Fortunately, a great deal of insight into the structure of multiple degenerate points can be gleaned from a Corollary of Theorem 5.

Corollary 6 *A multiple degenerate point $\vec{x}_0$ of index $I_{\mathbf{T}}$ is equivalent in the far field to a combination of simple degenerate points whose indices add up to $I_{\mathbf{T}}$. That is, $\vec{x}_0$ is equivalent to $\mathcal{W}$ wedge points and $\mathcal{T}$ trisectors such that*

$$\mathcal{W} - \mathcal{T} = 2I_{\mathbf{T}} \tag{4.23}$$

Proof. Let L be a Jordan curve and let S be L's interior. Following Theorem 5, the tensor index of L is equal to the sum of the indices at the degenerate points in S. Assume that the only degenerate point lying in S is a multiple degenerate point of index $I_{\mathbf{T}}$. Following Corollary 1, $I_{\mathbf{T}}$ is an integer or half-integer quantity. It follows that $2I_{\mathbf{T}}$ is an integer number, and that it is always possible to find an integer number of wedges ($\mathcal{W}$) and an integer number of trisectors ($\mathcal{T}$) satisfying Equation 4.23. Thus, a tensor field with same boundary conditions on L, but with $\mathcal{W}$ wedge points and $\mathcal{T}$ trisectors as only degenerate points in S, can be substituted for $\mathbf{T}$ within S without changing the field in L's exterior.

This completes the proof. □

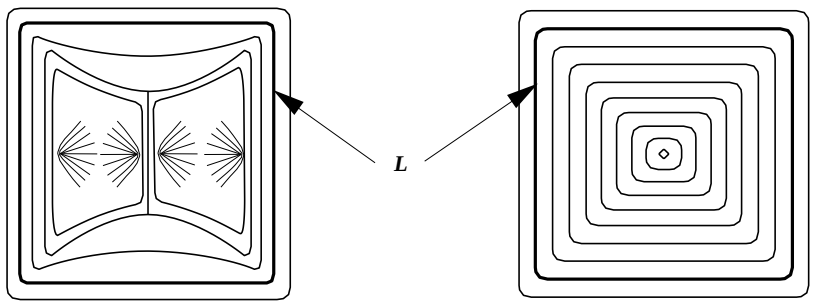

Figure 4.11: Combination of wedges and trisectors looking like a center in the far field.

In order to illustrate Corollary 6, consider the combination of simple degenerate points represented in Figure 4.11 (left). This pattern is made up of $\mathcal{W} = 4$ wedge points and $\mathcal{T} = 2$ trisectors. The total index is $I_{\mathbf{T}} = 4 \times \frac{1}{2} - 2 \times \frac{1}{2} = 1$ and the structure looks like a center ($I_{\mathbf{T}} = 1$) in the far field. As shown in Figure 4.11 (right), it is possible to substitute a center for the pattern in L's interior without changing the tensor field in L's exterior. We shall see that centers are indeed instances of multiple degenerate points.

First, we discuss the nature of those multiple degenerate points that are created by a few, merging, simple degenerate points. Then, we present a more general and more mathematical approach that extends the results of Theorem 11 to a large class of multiple degenerate points.

Merging Degenerate Points

In tensor fields that depend on time or on any other parameter, simple degenerate points move and eventually merge with each other, creating multiple degenerate points. In this section, we explore the qualitative nature of multiple degenerate points arising from merging a few simple degenerate points.

Figure 4.12 shows examples of multiple degenerate points created by merging two simple degenerate points belonging to the same class. Each column represents hyperstreamline patterns in one of the eigenvector fields. These combined patterns

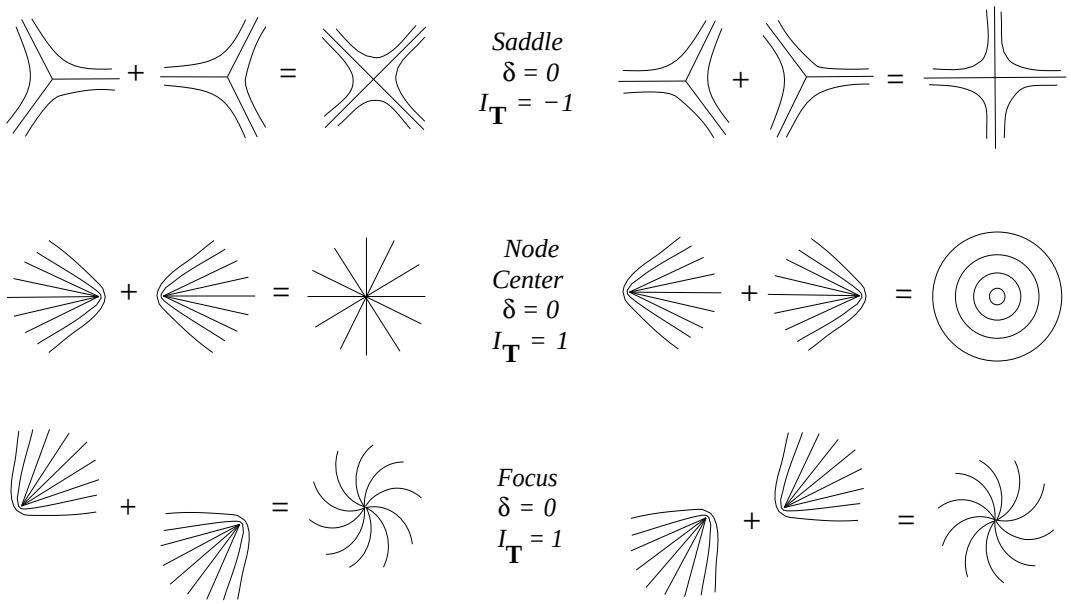

Figure 4.12: Merging degenerate points. δ = invariant of Equation 4.13, $I_{\mathbf{T}}$ = resulting tensor index. Each column represents one eigenvector field.

are created in such a way as to preserve continuity of the eigenvector fields. The patterns that arise are familiar from vector field topology. For example, two merging trisectors create a saddle point ($I_{\mathbf{T}} = -\frac{1}{2} - \frac{1}{2} = -1$) of each eigenvector field. Likewise, two merging wedge points ($I_{\mathbf{T}} = \frac{1}{2} + \frac{1}{2} = 1$) can induce simultaneously a node of one eigenvector field and a center of the other eigenvector field, or under other circumstances, they can create a pair of foci with opposite swirl.

It is interesting to note that by merging simple degenerate points of tensor fields, multiple degenerate points arise that belong to the family of critical points of continuous, signed vector fields. These multiple degenerate points can merge in turn, creating ever more complex singularities with an equivalent within the panoply of multiple critical points of vector fields (see for example Reference [68]). Figure 4.13 shows an example where four merging wedge points create two centers which merge in turn to induce a dipole ($I_{\mathbf{T}} = 1 + 1 = 2$). Dipoles are therefore multiple degenerate points arising from the simultaneous merging of four wedge points.

Merging simple degenerate points can also have a destructive effect. Wedge points

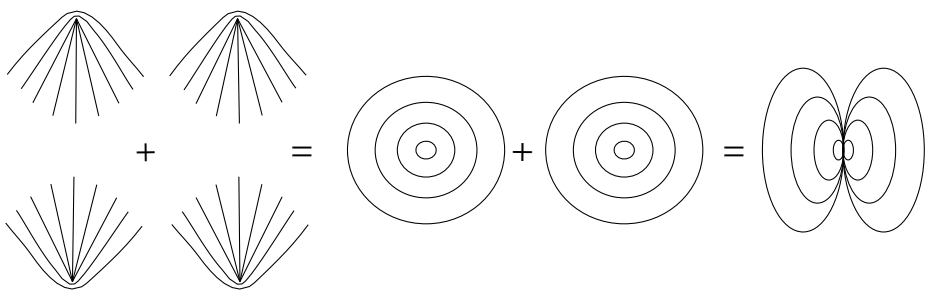

Figure 4.13: Dipole created by four merging wedge points.

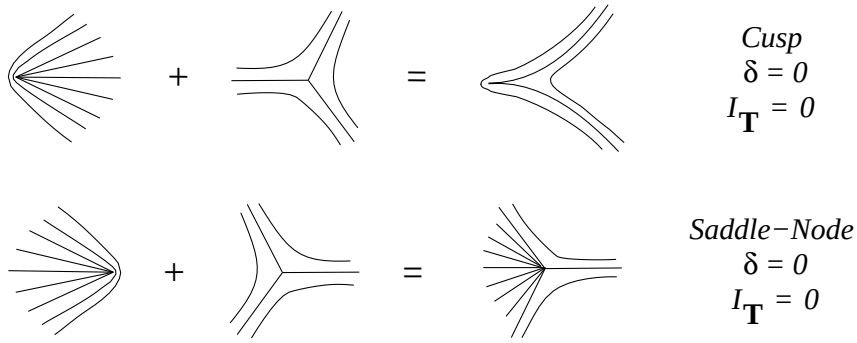

Figure 4.14: Merging wedge/trisector pairs inducing a cusp (top) and saddle-node (bottom). Each pattern appears simultaneously in one of the two eigenvector fields.

and trisectors cancel each other out by merging—i.e., they create a multiple degenerate point of index $I_{\mathbf{T}} = \frac{1}{2} - \frac{1}{2} = 0$ which is equivalent in the far field to a regular (non-degenerate) point. In a sense, it is as if the singularity vanished. This is represented in Figure 4.14 which shows a merging wedge/trisector pair inducing simultaneously a cusp (top) of one eigenvector field and a saddle-node (bottom) of the other eigenvector field. Both cusp and saddle-node can be replaced by a regular point without any global effect on the tensor field. Conversely, in tensor fields varying smoothly with time, wedge/trisector pairs can be created from regular points through an intermediate step consisting of cusps and saddle-nodes. (Examples of pair creations are discussed in Section 4.4.)

Separatrices of Multiple Degenerate Points

Now, we turn to a more quantitative discussion of multiple degenerate points. In order to make the mathematical analysis tractable, we focus on degenerate points where tensor components have Taylor expansions that start with homogeneous polynomials of the same degree—i.e., $m_p = m_q \equiv m$ in Equations 4.10. That is, we assume that tensor components can be expressed in the vicinity of a degenerate point $\vec{x}_0 = (x_0, y_0)$ as

$$\begin{cases} \frac{T_{11}-T_{22}}{2} \approx P_m(x - x_0, y - y_0) + \cdots \\ T_{12} \approx Q_m(x - x_0, y - y_0) + \cdots \end{cases} \quad (m \geq 1) \tag{4.24}$$

This leads to Theorem 12 which generalizes Theorem 11 to multiple degenerate points.

Theorem 12 *Let* $\mathbf{T}$ *be an analytic tensor field in an open subset* E *of* $\mathbf{R}^2$*, and let* $\vec{x}_0 \in E$ *be an isolated, multiple degenerate point of* $\mathbf{T}$*. Suppose that Taylor expansions of* $\frac{1}{2}(T_{11} - T_{22})$ *and* T_{12} *about* $\vec{x}_0$ *begin with* m^{th}*-degree polynomials* $P_m(x, y)$ *and* $Q_m(x, y)$*,* $m \geq 1$*, as in Equations 4.24. Let*

$$\begin{aligned} P_m(x, y) &= \sum_{i=0}^{m} p_i^{(m)} x^{m-i} y^i \\ Q_m(x, y) &= \sum_{i=0}^{m} q_i^{(m)} x^{m-i} y^i \end{aligned}$$

where coefficients $p_i^{(m)}$ *and* $q_i^{(m)}$*,* $i = 0, \ldots, m$*, are given by Equations 4.11. Then, the eigenvector fields have at* $\vec{x}_0$

1. *a multiple degenerate point with no more than $2(m+2)$ separatrices for the two eigenvector fields combined, or*

2. *a pair of foci with opposite swirl, or*

3. *a center and a star-node.*

The angles θ_k between the x-axis and the separatrices s_k are obtained by computing the real roots z_k (including infinity) of the polynomial

$$q_m^{(m)} z^{m+2} + (q_{m-1}^{(m)} + 2p_m^{(m)}) z^{m+1} + \sum_{i=2}^{m} (q_{i-2}^{(m)} + 2p_{i-1}^{(m)} - q_i^{(m)}) z^i + (2p_0^{(m)} - q_1^{(m)}) z - q_0^{(m)} = 0, \tag{4.25}$$

by inverting the relation $z_k = \tan\theta_k$, and by keeping only those angles that lie along the boundary of a hyperbolic sector. Case 2 occurs when Equation 4.25 has no real root and Case 3 occurs when all coefficients in Equation 4.25 vanish identically.

Proof. Consider a circle C with radius r and center $\vec{x}_0$ (Figure 4.9). Let S be the interior of C. The radius r is chosen to be small enough so that no degenerate points except $\vec{x}_0$ lie in $C \cup S$, and so that tensor components can be approximated by Equations 4.24 at every point of $C \cup S$.

On the circle C, $x - x_0 = r\cos\theta$ and $y - y_0 = r\sin\theta$ which implies

$$P_m(x - x_0, y - y_0) = P_m(r\cos\theta, r\sin\theta) = r^m P_m(\cos\theta, \sin\theta) = r^m \cos^m\theta \sum_{i=0}^{m} p_i^{(m)} \tan^i\theta$$

and

$$Q_m(x - x_0, y - y_0) = Q_m(r\cos\theta, r\sin\theta) = r^m Q_m(\cos\theta, \sin\theta) = r^m \cos^m\theta \sum_{i=0}^{m} q_i^{(m)} \tan^i\theta$$

Let $\alpha(\theta)$ be the angle between the x-axis and the eigenvectors at position θ on C (Figure 4.9). As in Theorem 11, angles where an eigenvector lies along the radial direction obey

$$\tan 2\theta = \tan 2\alpha(\theta) = \frac{2T_{12}}{T_{11} - T_{22}} = \frac{r^m \cos^m\theta \sum_{i=0}^{m} p_i^{(m)} \tan^i\theta}{r^m \cos^m\theta \sum_{i=0}^{m} q_i^{(m)} \tan^i\theta}$$

or,

$$\frac{2\tan\theta}{1-\tan^2\theta} = \frac{\sum_{i=0}^{m} p_i^{(m)} \tan^i\theta}{\sum_{i=0}^{m} q_i^{(m)} \tan^i\theta}$$

which is equivalent to Equation 4.25 with $z \equiv \tan\theta$.

Equation 4.25 is a polynomial of degree $m+2$ admitting as many as $m+2$ real roots z_k (including infinity), to which correspond $2(m+2)$ radial directions

$$\theta_k = \arctan z_k \quad (-\frac{\pi}{2} \leq \theta_k \leq \frac{\pi}{2})$$

and

$$\theta'_k = \theta_k + \pi$$

($k = 1, \ldots, m+2$). After discounting unwanted parabolic/parabolic, parabolic/elliptic, and elliptic/elliptic boundaries, one is left with no more than $2(m+2)$ separatrix directions.

Two particular cases are of interest. First, assume that the set of conditions

$$\begin{cases} q_0^{(m)} = 0 \\ 2p_0^{(m)} - q_1^{(m)} = 0 \\ q_{i-2}^{(m)} + 2p_{i-1}^{(m)} - q_i^{(m)} = 0 \qquad i = 2, \ldots, m \\ q_{m-1}^{(m)} + 2p_m^{(m)} = 0 \\ q_m^{(m)} = 0 \end{cases}$$

is satisfied which amounts to say that all coefficients in Equation 4.25 vanish identically. Every angle θ is a solution of Equation 4.25, and at every point of C, one eigenvector lies along the radial direction while the other eigenvector is tangent to C. Because these are the only possible orientations of the eigenvectors on C, and because the position of the eigenvectors must change continuously and smoothly along C, all the eigenvectors lying along the radial direction correspond to the same eigenvalue (major or minor); the corresponding eigenvector field possesses a star-node at $\vec{x}_0$ and the other eigenvector field has a center (orthogonality of eigenvectors).

The second particular case happens when Equation 4.25 has no real root. In this case, trajectories rotate around $\vec{x}_0$ without ever reaching it (or else there would be at least one real root to Equation 4.25). It follows that the eigenvectors have a focus at

$\vec{x}_0$. The swirl of the two foci are opposite due to the orthogonality of the eigenvector fields.

This completes the proof. □

As with simple degenerate points, if θ_k is a radial direction, so is $\theta'_k = \theta_k + \pi$, but as opposed to simple degenerate points, the same eigenvector field can be radial at both θ_k and θ'_k.

Corollary 7 *If the components of an analytical tensor field have Taylor expansions around a degenerate point starting with odd-degree polynomials—i.e., if m is odd—then the degenerate point is not a focus.*

Proof. When m is odd, Equation 4.25 is an odd-degree polynomial with real coefficients. Such a polynomial admits at least one real root, so the degenerate point cannot be a focus.

This completes the proof. □

Examples

Multiple degenerate points are varied and numerous as illustrated by the few examples below. These examples do not constitute a complete taxonomy; their purpose is to illustrate Theorem 12 and Equation 4.25.

Consider the tensor field

$$\mathbf{T}_1(\vec{x}) = \begin{pmatrix} \frac{1}{2}x^2 + 2xy + \frac{1}{2}y^2 & -x^2 + y^2 \\ -x^2 + y^2 & -\frac{1}{2}x^2 - 2xy - \frac{1}{2}y^2 \end{pmatrix}$$

which has a multiple degenerate point at the origin with $m = 2, p_0^{(2)} = \frac{1}{2}, p_1^{(2)} = 2, p_2^{(2)} = \frac{1}{2}, q_0^{(2)} = -1, q_1^{(2)} = 0$, and $q_2^{(2)} = 1$. Equation 4.25 becomes

$$z^4 + z^3 + 2z^2 + z + 1 = (z^2 + 1)(z^2 + z + 1) = 0$$

which does not admit any real root. This corresponds to Case *2* in Theorem 12, and $\mathbf{T}_1$ exhibits a pair of foci with opposite swirl at the origin. The textures in

Figure 4.15: Textures representing the eigenvectors of $\mathbf{T}_1(\vec{x})$. The tensor exhibits two foci at the origin. Color encodes the square root of the difference between the eigenvalues according to color scale 2 of Figure A.3.

Figure 4.16: Textures representing the eigenvectors of $\mathbf{T}_2(\vec{x})$. The tensor exhibits a center and a star-node at the origin. Color encodes the square root of the difference between the eigenvalues according to color scale 2 of Figure A.3.

Figure 4.15 represent the two foci. The index is $I_{\mathbf{T}_1} = 1$ and both eigenvector fields are characterized by $n_h = n_e = n_p = n_s = 0$.

Next, consider the tensor field

$$\mathbf{T}_2(\vec{x}) = \begin{pmatrix} x^2 - y^2 & 2xy \\ 2xy & x^2 - y^2 \end{pmatrix}$$

which admits a multiple degenerate point at the origin with $m = 2, p_0^{(2)} = 1, p_1^{(2)} = 0, p_2^{(2)} = -1, q_0^{(2)} = 0, q_1^{(2)} = 2$, and $q_2^{(2)} = 0$. All coefficients in Equation 4.25 vanish identically, which corresponds to Case *3* of Theorem 12. As shown by the textures in Figure 4.16, $\mathbf{T}_2$ has a star-node and a center at the origin. The index is $I_{\mathbf{T}_2} = 1$. The radial eigenvector is characterized by $n_h = n_e = n_s = 0$ and $n_p = 1$, while the tangent eigenvector has $n_h = n_e = n_s = n_p = 0$.

Another example of a $m = 2$ multiple degenerate point is the origin of the tensor field

$$\mathbf{T}_3(\vec{x}) = \begin{pmatrix} x^2 - 3y^2 & -5xy + 4y^2 \\ -5xy + 4y^2 & x^2 - 3y^2 \end{pmatrix}$$

in which case Equation 4.25 becomes

$$4z^4 - 11z^3 - 4z^2 + 7z = 0$$

which admits for real roots $z_1 = -0.849, z_2 = 0, z_3 = 0.713$, and $z_4 = 2.886$. The corresponding radial directions are $\theta_1 = 139.64°$, $\theta_1' = 319.64°$, $\theta_2 = 0°$, $\theta_2' = 180°$, $\theta_3 = 35.51°$, $\theta_3' = 215.51°$, $\theta_4 = 70.89°$, and $\theta_4' = 250.89°$. The textures in Figure 4.17 show that $\mathbf{T}_3$ has two saddle points at the origin. Each eigenvector field has $n_h = 4$ hyperbolic and $n_e = 0$ parabolic sectors. So the index is $I_{\mathbf{T}_3} = -1$. In addition, both eigenvector fields have $n_p = 0$ parabolic sectors and $n_s = 4$ separatrices. Each radial direction is a separatrix, reaching the theoretical maximum $2(m + 2)$ separatrices in total. This example shows that, as opposed to simple degenerate points, separatrices positioned 180° apart do not especially belong to different eigenvector fields.

More exotic patterns can arise. For example, the tensor field

$$\mathbf{T}_4(\vec{x}) = \begin{pmatrix} -x^2 + y^2 & -x^2 - 2xy + y^2 \\ -x^2 - 2xy + y^2 & -x^2 + y^2 \end{pmatrix}$$

Figure 4.17: Textures representing the eigenvectors of tensor field $\mathbf{T}_3(\vec{x})$. The tensor exhibits two saddle points at the origin. Superimposed are the separatrices. Color encodes the square root of the difference between the eigenvalues according to color scale 2 of Figure A.3.

possesses a $m = 2$ multiple degenerate point at the origin. Radial directions are given by Equation 4.25:

$$z^4 - 2z^2 + 1 = (z^2 - 1)^2 = 0$$

which admits real roots at angles $\pm 45°$ and $\pm 135°$, respectively. None of these radial directions is a separatrix. $\mathbf{T}_4$ has a node and a center at the origin. The pattern of hyperstreamlines is represented in Figure 4.18. $n_h = n_e = 0$ so the index is $I_{\mathbf{T}_4} = 1$. The radial eigenvector field has $n_p = 1$ parabolic sector and $n_s = 0$ separatrices; the other eigenvector field has $n_p = 0$ parabolic sectors and $n_s = 0$ separatrices.

Finally, the origin is a $m = 4$ multiple degenerate point of the tensor field

$$\mathbf{T}_5(\vec{x}) = \begin{pmatrix} x^4 - \frac{1}{2}x^2y^2 + y^4 & 2x^4 - 5x^3y - 9xy^3 \\ 2x^4 - 5x^3y - 9xy^3 & x^4 - \frac{1}{2}x^2y^2 + y^4 \end{pmatrix}$$

Equation 4.25 becomes

$$0z^6 - 7z^5 + 3z^3 + 2z^2 + 7z - 2 = 0$$

There are three finite roots, $z_1 = -1.100, z_2 = 0.260$, and $z_3 = 1.127$, and one infinite root $z_4 = \infty$. The corresponding radial directions are $\theta_1 = -47.73°$, $\theta_1' = 132.27°$, $\theta_2 = 14.58°$, $\theta_2' = 194.58°$, $\theta_3 = 48.41°$, $\theta_3' = 228.41°$, $\theta_4 = -90°$, and $\theta_4' = 90°$. Figure 4.19 represents the eigenvector fields. There are $n_h = 2$ hyperbolic and $n_e = 0$ sectors per eigenvector field, so the index is $I_{\mathbf{T}_5} = 0$. Six of the eight radial directions are separatrices. One eigenvector field has $n_p = 0$ parabolic sectors and $n_s = 2$ separatrices; the other eigenvector field has $n_p = 2$ parabolic sectors and $n_s = 4$ separatrices. $\mathbf{T}_5$ illustrates that, as opposed to simple degenerate points, eigenvector fields around multiple degenerate points do not generally have the same number of parabolic sectors or the same number of separatrices. The difference $n_e - n_h$ is preserved (Corollary 3) but n_h, n_e, n_p, and n_s can differ individually.

4.3.5 Limit Cycles

In the former sections, we defined separatrices as hyperstreamline trajectories lying at the boundaries of hyperbolic regions (Definition 10). So defined, separatrices emanate

Figure 4.18: Textures representing the eigenvector fields of a node of $\mathbf{T}_4(\vec{x})$. The tensor exhibits a node and a center at the origin. Color encodes the square root of difference between the eigenvalues according to color scale 2 of Figure A.3.

Figure 4.19: Textures representing the eigenvector fields of $\mathbf{T}_5(\vec{x})$. The tensor exhibits a multiple degenerate point with $n_h = 2$ hyperbolic sectors. Superimposed are the separatrices. Color encodes the fourth root of the difference between the eigenvalues according to color scale 2 of Figure A.3.

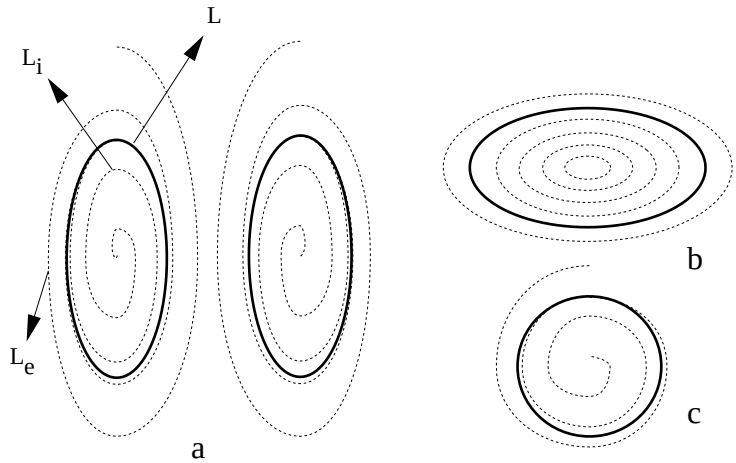

Figure 4.20: a: two limit cycles of a continuous tensor field; b and c: closed trajectories that are not limit cycles after Definition 12.

from degenerate points. In this section, we define yet another type of separatrices which do not originate from degenerate points. We call these trajectories "limit cycles" by analogy to vector fields. A precise definition follows:

Definition 12 (Limit Cycle) *Let* $\mathbf{T}$ *be a continuous tensor field, and let* L *be a hyperstreamline cycle of* $\mathbf{T}$ *not passing through any degenerate point. Let* S_i *be* L*'s interior and* S_e *be* L*'s exterior. Then,* L *is a limit cycle of* $\mathbf{T}$ *iff there exist two open neighborhoods of* L*,* $N_i \subset S_i$ *and* $N_e \subset S_e$*, such that all trajectories within* $N_i \cup N_e$ *are either converging towards* L *or diverging away from* L*, when moving along* L *in a constant direction.*

Because they draw geometric boundaries that separate trajectories in their interior from trajectories in their exterior, limit cycles play a role similar to separatrices emanating from degenerate points.

Since they do not include any degenerate points, limit cycles are Jordan curves. Indeed, they are closed, continuous and smooth (continuity of $\mathbf{T}$), and simple (see proof of Theorem 6). It is, therefore, always possible to distinguish between the interior and the exterior of limit cycles.

Figure 4.20 (a) shows two limit cycles L together with representative trajectories from L's interior (L_i) and exterior (L_e). For L to qualify as a limit cycle, L_i and L_e

must both converge or diverge when moving in a constant direction along L. (This is the case in Figure 4.20 (a).) Conversely, Figures 4.20 (b) and 4.20 (c) represent closed trajectories that are not limit cycles. Figure 4.20 (b) shows trajectories in the vicinity of a center where neighboring hyperstreamlines propagate parallel to L without ever converging nor diverging. L is a cycle within a band of cycles, but not a limit cycle after Definition 12. Neither is the trajectory represented in Figure 4.20 (c), where one trajectory diverges away from L while the other trajectory converges towards L.

Limit cycles typically occur in complex tensor fields that are not solenoidal. (Solenoidal tensor fields are to be discussed in Theorem 13 below.) An example is given in Figure 4.21, which represents Reynolds stresses (stresses induced by the turbulent motion) in a 2-D flow past a cylinder at one instant in time. The texture encodes the eigenvector associated to the positive eigenvalue (traction) of the Reynolds-stress tensor. Red and white dots are wedge points and trisectors, respectively. The two superimposed curves are limit cycles. All hyperstreamline trajectories that propagate in clockwise direction within the cycles' interiors or within some nearby exterior neighborhood, end up trapped in an indefinite, periodic motion along the limit cycles.[6] We computed the limit cycles in Figure 4.21 by integrating hyperstreamlines from points located inside the cycles' basins of attraction, and by retaining only the final, periodic component of their trajectories.

In the remaining of this section, we discuss "simple" limit cycles. In this case, the convergence / divergence of surrounding hyperstreamlines is strong enough to be measured as a first-order function of the transverse distance, which amounts to say that the first-order derivative of the Poincaré map does not vanish (Reference [69]). The following theorems are properties of solenoidal tensor fields.

Theorem 13 *2-D solenoidal tensor fields do not have simple limit cycles.*

Proof. Let L be a limit cycle of a solenoidal tensor field. We shall prove that L cannot exist. Trajectories on both sides of L either converge towards L or diverge away from L, when moving in a constant direction along L. This simple behavior of neighboring trajectories and the absence of degenerate points on L allow us to

[6] The convergence, however, is fairly slow and hard to notice by simple inspection of the textures.

Figure 4.21: Textures representing the major eigenvector field (traction) of Reynolds stresses in a 2-D flow past a cylinder. Superimposed are two limit cycles. White dots are trisector points and red dots are wedge points. Color encodes the magnitude of the longitudinal Reynolds stress according to color scale 2 of Figure A.3.

continuously confer a sign to the eigenvector fields within the domain $N_i \cup L \cup N_e$ (Definition 12). It follows from Theorem 1 that

$$\lambda_l' = K_{lt}(\lambda_l - \lambda_t)$$

in $N_i \cup L \cup N_e$, where λ_l and λ_t are the longitudinal and transverse eigenvalues, respectively. λ_l' is the derivative of the longitudinal eigenvalue along L, and K_{lt} is positive or negative depending on whether neighboring trajectories converge or diverge.

Let P be any point on L. L being a closed curve and solenoidal tensor fields being continuous,

$$\lambda_l(P) + \oint_{L^+} \lambda_l' ds = \lambda_l(P)$$

which implies that

$$\oint_{L^+} \lambda_l' ds = \oint_{L^+} K_{lt}(\lambda_l - \lambda_t) ds = 0$$

However, this is not possible because the integrand has a constant sign along L. Thus, L does not exist.

This completes the proof. □

Again, there is complete analogy between the properties of solenoidal tensor and vector fields. We can indeed use a similar argument to show that solenoidal vector fields do not have simple limit cycles such as those in Figure 4.20 (a) (Reference [69]). Their only admissible periodic trajectories are cycles within a band of cycles (Figure 4.20 (b)), semi-stable cycles (Figure 4.20 (c)), or limit cycles with higher-order convergence / divergence (vanishing first-order derivative of the Poincaré map—Reference [69]).

The following theorem extends this result to 3-D solenoidal tensor fields.

Theorem 14 *The major and minor eigenvectors of 3-D solenoidal tensor fields do not have structures such as the simple attractor cycles shown in Figure 4.22.*

Proof. The proof is similar to Theorem 13, but requires using Equation 3.8 instead of Equation 3.7.

This completes the proof. □

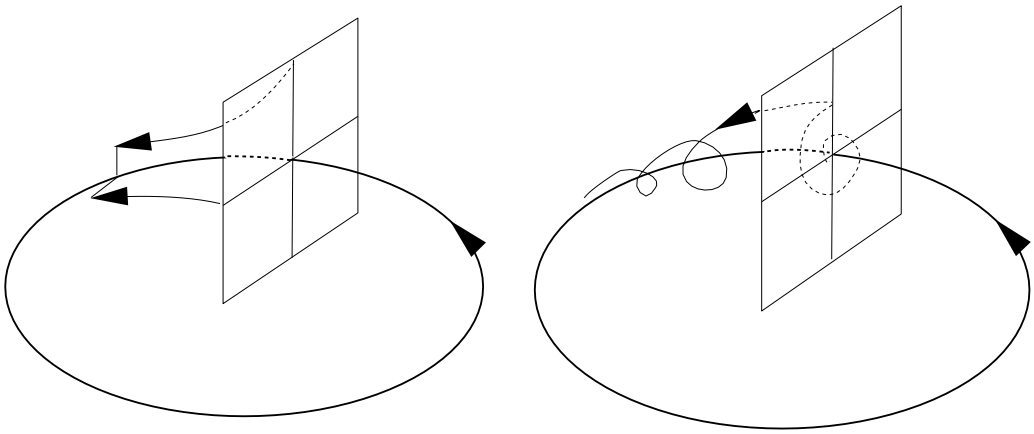

Figure 4.22: Attractor cycles in 3-D tensor fields.

In the next section, we show how to extract topological skeletons built from separatrices that emanate from degenerate points. In order to obtain complete topological depictions of tensor fields, we must add any eventual limit cycles (or attractor cycles in 3-D).

4.4 Tensor Field Topology

We build on the theory of degenerate points to extract the topology of tensor fields and to study topological transitions. The technique is similar to vector field topology with degenerate points playing the role of critical points. We represent each eigenvector field by a topological skeleton obtained by locating degenerate points and integrating the set of their connecting separatrices.

We illustrate these concepts by visualizing the topology of the stress tensor in a 2-D periodic flow past a cylinder.[7] Fluid elements undergo compressive stresses while moving with the flow. Stresses are described mathematically by the stress tensor, which combines isotropic pressure and anisotropic viscous stresses (Table 1.2). Both

[7] An accompanying video tape is available upon request from Prof. Lambertus Hesselink, Department of Electrical Engineering, Stanford University.

eigenvalues of the stress tensor are negative and the two orthogonal eigenvectors, $\vec{v}_1$ and $\vec{v}_2$ (Equation 4.1), are along the least and the most compressive directions, respectively. At a degenerate point, the viscous stresses vanish and both eigenvalues are equal to the pressure; degenerate points are points of pure pressure.

The textures in Figure 4.23 show the flow (velocity field) at two representative time steps. The flow consists of the periodic detachment of a separation bubble, with repeated shedding downstream of saddle/center pairs. Color encodes velocity magnitude, from fast (red) to slow (blue).

Video Clip 1. This clip shows a moving texture representing the periodic evolution of the flow over time. Color encodes velocity magnitude as in Figure 4.23, from fast (red) to slow (blue). Slow regions correspond to saddle/center pairs originating on the cylinder's surface as detachment bubbles alternatively above and below the cylinder's symmetric axis.

$\diamondsuit$

4.4.1 Tracking Degenerate Points

The first step for understanding the structure of the stress-tensor field consists in tracking the motion of degenerate points over time. We locate degenerate points at each time step by seeking solutions to Equations 4.3. We process each grid cell one after the other as detailed in Appendix B.

Figure 4.24 shows results at a specific instant in time. The dots mark the location of simple degenerate points. The top view shows the overall data while the bottom view focuses on the region close to the body. The colored background encodes the magnitude λ_2 of the most compressive force, from very compressive (red), to mildly compressive (orange, yellow, green), to little compressive (blue). Wedge points and trisectors are represented as black and white dots, respectively. It is shown clearly that wedge points are situated in the wake about the cylinder axis while trisector points are located off-axis. The images in Figure 4.24 belong to two video clips that visualize the motion of degenerate points over time.

Figure 4.23: Frames of Video Clip 1 showing the flow at two representative time steps. Color encodes velocity magnitude from fast (red) to slow (blue), according to color scale 2 of Figure A.3.

Figure 4.24: Frames of Video Clips 2 and 3 showing the motion of degenerate points of the stress-tensor field over time. Wedge points are represented as black dots and trisectors are white dots. Color encodes the most compressive eigenvalue, λ_2, from very compressive (red), to mildly compressive (orange, yellow, green), to little compressive (blue). We use color scale 2 of Figure A.3.

Video Clips 2 and 3. We visualize the motion of degenerate points of the stress-tensor field. The colored background is as in Figure 4.24. We show wedge points as black dots and trisectors as white dots. Video Clip 2 represents the overall structure of the motion and Video Clip 3 focuses on the region closer to the body. The video clips show periodic creations of wedge/trisector pairs alternatively above and below the cylinder's symmetry axis. These pair-creation events are clearly tied to each region of low compressive stresses (blue color).

$\diamondsuit$

Figure 4.24 contains valuable information but we can learn more about the spatiotemporal structure of the tensor field by representing in a still image, the trajectories followed by degenerate points over time. Figure 4.25 shows these trajectories in three-dimensional space. The third dimension is time, increasing from front to back. The figure represents one period of the evolution of the flow. Red spheres are wedge points and green spheres are trisectors.

Interesting phenomena occur at locations marked by the letters "C" and "M", respectively. C-events are creations of wedge-trisector pairs from regular points, and M-events correspond to pair cancellation by merging. As discussed in Section 4.3.4, both processes of creating and cancelling wedge-trisector pairs are topologically consistent since they conserve the local index. In some instances, pair creations affect only the local flow; the two newly created points move together and eventually disappear by merging. Two C-events, however, are different; the newly created points move far away from each other, inducing a topological transition of the tensor field. These new wedge-trisector pairs are created periodically in a location above and below the axis of symmetry, alternatively. New wedge points are quickly dragged into the wake about the cylinder's axis while new trisectors move downstream away from the axis.

4.4.2 Correlating Vector and Tensor Data

Tensor data are highly multivariate and rich in information content but they are also complex and poorly understood, while vector data are simpler and more familiar. It

Figure 4.25: Spatiotemporal trajectories of degenerate points in the stress-tensor field. Time increases from front to back. Red spheres = wedges, green spheres = trisectors. M and C indicate merging and creation of wedge-trisector pairs, respectively.

can be useful to correlate visually tensor and vector fields, not only for our basic understanding of tensor data, but also for gleaning new physical insights into vector fields. In this section we correlate velocity field and stress tensor.

Video Clip 4. The moving texture encodes the direction of the velocity field. Color encodes the magnitude of the most compressive eigenvalue, λ_2, from very compressive (red), to mildly compressive (orange, yellow, green), to little compressive (blue). Overlaid are the degenerate points of the stress tensor. Wedge points and trisectors are represented as black and white dots, respectively.

$\diamondsuit$

Figure 4.26 represents one frame from this clip. (Here wedge points are drawn in red.) Texture and color indicate clearly that detachment bubbles (saddle-center pairs of the velocity field) are regions of low compressive stresses. The motion of the degenerate points is interesting. The wedge point A originates by pair creation then follows the detachment bubble in its motion downstream. In fact, a new pair is created with each new bubble. The oscillating pair B is closely associated to the recirculation regions close to the body surface. The wedge C follows a stable orbit shaped as an 8. It rolls back and forth between two consecutive bubbles without ever venturing inside.

4.4.3 Topological Skeletons

We obtain topological skeletons by detecting degenerate points and integrating the set of their connecting separatrices. Trisector points in tensor fields play the topological role of saddle points in vector fields. As shown in Figures 4.7 and 4.8, they deflect adjacent trajectories in any one of their three hyperbolic sectors toward topologically distinct regions of the domain. Wedge points possess both a hyperbolic and a parabolic sector. They deflect trajectories adjacent in their hyperbolic sector, and terminate trajectories impinging on their parabolic sector.

Figure 4.26: A frame of Video Clip 4 showing the correlation between the velocity field (moving texture) and the degenerate points of the stress tensor. Color encodes the most compressive stresses, from very compressive (red), to mildly compressive (orange, yellow, green), to little compressive (blue). Red dots = wedges, white dots = trisectors.

Here follows an algorithm to extract the topology of a tensor field. This simplified version handles simple degenerate points only:[8]

1. locate degenerate points by searching for solutions to Equations 4.3 in every grid cell (this step is detailed in Appendix B);

2. classify each degenerate point as a trisector ($\delta < 0$) or a wedge point ($\delta > 0$) by evaluating a, b, c, d using Equations 4.11 and computing $\delta = ad - bc$; send a warning message if a multiple degenerate point ($\delta = 0$) is detected;[9]

3. select an eigenvector field;

4. solve Equation 4.18 to find the directions of the three separatrices (s_1, s_2, s_3) at each trisector point (Figure 4.7—top); likewise, extract separatrices (s_1, s_2) at wedge points where Equation 4.18 admits three real roots[10] (Figure 4.7—bottom left) and extract the unique separatrix at wedge points where Equation 4.18 has only one real root (Figure 4.7—bottom right);

5. integrate hyperstreamlines along the separatrices;[11] terminate the trajectories wherever they leave the domain, or impinge on the parabolic sector of a wedge point.[12]

Figure 4.27 shows an example. The texture represents the most compressive eigenvector of the stress tensor ($\vec{v}_2$). Color encodes as before the magnitude of the compressive force (λ_2), from most compressive (red) to least compressive (blue). We emphasize the structure of the tensor field by superimposing the topological skeleton of $\vec{v}_2$. These time-dependent data are complex, and we find that the spatiotemporal

[8] More complex algorithms are necessary to extract automatically multiple degenerate points (Section 4.3.4) and limit cycles (Section 4.3.5).

[9] In practice, we avoid roundoff problems by using a threshold ϵ, $0 < \epsilon \ll 1$, and considering that the degenerate point is multiple if $|\delta| \leq \epsilon$.

[10] We keep only the smallest and the largest of the three angles that define radial direction of each eigenvector field.

[11] In practice, we start integrating at a location a small distance away from the degenerate point in the direction of the separatrices.

[12] In practice, we terminate trajectories propagating within the parabolic sector of a wedge point at a distance smaller than a given threshold.

Figure 4.27: A frame of Video Clip 5 showing the instantaneous topology of the most compressive eigenvector $\vec{v}_2$. Color encodes λ_2, from very compressive (red), to mildly compressive (orange, yellow, green), to little compressive (blue). W = wedge points, T = trisectors.

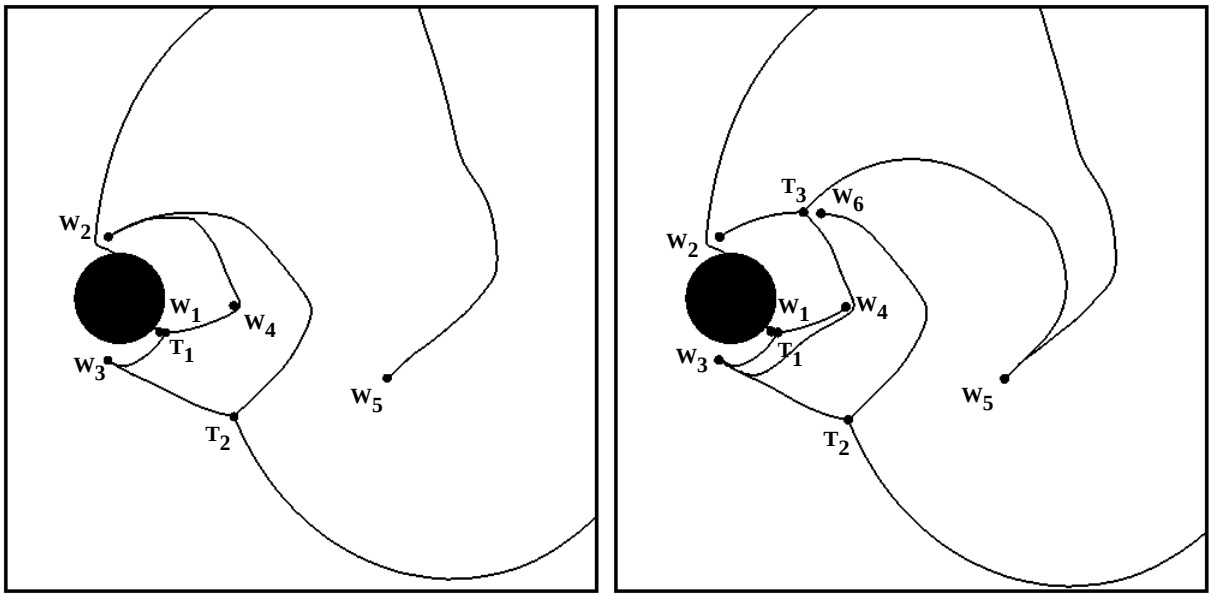

Figure 4.28: Two consecutive frames showing a topological transition of the stress-tensor field.

structure of the tensor field is conveyed more efficiently by simplifying the skeletons and displaying only the separatrices that originate at trisector points, leaving aside the separatrices that emanate from wedge points.

We can infer the orientation of the eigenvectors at any point in the plane from the topological skeleton: hyperstreamlines curve their trajectories so as to follow the shape of the separatrices, bending around wedge points. In Figure 4.27 for example, wedge points are located around the cylinder's axis and trisectors quickly move off-axis. The separatrices that emanate from the trisector points delineate the global structure of the most compressive eigenvector; hyperstreamlines oscillate about the cylinder's axis, presenting a distorted, wave-like pattern with sharp turns at the wedge points.

With time, the repeated creation of new wedge-trisector pairs induces periodic topological transitions, which we illustrate in Figure 4.28. The newly created pair $\{T_3, W_6\}$ changes the topological structure of the tensor field. Hyperstreamline trajectories which used to follow the separatrices $W_3 - T_1 - W_4 - W_2$ and $W_3 - T_2 - W_2$,

ended trapped in the parabolic sector of W_2; now, they sweep pass the new trisector T_3—bending along the hyperbolic sector of W_6—and pursue their course further downstream.

As with vector field topology, the power of the representation comes from its simplicity; a few points and lines suffice to reveal the directional information otherwise buried within abundant multivariate data.

Video Clips 5 and 6. The two clips show the evolution with time of the topological skeleton in Figure 4.27, with and without the textured background. Black dots represent wedge points and white dots are trisectors. Topological transitions such as the one represented in Figure 4.28 occur periodically, first above then below the cylinder's symmetry axis.

$\diamondsuit$

By using textures or topological skeletons, we render tensor information only partially. We discussed in Section 3.2.2 a technique to correlate the two eigenvector fields within a single display. Another example is given in Figure 4.29 where we use texture, color, and elevation as channels to encode eigenvector direction, longitudinal eigenvalue, and transverse eigenvalue, respectively. The texture is the same as in Figure 4.27. In addition to topological information, the display reveals a strong correlation between the two eigenvalues—a fact that was previously overlooked in "flat" representations of one eigenvector field, such as Figure 4.27.

4.5 Tensor Topological Rule

When a tensor field is defined across a surface $\mathbf{M}$, the topology of $\mathbf{M}$ puts a constraint on the number and nature of degenerate points, considerably limiting the variety of possible tensor patterns. We investigate this constraint in this section.

Figure 4.29: Trivariate data visualization to fully represent the stress-tensor field. The texture and the topological skeletons show the most compressive eigenvector $\vec{v}_2$. Color encodes λ_2, from very compressive (red), to mildly compressive (orange, yellow, green), to little compressive (blue). Red dots are wedge points and white dots are trisectors. The elevation of the surface encodes the least compressive eigenvalue, λ_1.

M	$\chi(\mathbf{M})$
sphere	2
torus	0
2-holed torus	-2
g-holed torus	2 - 2 g

Table 4.4: Euler characteristic of generic surfaces.

Euler Characteristic

The topology of any surface $\mathbf{M}$ is unambiguously characterized by a single number $\chi(\mathbf{M})$ called the surface's Euler characteristic [71]. All orientable[13] homeomorphic surfaces (i.e., the set of orientable surfaces that can be distorted to look identical by continuous bending, stretching, or squashing, but without tearing or gluing) have the same value of $\chi(\mathbf{M})$. The Euler characteristic $\chi(\mathbf{M})$ is related to the number of "holes" in $\mathbf{M}$ which is called the surface's genus, $g(\mathbf{M})$. The relation between $\chi(\mathbf{M})$ and $g(\mathbf{M})$ is

$$\chi(\mathbf{M}) = 2 - 2g(\mathbf{M}) \tag{4.26}$$

For example, a sphere and a cube are homeomorphic with $g(\mathbf{M}) = 0$ and $\chi(\mathbf{M}) = 2$. A torus and a coffee mug are homeomorphic with $g(\mathbf{M}) = 1$ and $\chi(\mathbf{M}) = 0$. Table 4.4 summarizes $\chi(\mathbf{M})$ for a few generic surfaces.

Vector Fields Tangent to 2-D Surfaces

Consider a vector field $\vec{v}(\vec{x})$ tangent to a 2-D surface $\mathbf{M}$. That is, at each point $\vec{x}$ of $\mathbf{M}$, the vector $\vec{v}(\vec{x})$ lies in the plane tangent to $\mathbf{M}$ at $\vec{x}$. A classical theorem of surface topology, known as the Poincaré-Hopf theorem (Reference [72]), establishes a link between the topology of the surface $\mathbf{M}$ and the topology of the vector field $\vec{v}(\vec{x})$ on $\mathbf{M}$. Indeed, this theorem, also known as the Poincaré Index Theorem, stipulates that under appropriate conditions of continuity and differentiability of both vector field and surface, the sum of the indices at the critical points of $\vec{v}(\vec{x})$ is equal to $\chi(\mathbf{M})$. Thus, if $\vec{v}(\vec{x})$ has $\mathcal{N}$ nodes, $\mathcal{C}$ centers, $\mathcal{F}$ foci, and $\mathcal{S}$ saddles on $\mathbf{M}$, the total

[13]See Reference [71] for a precise definition of surface orientability. Most of the surfaces in every day life are orientable. Notable exceptions include Möbius bands and Klein bottles.

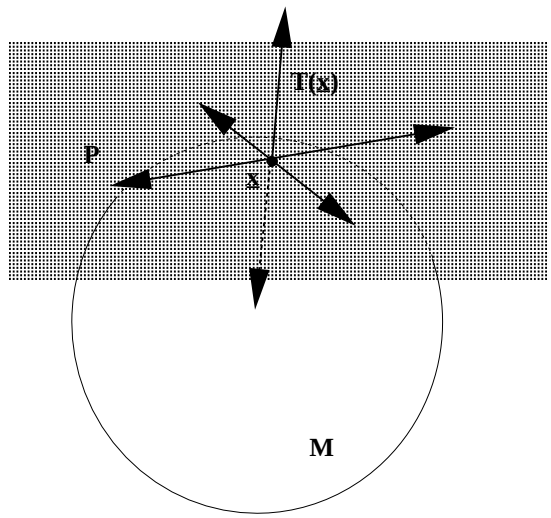

Figure 4.30: A tensor field defined across an orientable surface $\mathbf{M}$.

index is $\mathcal{N} + \mathcal{C} + \mathcal{F} - \mathcal{S} = \chi(\mathbf{M})$. This result shows how the topology of the surface $\mathbf{M}$—i.e., $\chi(\mathbf{M})$—affects the structure of any vector field tangent to $\mathbf{M}$—i.e., the sum $\mathcal{N} + \mathcal{C} + \mathcal{F} - \mathcal{S}$.

Tensor Fields Tangent to 2-D Surfaces

In the following, we extend the Poincaré-Hopf theorem to symmetric tensor fields $\mathbf{T}(\vec{x})$ that are tangent to orientable, 2-D surfaces $\mathbf{M}$. The data under consideration are 3-D symmetric tensor fields $\mathbf{T}(\vec{x})$ that are defined across an open subset $E \subset \mathbf{R}^3$ such that $\mathbf{M} \subset E$ and that have at every point $\vec{x}$ of $\mathbf{M}$ two orthogonal eigenvectors lying in the plane tangent to $\mathbf{M}$ at $\vec{x}$ (Figure 4.30). It is clear that $\mathbf{T}$ possesses a third eigenvector field directed along the normal to $\mathbf{M}$, but we confine the discussion to the system of two eigenvector fields tangent to $\mathbf{M}$. We assume that $\mathbf{T}$ has a finite number of isolated degenerate points on $\mathbf{M}$, and that these degenerate points never involve the eigenvalue corresponding to the normal eigenvector. Thus, when referring to "degenerate point of $\mathbf{T}$ on $\mathbf{M}$" we really mean "degenerate point of the two tangent eigenvector fields." Further, the condition $\mathbf{T} \in C^1(\mathbf{M})$ means that the two tangent eigenvector fields are continuous across $\mathbf{M}$ except at the location of eventual

degenerate points.

Tensor Index of a Surface

We can define the index of an orientable surface $\mathbf{M}$ with respect to a tensor field $\mathbf{T}$ tangent to $\mathbf{M}$, by extending to surfaces the notion of index of a Jordan curve (Equation 4.7).

Definition 13 (Tensor Index of a Surface) *Let $\mathbf{T} \in C^1(\mathbf{M})$ be a tensor field tangent to an orientable surface $\mathbf{M}$. Assume that $\mathbf{T}$ has m isolated degenerate points $\vec{x}_i \in \mathbf{M}$, $i = 1, \ldots, m$. Then, the tensor index of the surface $\mathbf{M}$ with respect to the tensor field $\mathbf{T}$ is*

$$I_{\mathbf{T}}(\mathbf{M}) = \sum_{i=1}^{m} I_{\mathbf{T}}(\vec{x}_i)$$

where $I_{\mathbf{T}}(\vec{x}_i)$ is the tensor index at $\vec{x}_i$.

In order to analyze how the topology of $\mathbf{M}$ affects the topology of $\mathbf{T}$, we make the following assumption:

Conjecture 1 *The tensor index of a sphere $\mathbf{S}$ with respect to a tangent tensor field $\mathbf{T} \in C^1(\mathbf{S})$ is a constant number independent of the particular tensor field $\mathbf{T}$.*

This conjecture is certainly true for continuous vector fields (see for example References [73, 69]) and we assume that it remains true for continuous tensor fields—i.e., for continuous but unsigned eigenvector fields.

Figure 4.31 represents a possible pattern for an eigenvector field tangent to a sphere $\mathbf{S}$. The topological skeleton consists of $\mathcal{T} = 2$ trisectors and $\mathcal{W} = 6$ wedge points. It follows that the tensor index of a sphere $\mathbf{S}$ with respect to the particular tensor field represented in Figure 4.31, and by virtue of the above conjecture, with respect to any continuous, tangent tensor field $\mathbf{T}$ is given by

$$I_{\mathbf{T}}(\mathbf{S}) = 4 \times \frac{1}{2} - 2 \times \frac{1}{2} = 2 \tag{4.27}$$

From there on we can infer the link between the topology of a surface $\mathbf{M}$ and the topology of tensor fields $\mathbf{T}$ tangent to $\mathbf{M}$:

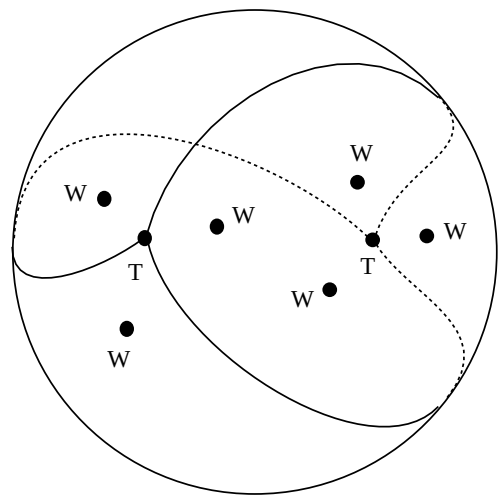

Figure 4.31: A tensor field tangent to a sphere **S**. T's are trisectors and W's are wedge points.

Theorem 15 *The tensor index $I_{\mathbf{T}}(\mathbf{M})$ of a 2-D orientable surface* **M** *relative to a tangent tensor field $\mathbf{T} \in C^1(\mathbf{M})$, with at most a finite number m of degenerate points on* **M**, *is independent of* **T** *and is equal to the Euler characteristic of* **M**. *Thus,*

$$I_{\mathbf{T}}(\mathbf{M}) = \sum_{i=1}^{m} I_{\mathbf{T}}(\vec{x}_i) = \chi(\mathbf{M}) \tag{4.28}$$

where $\vec{x}_i$, $i = 1, \ldots, m$, are isolated degenerate points of **T** *on* **M** *and $I_{\mathbf{T}}(\vec{x}_i)$, $i = 1, \ldots, m$, are the associated tensor indices.*

Proof. First, we show that the tensor index of an orientable surface **M** with genus $g(\mathbf{M})$ is given by

$$I_{\mathbf{T}}(\mathbf{M}) = (1 - g(\mathbf{M}))I_{\mathbf{T}}(\mathbf{S}) \tag{4.29}$$

where $I_{\mathbf{T}}(\mathbf{S})$ is the tensor index of a sphere. Equation 4.29 was proven by Gomory in the case of continuous vector fields defined across surfaces. Here we reproduce the proof given in Reference [69], pp. 284-285. This proof applies to continuous tensor fields as well, because it is purely topological; nowhere does the reasoning rely on the vector field being signed or on the specific nature of the singularities—i.e., critical versus degenerate points.

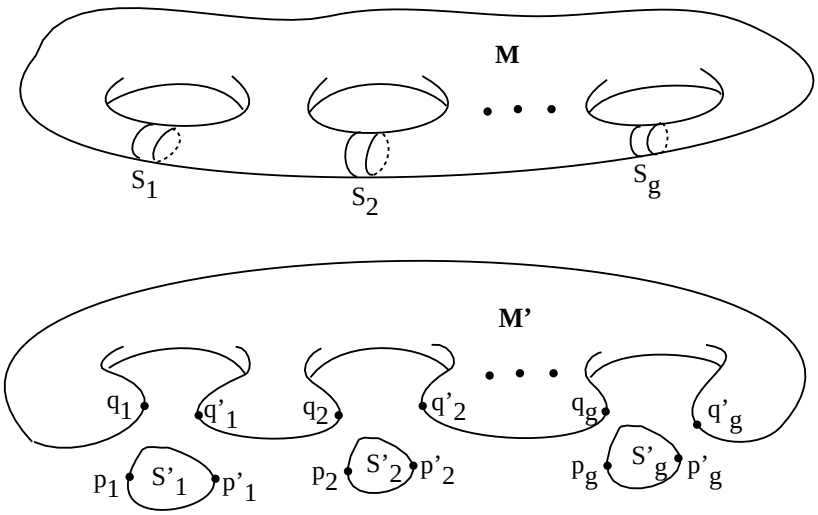

Figure 4.32: Calculation of the tensor index of a surface of genus $g(\mathbf{M})$.

The surface $\mathbf{M}$ of genus $g(\mathbf{M})$ is homeomorphic to the $g(\mathbf{M})$-holed torus represented in Figure 4.32 (top). (This is also the topological equivalent of a sphere with $g(\mathbf{M})$ handles.) Suppose that the tensor field $\mathbf{T}$ has only a finite number of degenerate points on $\mathbf{M}$. As in Figure 4.32 (top), cut out at each hole of $\mathbf{M}$ a narrow section S_i, $i = 1, \ldots, g(\mathbf{M})$, which does not contain any degenerate point. Then, shrink the boundaries of S_i to the points p_i and p_i' and the boundaries of $\mathbf{M}$ to the points q_i and q_i' as in Figure 4.32 (bottom).

Let us denote $\mathbf{M}'$ and S_i', $i = 1, \ldots, g(\mathbf{M})$, the resulting surfaces. The shrinking of the boundaries to the points q_i and q_i' introduces new singularities on $\mathbf{M}'$. Thus,

$$I_{\mathbf{T}}(\mathbf{M}') = I_{\mathbf{T}}(\mathbf{M}) + \sum_{i=1}^{g(\mathbf{M})} (I_{\mathbf{T}}(q_i) + I_{\mathbf{T}}(q_i')) \tag{4.30}$$

The surface $\mathbf{M}'$ is homeomorphic to a sphere $\mathbf{S}$, so

$$I_{\mathbf{T}}(\mathbf{M}') = I_{\mathbf{T}}(\mathbf{S}) \tag{4.31}$$

It is also true that

$$I_{\mathbf{T}}(q_i) = I_{\mathbf{T}}(p_i)$$

and that

$$I_{\mathbf{T}}(q_i') = I_{\mathbf{T}}(p_i')$$

so

$$I_{\mathbf{T}}(q_i) + I_{\mathbf{T}}(q_i') = I_{\mathbf{T}}(p_i) + I_{\mathbf{T}}(p_i') = I_{\mathbf{T}}(\mathbf{S}) \tag{4.32}$$

since each surface S_i' is homeomorphic to a sphere. It follows from Equations 4.30, 4.31, and 4.32 that

$$I_{\mathbf{T}}(\mathbf{S}) = I_{\mathbf{T}}(\mathbf{M}) + g(\mathbf{M}) I_{\mathbf{T}}(\mathbf{S})$$

or

$$I_{\mathbf{T}}(\mathbf{M}) = (1 - g(\mathbf{M})) I_{\mathbf{T}}(\mathbf{S})$$

which proves Equation 4.29.

Combining Equation 4.29 with Equation 4.27, we obtain

$$I_{\mathbf{T}}(\mathbf{M}) = 2(1 - g(\mathbf{M}))$$

which is precisely equal to the Euler characteristic of the surface $\mathbf{M}$ (Equation 4.26).

This completes the proof. □

As with vector fields, this rule establishes a connection between the topology of the surface $\mathbf{M}$ (i.e., $\chi(\mathbf{M})$) and the structure of any tensor field tangent to $\mathbf{M}$—i.e., the sum of tensor indices at degenerate points on $\mathbf{M}$.

Corollary 8 *Within the assumptions of Theorem 15, and if the degenerate points of* $\mathbf{T}$ *on* $\mathbf{M}$ *consist of* $\mathcal{W}$ *wedges,* $\mathcal{T}$ *trisectors,* $\mathcal{N}$ *nodes,* $\mathcal{C}$ *centers,* $\mathcal{F}$ *foci,* $\mathcal{S}$ *saddles,* $\mathcal{D}$ *dipoles, ..., then Equation 4.28 implies the topological rule*

$$\frac{1}{2}(\mathcal{W} - \mathcal{T}) + \mathcal{N} + \mathcal{C} + \mathcal{F} - \mathcal{S} + 2\mathcal{D} + \ldots = \chi(\mathbf{M})$$

where the sum in the left-hand side encompasses all the different types of degenerate points of $\mathbf{T}$ on $\mathbf{M}$.

Equation 4.28 considerably restricts the number of admissible surface tensor patterns. For example, Figure 4.33 shows two complex tensor fields—one defined across a torus and another one across a sphere. A topological analysis reveals $\mathcal{N} = \mathcal{C} = \mathcal{F} =$

Figure 4.33: Illustration of the tensor topological rule for a torus and a sphere.

$\mathcal{S} = \mathcal{D} = 0$, $\mathcal{W} = \mathcal{T} = 18$ for the torus, and $\mathcal{N} = \mathcal{C} = 1$, $\mathcal{F} = \mathcal{D} = 0$, $\mathcal{W} = \mathcal{T} = 3$ for the sphere. Both sets of values satisfy Equation 4.28 with $\chi(\textbf{torus}) = 0$ and $\chi(\textbf{sphere}) = 2$, respectively.

Finally, we note that Theorem 15 and Corollary 8 can also be inferred by using results from the topology of line fields (Reference [74], pp. 324-332).

4.6 Extensions to 3-D Symmetric Tensor Fields

In this section, we discuss global icons of 3-D symmetric tensor fields. First, we partly extend the theory of degenerate points to 3-D tensor data (Section 4.6.1). Then, we identify structural loci that characterize globally infinite collections of hyperstreamlines—i.e., both their trajectories and their cross-sections (Section 4.6.2).

4.6.1 Degenerate Points

We extend the theory of degenerate points to 3-D symmetric tensor fields (Equation 1.6). In this case, there are three real eigenvalues, λ_i, and three unit orthogonal eigenvectors, $\vec{e}_i$, $i = 1, 2, 3$, at each point of space. The data are equivalent to three orthogonal eigenvector fields

$$\vec{v}_i(\vec{x}) = \lambda_i(\vec{x})\vec{e}_i(\vec{x})$$

$i = 1, 2, 3$.

Various types of degenerate points $\vec{x}_0$ exist, corresponding to the conditions

$$\lambda_1(\vec{x}_0) = \lambda_2(\vec{x}_0),$$

$$\lambda_2(\vec{x}_0) = \lambda_3(\vec{x}_0),$$

and

$$\lambda_1(\vec{x}_0) = \lambda_2(\vec{x}_0) = \lambda_3(\vec{x}_0),$$

respectively.[14] Consider a degenerate point where two eigenvalues are identical—for example, $\lambda_1(\vec{x}_0) = \lambda_2(\vec{x}_0) > \lambda_3(\vec{x}_0)$. The tensor field is degenerate in the plane

[14] Recall that $\lambda_1(\vec{x}) \geq \lambda_2(\vec{x}) \geq \lambda_3(\vec{x})$ at every point $\vec{x}$.

orthogonal to $\vec{v}_3(\vec{x}_0)$ within which locally two-dimensional patterns such as wedge points, trisectors, and multiple degenerate points can occur. Figure 4.34 represents the tensor field around a wedge point and a trisector in the plane orthogonal to $\vec{v}_3(\vec{x}_0)$. An example of such patterns is given in Figure 4.35, which shows a trisector point deflecting hyperstreamline trajectories in the elastic stress tensor of Figure 3.6. In addition to these simple degenerate points, the whole panoply of multiple degenerate points can occur.

In fact, the patterns in Figure 4.34 should be drawn on a surface normal to the non-degenerate eigenvector field, $\vec{v}_3(\vec{x})$. However, when close enough to $\vec{x}_0$, this surface can be approximated with arbitrary precision by its tangent plane $\mathbf{P}$ at $\vec{x}_0$. (Away from $\vec{x}_0$, trajectories depart from $\mathbf{P}$.)

Techniques discussed in Sections 4.3.3 and 4.3.4 to analyze quantitatively 2-D degenerate points also apply to degenerate points of 3-D symmetric tensor fields. Let $\vec{x}_0$ be a degenerate point of a tensor field $\mathbf{T} = \{T_{ij}\}$, $i, j = 1, 2, 3$. Assume that $\lambda_1(\vec{x}_0) = \lambda_2(\vec{x}_0) \equiv \lambda$ but that $\lambda_3(\vec{x}_0) \neq \lambda$. Let $\mathbf{B}^0 = \{\beta^0_{ij}\}$, $i, j = 1, 2, 3$, be the rotation matrix that brings the third axis of the coordinate system along $\vec{e}_3(\vec{x}_0)$—the unit eigenvector associated to $\lambda_3(\vec{x}_0)$ (Figure 4.34). Transforming $\mathbf{T}$ by the rotation $\mathbf{B}^0 = \{\beta^0_{ij}\}$ leads to new components

$$T'_{ij} = \sum_{p,q=1}^{3} \beta^0_{ip}\beta^0_{jq}T_{pq}$$

At $\vec{x}_0$, $\mathbf{T}'$ is diagonalized—i.e.,

$$\mathbf{T}'(\vec{x}_0) = \{T'_{ij}(\vec{x}_0)\} = \begin{pmatrix} \lambda & 0 & 0 \\ 0 & \lambda & 0 \\ 0 & 0 & \lambda_3 \end{pmatrix}$$

Let $x'_i = \sum_{p=1}^{3} \beta^0_{ip}(x_p - x^0_i)$, $i = 1, 2, 3$, be the new coordinates. $x'_i = 0$ at the location of the degenerate point $\vec{x}_0$. x'_1 and x'_2 run along the plane $\mathbf{P}$ while x'_3 goes in the direction normal to $\mathbf{P}$. This new frame of reference is shown in Figure 4.34, where we translated the origin away from the degenerate point for clarity. The components of $\mathbf{T}'$ in the vicinity of $\vec{x}_0$ can be expanded to first-order terms as

$$T'_{ij}(\vec{x}') \approx T'_{ij}(\vec{x}_0) + \sum_{k=1}^{3} \alpha'_{ijk}x'_k$$

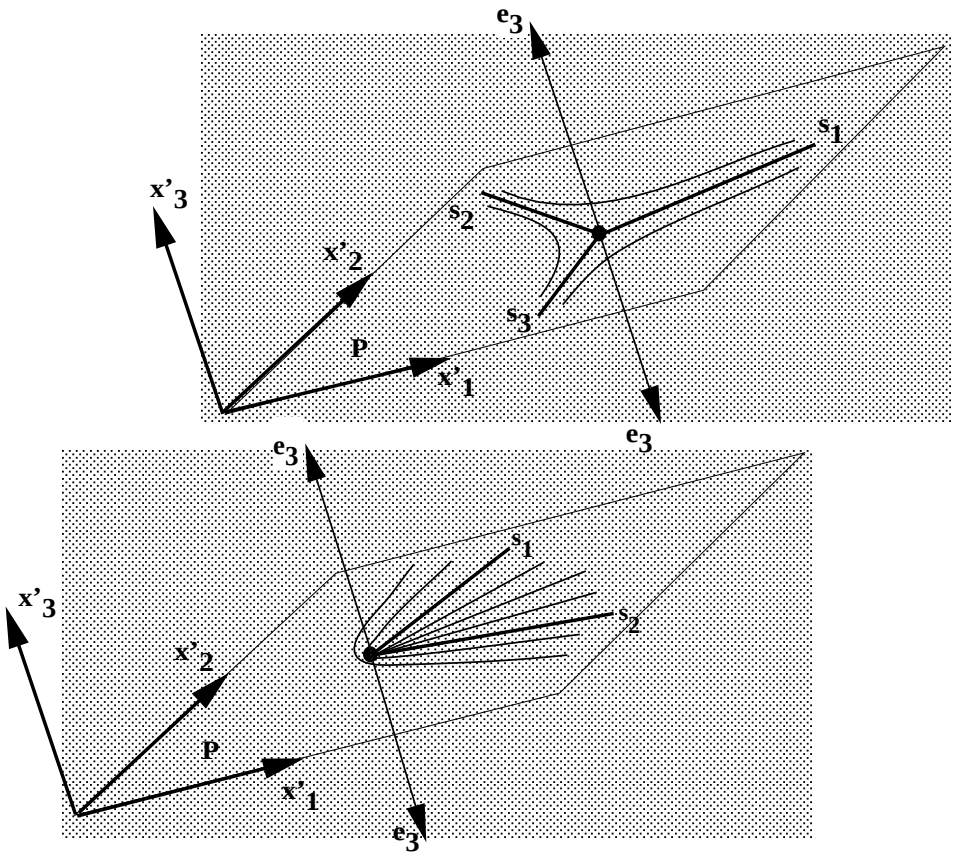

Figure 4.34: Three-dimensional wedge point and trisector around a degenerate point where $\lambda_1 = \lambda_2 > \lambda_3$.

Figure 4.35: A trisector point that deflects minor hyperstreamline trajectories of the elastic stress tensor in Figure 3.6. Color encodes the longitudinal eigenvalue according to color scale 1 in Figure A.3.

with $i, j, k = 1, 2, 3$. The derivatives

$$\alpha'_{ijk} = \frac{\partial T'_{ij}}{\partial x'_k}$$

are computed for $x'_i = 0$. We can analyze tensor patterns in the plane $\mathbf{P}$ (Figure 4.34) by letting $x'_3 \equiv 0$ and considering the 2x2 block

$$\begin{pmatrix} T'_{11} & T'_{12} \\ T'_{12} & T'_{22} \end{pmatrix} = \begin{pmatrix} \lambda + \alpha'_{111}x'_1 + \alpha'_{112}x'_2 & \alpha'_{121}x'_1 + \alpha'_{122}x'_2 \\ \alpha'_{121}x'_1 + \alpha'_{122}x'_2 & \lambda + \alpha'_{221}x'_1 + \alpha'_{222}x'_2 \end{pmatrix}$$

As in Section 4.3.3, the important parameter is the third-order invariant $\delta = a'd' - b'c'$, where $a' = \frac{1}{2}(\alpha'_{111} - \alpha'_{221})$, $b' = \frac{1}{2}(\alpha'_{112} - \alpha'_{222})$, $c' = \alpha'_{121}$, and $d' = \alpha'_{122}$. Trisectors, wedge points, and multiple degenerate points correspond to $\delta < 0$, $\delta > 0$, and $\delta = 0$, respectively.

The former discussion concerns degenerate points where $\lambda_1(\vec{x}_0) = \lambda_2(\vec{x}_0) > \lambda_3(\vec{x}_0)$. The case of degenerate points characterized by $\lambda_1(\vec{x}_0) > \lambda_2(\vec{x}_0) = \lambda_3(\vec{x}_0)$ is similar. However, fully three-dimensional patterns that exist in the vicinity of degenerate points where $\lambda_1(\vec{x}_0) = \lambda_2(\vec{x}_0) = \lambda_3(\vec{x}_0) \equiv \lambda$—such as points of pure pressure in 3-D stress-tensor fields—are yet to be analyzed. In this case $T_{ij}(\vec{x}_0) = \lambda\delta_{ij}$, $i, j = 1, 2, 3$, so we can locate these degenerate points by solving five simultaneous equations:

$$\begin{cases} T_{11}(\vec{x}_0) - T_{22}(\vec{x}_0) = 0 \\ T_{22}(\vec{x}_0) - T_{33}(\vec{x}_0) = 0 \\ T_{12}(\vec{x}_0) = 0 \\ T_{13}(\vec{x}_0) = 0 \\ T_{23}(\vec{x}_0) = 0 \end{cases} \tag{4.33}$$

Hyperstreamline patterns that arise in the vicinity of $\vec{x}_0$ are, therefore, characterized by gradients of five scalar functions.

4.6.2 Topological Loci

As discussed in Chapter 3, we can interpret 3-D symmetric tensor fields as three infinite collections of hyperstreamlines, one along each eigenvector field. Each hyperstreamline is characterized by its trajectory, color, and cross-section.

In order to project such mental images on a computer screen, we must solve complex problems related to visual clutter. Displaying intelligibly more than a few hyperstreamlines is not simple, and representing directly an infinite number of such hyperstreamlines is a fortiori beyond reach. We can represent indirectly, however, the collective behavior of a large number of hyperstreamlines. That is, we can display various topological loci that unambiguously characterize an infinite set of hyperstreamlines without actually drawing them. Many conclusions about the behavior of hidden or undrawn hyperstreamlines can be inferred by learning to interpret these loci.

Consider the collection $\mathcal{HS}_l$ of hyperstreamlines propagating along the longitudinal eigenvector field $\vec{v}_l$ corresponding to the eigenvalue λ_l. Let us denote the two transverse eigenvalues by λ_{t_1} and λ_{t_2}, respectively. Important features exist in both the trajectory and the cross-section of the hyperstreamlines belonging to $\mathcal{HS}_l$.

The locus

$$(\lambda_l - \lambda_{t_1})(\lambda_l - \lambda_{t_2}) = 0 \tag{4.34}$$

is the set of degenerate points that deflect, attract, or terminate hyperstreamline trajectories in $\mathcal{HS}_l$. This set includes both degenerate points where two eigenvalues are equal to each other and degenerate points where all three eigenvalues are identical. The representation of the locus in Equation 4.34 partly elucidates the global behavior of trajectories in $\mathcal{HS}_l$; at points outside this locus, hyperstreamline trajectories behave as if the tensor field were topologically uniform.

Equation 4.34 is formally important, but in practice it is easier to locate degenerate points by directly considering tensor components rather than eigenvalues. (See for example Equations 4.3 or 4.33.[15]) The reason is that computing zeros of functions of tensor components is much easier than computing extrema of functions of eigenvalues.[16]

[15]Equations 4.3 apply to degenerate points of 2-D symmetric tensor fields only. For 3-D symmetric tensor fields, more complex equations involving tensor coefficients have to be solved in order to locate degenerate points where two eigenvalues are degenerate.

[16]Zeros of Equation 4.34 are also extrema because of the specific ordering $\lambda_1 \geq \lambda_2 \geq \lambda_3$ of the eigenvalues.

Other topological loci characterize the cross-sections of hyperstreamlines belonging to $\mathcal{HS}_l$. For example, at points where the product of the transverse eigenvalues vanish—i.e., points where

$$\lambda_{t_1}\lambda_{t_2} = 0 \tag{4.35}$$

cross-sections of hyperstreamlines in $\mathcal{HS}_l$ are singular; they are reduced to straight lines or even points. More generally, loci where the eccentricity of the cross-sections

$$\epsilon = \sqrt{1 - \frac{\min^2(|\lambda_{t_1}|, |\lambda_{t_2}|)}{\max^2(|\lambda_{t_1}|, |\lambda_{t_2}|)}}$$

is constant are sets of points where the cross-sections of hyperstreamlines in $\mathcal{HS}_l$ have the same shape, regardless of their orientation and scaling. In particular, the locus

$$\lambda_{t_1} \pm \lambda_{t_2} = 0$$

is the set of points where cross-sections degenerate into a circle ($\epsilon = 0$).

Elastic Stress Tensor Induced by Two Compressive Forces

Figure 4.36 shows topological loci for the stress tensor depicted in Figure 3.6 (elastic stress tensor induced by two compressive forces). Yellow and green surfaces are loci of points where medium eigenvalue λ_2 and major eigenvalue λ_1 vanish, respectively. The two surfaces taken together correspond to the locus in Equation 4.35. On both surfaces, the cross-sections of minor tubes (four of them are shown) reduce to straight lines. On the blue surface $\lambda_1 - \lambda_2 = 0$, transverse eigenvalues are opposite to each other and minor tubes' cross-sections are circular. Below the yellow surface, both transverse eigenvalues are positive; all transverse directions in the tubes' cross-sections are in tension. Above the yellow surface, the medium eigenvalue is negative; some transverse directions are in tension while others are compressive. Inside the green surface, however, both transverse eigenvalues are negative, and all transverse directions are in compression.

Stress and Viscous-Stress Tensors in Fluid Flows

Another example of structural depiction is given for the stress tensor σ_{ik} and the viscous-stress tensor σ'_{ik} in fluid flows. As shown in Table 1.2, these two tensors differ

Figure 4.36: Topological loci of the elastic stress tensor in Figure 3.6.

only by an isotropic pressure component, implying that the unit eigenvectors of both tensor fields are identical. However, eigenvalues of σ_{ik} are equal to eigenvalues of σ'_{ik} minus a large pressure component. Table 1.2 also shows that visualizing σ'_{ik} is equivalent to visualizing the rate-of-strain tensor ϵ_{ik} in incompressible flows.

Hyperstreamlines of the stress tensor in the flow past a hemisphere cylinder are shown in Figure 4.37 (the flow is the same as in Figure 3.8). The major tubes in front propagate along the least compressive direction, $\vec{v}_1$. Their trajectory shows how forces propagate from the region in front of the cylinder to the surface of the body. The cross-sections of the tubes are circular, indicating as expected that the pressure component of the stresses is dominant. However, viscous stresses close to the body induce slightly anisotropic cross-sections. For example, eccentricity on the yellow surface is equal to 10%.

The helices lie along the medium eigenvector field, $\vec{v}_2$. While propagating, they remain mostly parallel to the cylinder's surface, and the orientation of their arms indicate a fairly constant direction of the two transverse eigenvectors—the most and least compressive eigendirections, respectively. The third helix exhibits a more complex behavior, suggesting that the stress tensor is less uniform in the region of contact between the tubes and the body than in other parts of the flow.

Figure 4.38 shows the viscous-stress tensor σ'_{ik} in the same flow. As expected, trajectories are similar to those in Figure 4.37, but removing the large, isotropic pressure contribution, dramatically enhances the anisotropy of the tubes' cross-sections. The surface shown corresponds to a constant eccentricity of 90%; it is crossed twice by each tube.

4.7 Chapter Summary

In this chapter, we define the topology of symmetric, second-order tensor fields as the topology of their eigenvector fields. We extract topological skeletons based on degenerate points, the set of their connecting separatrices, and limit cycles—thereby broadening concepts developed in differential equations and dynamical systems to cover the visualization of second-order tensor fields. We study in detail the topology

Figure 4.37: Stress tensor in the flow past a hemisphere cylinder. Color scale 1 of Figure A.3 is used.

Figure 4.38: Viscous-stress tensor in the flow past a hemisphere cylinder. Color scale 1 of Figure A.3 is used.

of 2-D symmetric tensor fields, and we partially extend results to 3-D symmetric tensor data.

Degenerate points are points where at least two eigenvalues are equal to each other. They are basic topological elements playing a similar role as critical points in vector fields. Indeed, hyperstreamline trajectories never cross each other except at degenerate points, in the vicinity of which we singled out three types of sectors—hyperbolic, elliptic, and parabolic. Degenerate points deflect hyperstreamlines adjacent in their hyperbolic sectors and terminate hyperstreamlines approaching from within their parabolic sectors. At a degenerate point, the two eigenvector fields have in general a different number of sectors of each type, but they have the same number of elliptic sectors in excess to the number of hyperbolic sectors.

We introduce the concept of a "tensor index," a quantity that is fundamental to the topology of 2-D symmetric tensor fields. The tensor index of a Jordan curve is a line integral of tensor components equal to the number of counterclockwise revolutions undergone by the eigenvectors during one counterclockwise revolution along the curve. Due to the eigenvectors' sign indeterminacy, tensor indices are integer or half-integer quantities. The tensor index at a degenerate point $\vec{x}_0$ is the index of Jordan curves encompassing $\vec{x}_0$ but no other degenerate point. There is a correspondence between tensor index and number of hyperbolic and elliptic sectors at a degenerate point. If a Jordan curve encompasses more than one degenerate point, the curve's index is the sum of tensor indices at enclosed degenerate points. In particular, the tensor index of a hyperstreamline cycle is equal to unity.

We classify degenerate points as a function of a parameter δ, an invariant of third-order tensor fields. δ is a function of tensor gradients at the degenerate point position. Simple degenerate points correspond to values of $\delta \neq 0$ and multiple degenerate points fall in the category $\delta = 0$. There are two types of simple degenerate points—trisectors and wedge points corresponding to $\delta < 0$ and $\delta > 0$, respectively. Neither of them has elliptic sectors. Trisector points have a tensor index equal to $-\frac{1}{2}$, three hyperbolic sectors per eigenvector field, and no parabolic sector. Likewise, wedge points have an index equal to $\frac{1}{2}$, one hyperbolic sector, and one or zero parabolic sector per eigenvector field. We conceptualize multiple degenerate points as arising from the

merging of simple degenerate points. There is a large and diverse panoply of multiple degenerate points among which we identify star-nodes, centers, foci, saddle points, cusps, saddle-nodes, and dipoles. In general, multiple degenerate points are built from the juxtaposition of any number of hyperbolic, elliptic, and parabolic sectors.

Together with degenerate points, separatrices are basic topological elements of 2-D tensor fields. These hyperstreamline trajectories separate the domain into regions where the tensor field is topologically equivalent to uniform data. We identify two types of separatrices: limit cycles and hyperstreamlines that emanate from degenerate points and that lie on the boundary of hyperbolic sectors. We prove that simple limit cycles do not exist in solenoidal tensor fields. Also, trisector points have three separatrices per eigenvector field while wedge points have one or zero separatrix per eigenvector field. Likewise, multiple degenerate points have at most $2(m+2)$ separatrices for the two eigenvector fields combined, m being the lowest degree of non-vanishing terms in Taylor expansions of tensor components around the degenerate point.

We generalize the Poincaré-Hopf theorem to analyze tensor fields tangent to 2-D surfaces, by proving that the sum of tensor indices at degenerate points of such tensor fields depends only on the topology of the surface and not on the tensor field. More precisely, the sum of tensor indices at degenerate points is equal to the surface's Euler characteristic. This topological rule makes explicit the way the topology of the surface affects the topology of any tangent tensor field.

Finally, we discuss 3-D symmetric tensor fields. In this case, a topological depiction represents schematically the global behavior of an infinite collection of hyperstreamlines. Basic topological elements include degenerate points and other topological loci.

Similar to the two-dimensional case, degenerate points of 3-D tensor fields deflect or terminate hyperstreamline trajectories. 3-D degenerate points fall within two categories, those where two eigenvalues are equal to each other and those where all three eigenvalues are identical. The former are characterized by patterns similar to 2-D simple and multiple degenerate points but lying in a plane orthogonal to the eigenvector associated to the non-degenerate eigenvalue. The latter are more complex because

local hyperstreamline patterns depend on the gradients of five scalar functions.

In addition to 3-D degenerate points, we extract various topological loci that carry global information about hyperstreamlines' cross-sections. These sets of points include loci of constant eccentricity, and loci where cross-sections are reduced to points, lines, or circles.

Chapter 5

Conclusions and Future Research

In the introduction of this dissertation, we stated our main objectives as eliciting the geometric structure of second-order tensor fields and laying a framework for their visualization. In this final chapter, we recapitulate the steps that we follow towards fulfilling these objectives. We also identify areas that are open for future research.

5.1 A Look Back ...

We study the geometric structure of symmetric tensor fields, designing at each step appropriate icons for their visualization. We also provide suggestions for extending these ideas to asymmetric tensor data. Tables 5.1 and 5.2 reproduce what was presented earlier (Tables 1.3 and 1.4 of Chapter 1, respectively). The italicized items in Table 5.2 map our contributions to the visualization of tensor fields according to the framework given in the introduction.

This framework is relevant to the visualization of continuous, multivariate data. A particularly important concept is the information level embedded in icons which we characterize as elementary, local, or global. This framework emphasizes the similarities of the problems encountered when visualizing continuous vector and tensor fields. The difficulty of representing these data stems from the necessity of rendering the underlying continuity while avoiding problems related to visual clutter.

For vector fields, we can emphasize the continuity by displaying streamlines and

Spatial Domain	Embedded Information		
	Elementary	Local	Global
Point	arrows wedges hedgehogs	critical-point glyphs	
Line	streamlines streaklines particle traces	streamribbons streamtubes	vortex cores
Surface	streamsurfaces	⋆	2-D vector topology ⋆
Volume			skin-friction topology and separation surface, helicity density (c), or vortex cores ⋆

Table 5.1: Vector icons. (c) means object contraction. The stars indicate promising research areas.

Spatial Domain	Embedded Information		
	Elementary	Local	Global
Point	ellipsoids tensor glyphs	*degenerate points* ⋆	
Line	trajectories (c) *hyperstreamlines*	⋆	
Surface	⋆	⋆	*2-D tensor topology* ⋆
Volume			*3-D topological loci* ⋆

Table 5.2: Tensor icons. (c) means object contraction. Italicized items show the contributions of this dissertation. The stars indicate promising research areas.

streamsurfaces rather than arrows. We can also represent the global structure of the data by extracting the vector-field topology—a set of carefully chosen points (critical points) and lines (separatrices) that schematically encode the behavior of a continuous distribution of (undrawn) streamlines.

We design similar icons for symmetric tensor fields, seeking continuous representations that avoid coarsely-spaced point icons. We show that n-dimensional tensor fields are equivalent to n orthogonal families of smooth and continuous curves tangent to the eigenvector fields (hyperstreamline trajectories). These trajectories never intersect each other except at points where the eigenvalues are equal to each other (degenerate points). In two dimensions ($n = 2$), we generate textures to render hyperstreamline trajectories. In three dimensions ($n = 3$), we use numerical integration. We then surround the resulting trajectories by tubular surfaces (hyperstreamlines) that represent the transverse eigenvectors. We define solenoidal tensor fields by analogy with solenoidal vector fields, and we show the similarity of the geometric properties of hyperstreamlines in solenoidal tensor fields and streamlines in solenoidal vector fields. Theorems 1, 2, and 13 summarize these properties.

Hyperstreamlines represent, better than point icons, the underlying continuity of tensor fields. However, they merely sample the data along their trajectories. In general, many hyperstreamlines are required for understanding the global structure of tensor fields without ambiguity. This creates overly cluttered images. To remedy this, we define and analyze the topology of tensor fields. As with vector fields, we derive a set of points and trajectories that embed global information, representing schematically the collective behavior of a continuous distribution of (undrawn) hyperstreamlines. By extracting the geometric structure of tensor data, we produce simple and austere depictions that allow observers to infer the behavior of any hyperstreamlines in the field.

The points that underlie the topology of tensor fields are the degenerate points—points where the eigenvalues are equal to each other. Depending on the tensor gradients, degenerate points can be of various types that correspond to different local patterns of the eigenvectors. We define a parameter δ, a third-order tensor invariant

that is function of the tensor gradients and that characterizes the nature of degenerate points. (Likewise, second-order tensor invariants determine the nature of critical points in vector fields.) When $\delta \neq 0$, degenerate points are simple; they are either wedge points ($\delta > 0$) or trisector points ($\delta < 0$) (Theorem 11). When $\delta = 0$, degenerate points are multiple; among these points we identify nodes, foci, saddle points, dipoles, cusps, saddle-nodes, as well as other, more exotic patterns (Theorem 12).

The other elements that underlie the topology of tensor fields are the separatrices, which designate either the limit cycles, or the trajectories that emanate from the degenerate points and lie on the border of hyperbolic sectors. We prove that solenoidal tensor fields do not posses simple limit cycles (Theorem 13), and we develop an algorithm to extract the topology of symmetric tensor fields.

When a tensor field is defined across a surface, there is a connection between the topology of the surface and the topology of the tensor field. We transpose to tensor fields a theorem by Poincaré for vector fields: Theorem 15 establishes how the surface geometry constrains the number and the nature of the degenerate points that lie on the surface.

5.2 ...and a Look Ahead

Our study generates new questions to be addressed in the future, including the 3-D extensions of tensor field topology, and the techniques for the automatic comparison of tensor topological skeletons. More specifically, we can identify three broad categories of research issues: visual, physical, and mathematical.

5.2.1 Visual Issues

The empty boxes in Tables 5.1 and 5.2 suggest new areas for visualization research. Some of these boxes cannot be filled, but others call for new icons to be designed. The stars indicate areas that offer especially rich prospects for new developments. Namely,

- Global icons of vector and tensor fields. The general, topological approaches that were discussed in previous chapters may be enhanced by computing more specific, problem-dependent data features that carry global information.

- Local icons of tensor fields. In particular, how are we to design degenerate-point glyphs that show tensor gradients around degenerate points, similar to the way critical-point glyphs show vector gradients around critical points? (See Figure 2.7.)

- Elementary surface icons of tensor fields. Surface icons can help to improve the perception of complex eigenvector patterns in 3-D tensor data sets. (See Figure 2.13 for vector fields.) Two types of surfaces are possible: surfaces that are tangent to one eigenvector field and orthogonal to the two other eigenvector fields; and surfaces that are tangent to two eigenvector fields and orthogonal to the third eigenvector field. Degenerate points are appropriate places to start the integration of both types of surfaces.

- Local surface icons of vector fields—such as streamsurfaces that display, in addition to elementary information, aspects of the vector field gradients.

Filling up these boxes with new icons will provide researchers with a broad range of tools to visualize vector and symmetric tensor data sets. In addition, one can combine the decompositions of Section 3.5 with the results of Chapter 4 to explore the topology of asymmetric tensor fields.

5.2.2 Physical Issues

Our general methodology for visualizing tensor data and for extracting topological structures must be tailored to more specific problems in fluid mechanics, mechanical engineering, relativity, etc. We hope that new insights will be gained by visualizing tensor data and by correlating them with vector and scalar fields. In addition, the two following questions should be investigated: Can specific physical constraints restrict the variety of admissible patterns around degenerate points? And do degenerate

points, as well as the associated local eigenvector patterns, possess physical meanings beyond that of isotropy? (That is, degenerate eigenvalues.)

5.2.3 Mathematical Issues

Some mathematical and algorithmic questions are yet to be answered.

- Multiple degenerate points. We analyzed multiple degenerate points where the Taylor expansions of tensor components start with polynomials of the same degree (Equation 4.24). Multiple degenerate points with polynomial expansions of arbitrary degree—i.e., $m_p \neq m_q$ in Equation 4.10—remain to be studied.

- Separatrices of multiple degenerate points. It would be useful to establish a mathematical criterion that identifies which roots of Equation 4.33 define separatrices (i.e., roots that lie on the border of a hyperbolic sector), and which roots are mere radial directions. This would also simplify the topological analysis of conventional, signed vector fields.

- 3-D degenerate points. The local patterns around 3-D degenerate points with three identical eigenvalues (Equation 4.33) remain to be characterized.

- Limit cycles. Is it possible to design algorithms for automatically detecting limit cycles? (See Section 4.3.5.) This is also a research issue for the visualization of vector fields.

- Topological transitions. Can we automatically compare topological skeletons of tensor fields, perhaps using graph theoretic approaches? (See Reference [75].) This is also a research issue for the visualization of vector fields.

By designing visualization mappings of second-order tensor fields and by elucidating their topological structure, this dissertation demonstrates the potential of scientific visualization for building new knowledge beyond the usual goal of inspecting results from experiments and computations. It is our hope that our analysis will serve as a

model to tackle the visualization of other multivariate, continuous data. Furthermore, we wish that our general methodology will be augmented as it is applied to more specific cases, thereby generating new ideas that will further expand the growing field of scientific visualization.

Appendix A

Smooth Hue Scale

This appendix describes our design of a color scale for encoding univariate variables. This is an important topic, but we discuss it in appendix because it is a by-product of our main research focus on tensor field visualization.

We seek a smooth color scale—a color scale that translates equal changes in the underlying variable into equally perceived color differences. This amounts to choosing a color path, a trajectory in uniform color space which we uniformly sample so as to yield the color scale. We use as color space the CIE 1976 $L^*u^*v^*$ space, which is approximately uniform across a wide range of colors (Reference [76]). In this space, the perceived difference between two colors separated by small increments $(\Delta L^*, \Delta u^*, \Delta v^*)$ is equal to Euclidean distance. That is,

$$\text{Perceived Color Difference} \approx \sqrt{(\Delta L^*)^2 + (\Delta u^*)^2 + (\Delta v^*)^2}$$

(Formulae relating color coordinates in $L^*u^*v^*$ space to the CIE 1931 $\{X, Y, Z\}$ tristimulus values are given in Reference [76].)

We seek a color path that fulfills the following three requirements as well as possible:

1. A uniform color scale is obtained by uniformly sampling the color path.

2. Hue undergoes significant and monotonic variations along the color path; other color dimensions, such as saturation and lightness, experience only relatively small variations.

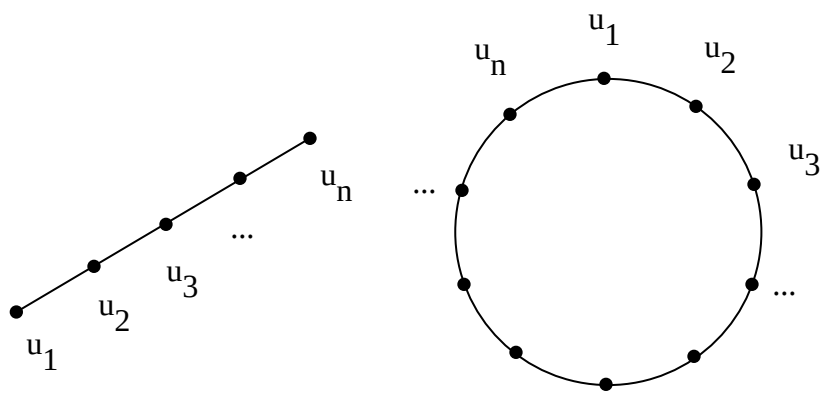

Figure A.1: A line segment and a circle as color paths.

3. The length of the color path in $L^*u^*v^*$ space is as large as possible, so as to maximize the number of Just Noticeable Differences (JND) along the scale.

The uniformly sampled line segment shown in Figure A.1 (left) is the most attractive color path which satisfies requirement 1. Indeed, let

$$d_m(k) = |u_{k+m} - u_k| \tag{A.1}$$

be the perceived color difference between samples u_k and u_{k+m}. There are two main reasons why a uniformly sampled line segment is appealing: uniformity and additivity. For m small, $d_m(k)$ is constant when k runs along the path. This ensures uniformity of the color scale. Perceived color differences along a line segment are also additive. That is,

$$d_{m+n}(k) = d_m(k) + d_n(k+m) \tag{A.2}$$

for every k and for small values of m and n. Both these properties make uniformly sampled line segments attractive color paths. However, because hue is typically a circular component of color, it does not undergo large variations along linear paths (unless saturation also varies significantly, which clearly violates requirement 2).

Because of this, a better topology for color paths is the uniformly sampled circle represented in Figure A.1 (right). Again, perceived color differences $d_m(k)$ (Equation A.1) are constant along the path for m small, and the resulting color scale is

uniform. However, color differences are no longer additive (Equation A.2). Choosing a uniformly sampled circle rather than a line segment, therefore, amounts to sacrifice the scale additivity for a wider dynamic range.

The number of JNDs in a color scale is approximately proportional to the length of the associated color path in $L^*u^*v^*$ space. Requirement 3 then calls for maximizing the circle radius. By trial and error, we selected the optimal circle represented in Figure A.2. Uniformity is ensured by allowing small variations of saturation and lightness along the circle. (The other curves in Figure A.2 are paths of constant saturation and lightness. Clearly, their topology does not permit constant distances $d_m(k)$.) The circle lies within a plane of normal

$$\begin{cases} n_{L^*} = 0.9685 \\ n_{u^*} = 0.1453 \\ n_{v^*} = -0.0969 \end{cases}$$

The center of the circle is located at the point

$$\begin{cases} L^* = 73.0 \\ u^* = 25.0 \\ v^* = 16.0 \end{cases}$$

and the radius is

$$R = 86.0$$

The perimeter of the circle is $2\pi R = 540$, so the resulting color scale contains as many as 5.4 times more JNDs than a gray scale does.

In practice, we do not sample the circle along a full perimeter because of the circular character of hue. Figure A.3 shows the result obtained by uniformly sampling parts of the circle in Figure A.2. Color scales 1 and 2 contain 4.93 and 3.42 as many JNDs as a gray scale, respectively. They present the best uniformity that can be reached without accounting for the imperfections of the $L^*u^*v^*$ space itself—especially in corners away from the L^* axis.[1]

[1] The scale uniformity is unfortunately difficult to render in prints.

Figure A.2: Color path in CIE 1976 $L^*u^*v^*$ color space.

Figure A.3: Smooth color scale for encoding univariate variables.

Our experience with color scales teaches us that our hue scale is more uniform than other widely used color scales, such as the LOCS scale (Reference [77]) or the color scale in NASA's FAST visualization package (Reference [78]).

Appendix B

Locating Simple Degenerate Points

In this appendix, we discuss the technique used in locating simple degenerate points. We seek the simple roots $\vec{x}_0$ of the system of equations

$$\begin{cases} T_{11}(\vec{x}_0) - T_{22}(\vec{x}_0) = 0 \\ T_{12}(\vec{x}_0) = 0 \end{cases} \qquad \text{(Equations 4.3)}$$

when tensor components T_{ij} are defined on a regular grid. The algorithm processes each grid cell in turn for each time step so we detail below operations specific to a generic grid cell.

Consider the grid cell shown in Figure B.1. For expediency, we first determine if the cell is likely to contain simple degenerate points, or not. Only if the former is the case, do we seek solutions to Equations 4.3 within the cell.

Let $f_{i,j}$ and $g_{i,j}$ be the values of $T_{11} - T_{22}$ and T_{12} at the vertex (i, j), and let f_{min} and f_{max} be the minimum and maximum values of $f_{i,j}$, $f_{i+1,j}$, $f_{i,j+1}$, and $f_{i+1,j+1}$, respectively. Accordingly, let g_{min} and g_{max} be the minimum and maximum values of

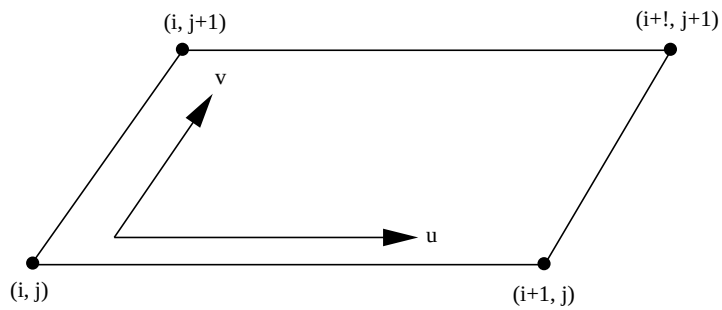

Figure B.1: A grid cell.

$g_{i,j}$, $g_{i+1,j}$, $g_{i,j+1}$, and $g_{i+1,j+1}$. If one of the six conditions

$$\begin{cases} f_{min} \leq 0 \\ f_{max} \geq 0 \\ g_{min} \leq 0 \\ g_{max} \geq 0 \\ |f_{min}| + |f_{max}| > 0 \\ |g_{min}| + |g_{max}| > 0 \end{cases}$$

is not met, that means that the cell does not contain simple degenerate points, or that the tensor field is uniformly zero across the cell. In both cases, we do not process the cell further.

If all six conditions are met, we use bilinear interpolation to approximate tensor components within the cell as

$$\begin{cases} f \approx f_{i,j} + u(f_{i+1,j} - f_{i,j}) + v(f_{i,j+1} - f_{i,j}) + uv(f_{i+1,j+1} - f_{i,j+1} - f_{i+1,j} + f_{ij}) \\ g \approx g_{i,j} + u(g_{i+1,j} - g_{i,j}) + v(g_{i,j+1} - g_{i,j}) + uv(g_{i+1,j+1} - g_{i,j+1} - g_{i+1,j} + g_{ij}) \end{cases}$$

where $0 \leq u, v \leq 1$ (Figure B.1). We find degenerate points within the cell by seeking solutions of the system

$$\begin{cases} f = 0 \\ g = 0 \end{cases}$$

which can lead up to two solutions, (u_1, v_1) and (u_2, v_2), or to a linear family of solutions

$$\alpha u + \beta v + \gamma = 0 \tag{B.1}$$

We must reject solutions located outside the cell (u or v outside the range $[0, 1]$) as well as solutions such as Equation B.1, which indicate a line of degenerate points rather than isolated degenerate points.

Appendix C

Related Publications

The work presented in this dissertation has appeared or will appear in several publications; this appendix contains a brief overview of the relevant articles.

- Thierry Delmarcelle and Lambertus Hesselink, "Visualization of Second-Order Tensor Fields and Matrix Data," in *Proc. IEEE Visualization '92,* pp. 316-323, CS Press, Los Alamitos, CA., October 1992.

  Awarded Visualization '92 Conference Best Paper. This paper introduces the concept of hyperstreamlines and topological loci of 3-D symmetric tensor fields.

- Thierry Delmarcelle and Lambertus Hesselink, "Visualizing Second-Order Tensor Fields with Hyperstreamlines," *IEEE Computer Graphics and Applications,* vol. 13, no. 4, pp. 25-33, July 1993. Special issue on scientific visualization.

  Awarded IEEE Computer Graphics and Applications Best 1993 Paper. This invited paper discusses, in addition to hyperstreamlines and topological loci, solenoidal tensor fields, color-coding schemes, and icons for 3-D unsymmetric data.

- Thierry Delmarcelle and Lambertus Hesselink, "A Unified Framework for Flow Visualization," in *Computer Visualization* (R. Gallagher Ed.), Chapter 5, CRC Press, 1994.

  Invited Book Chapter. This chapter lays out the unified framework for scientific visualization that we discussed in the introduction of the thesis. It provides the

first comprehensive review of both vector and tensor visualization techniques.

- Lambertus Hesselink and Thierry Delmarcelle, "Visualization of Vector and Tensor Data Sets," in *Scientific Visualization. Advances and Challenges* (L. Rosenblum Ed.), Chapter 26, pp. 419-433, Academic Press, San Diego, 1994.

  This paper discusses further the unified framework for vector and tensor field visualization.

- Thierry Delmarcelle and Lambertus Hesselink, "The Topology of Symmetric, Second-Order Tensor Fields," in *Proc. IEEE Visualization '94,* pp. 140-147, CS Press, Los Alamitos, CA., 1994.

  Awarded Visualization '94 Conference Best Paper. This paper introduces the concept of tensor field topology, degenerate points, hyperbolic and parabolic sectors, and hyperstreamline separatrices. The tensor topological rule is discussed.

Bibliography

,

[1] E. R. Tufte, *The Visual Display of Quantitative Information.* Graphics Press, Box 430, Cheshire, Connecticut 06410, 1983.

[2] E. A. Abbott, *Flatland: A Romance in Many Dimensions.* Barnes & Noble, New York, 5 ed., 1963.

[3] H. Chernoff, "The use of faces to represent points in k-dimensional space graphically," *Journal of the American Statistical Association*, vol. 68, pp. 361–368, June 1973.

[4] E. R. Tufte, *Envisionning Information.* Graphics Press, Box 430, Cheshire, Connecticut 06410, 1990.

[5] J. Bertin, *Semiology of Graphics.* The University of Wisconsin Press, 1983. Translation of *Sémiologie Graphique*, Editions Gauthier-Villars, Paris, 1967.

[6] J. Bertin, *Graphics and Graphic Information Processing.* Walter de Gruyter, 1981. Translation of *La Graphique et le Traitement Graphique de l' Information*, Flammarion, Paris, 1977.

[7] B. H. McCormick, T. A. DeFanti, and M. D. Brown, "Visualization in scientific computing: a synopsis," *IEEE Computer Graphics and Applications*, vol. 7, no. 4, pp. 61–70, 1987.

[8] W. E. Lorensen and H. E. Cline, "Marching cubes: A high resolution 3-D surface construction algorithm," *Computer Graphics*, vol. 21, no. 4, pp. 163–169, 1987.

[9] S. M. Jaffey, K. Dutta, and L. Hesselink, "Digital reconstruction methods for three-dimensional image visualization," in *Processing and Display of Three-Dimensional Data II (Proc. SPIE)*, vol. 507, pp. 155–165, SPIE, Bellingham, WA., 1984.

[10] M. Levoy, "Display of surfaces from volume data," *IEEE Computer Graphics and Applications*, vol. 8, no. 3, pp. 29–37, 1988.

[11] R. A. Drebin, L. Carpenter, and P. Hanrahan, "Volume rendering," *Computer Graphics*, vol. 22, no. 4, pp. 110–119, 1988.

[12] R. B. Haber, "Visualization techniques for engineering mechanics," *Computing Systems in Engineering*, vol. 1, no. 1, pp. 37–50, 1990.

[13] R. B. Haber and D. A. McNabb, "Visualization idioms: a conceptual model for scientific visualization systems," in *Visualization in Scientific Computing* (G. M. Nielson and B. Shriver, eds.), pp. 74–93, CS Press, Los Alamitos, CA., 1990.

[14] G. M. Nielson, "Visualization in scientific computing," *IEEE Computer*, vol. 22, no. 8, pp. 10–11, 1989. Guest editor's introduction to a special issue on Scientific Visualization.

[15] E. J. Farrell, "Preface to a special issue on visual interpretation of complex data," *IBM Journal of Research and Development*, vol. 35, no. 1, p. 3, 1991.

[16] L. J. Rosenblum and G. M. Nielson, "Visualization comes of age," *IEEE Computer Graphics & Applications*, vol. 11, no. 3, pp. 15–17, 1991. Guest editor's introduction to a special issue on Scientific Visualization.

[17] B. S. Baldwin and H. Lomax, "Thin layer approximation and algebraic model for separated turbulent flows," in *AIAA 16th Aerospace Sciences Conference*, Jan. 1978. AIAA Paper 78-257.

[18] R. D. Bergeron and G. G. Grinstein, "A reference model for the visualization of multi-dimensional data," in *EUROGRAPHICS '89* (W. Hansmann, F. Hopgood,

and W. Strasser, eds.), pp. 393–399, Elsevier Science Publishers B.V. (North-Holland), 1989.

[19] G. D. Kerlick, "Moving iconic objects in scientific visualization," in *Proc. IEEE Visualization '90*, pp. 124–130, CS Press, Los Alamitos, CA., 1990.

[20] C. S. Peirce, *Philosophical Writings of Peirce, selected and edited with an introduction by Julius Buchtler.* Dover Publications, New York, 1955.

[21] V. Tejera, *Semiotics from Peirce to Barthes: a conceptual introduction to the study of communication, interpretation, and expression.* E. J. Brill, Leiden, The Netherlands, 1988.

[22] P. K. Robertson, "A methodology for choosing data representations," *IEEE Computer Graphics and Applications*, vol. 11, no. 3, pp. 56–67, 1991. Special issue on visualization.

[23] B. Cabral and L. C. Leedom, "Imaging vector fields using line integral convolution," *Computer Graphics (SIGGRAPH'93 Proceedings)*, vol. 27, pp. 263–272, 1993.

[24] J. J. van Wijk, "Spot noise. Texture synthesis for data visualization," *Computer Graphics*, vol. 25, no. 4, pp. 309–318, 1991.

[25] M. Hetenyi, *Handbook of Experimental Stress Analysis.* John Wiley & Sons, New York, 1950.

[26] R. R. Dickinson, "A unified approach to the design of visualization software for the analysis of field problems," in *3D Visualization and Display Technologies (Proc. SPIE)*, vol. 1083, pp. 173–180, SPIE, Bellingham, WA., 1989.

[27] W. Merzkirch, *Flow Visualization.* Academic Press, London, second ed., 1987.

[28] K. A. Kroos, "Computer graphics techniques for three-dimensional flow visualization," in *Frontiers in Computer Graphics (Proc. Computer Graphics Tokyo'84)* (T. L. Kunii, ed.), Springer-Verlag, 1985.

[29] G. D. Kerlick, "Isolev: a level surface cutting plane program for fluid flow data," in *Extracting Meaning from Complex Data: Processing, Display, Interaction (Proc. SPIE)*, vol. 1259, pp. 2–13, SPIE, Bellingham, WA., 1990.

[30] L. Yaeger, C. Upson, and R. Myers, "Combining physical and visual simulation - creation of the planet jupiter for the film '2010'," *Computer Graphics*, vol. 20, no. 4, pp. 85–93, 1986.

[31] C. Upson, R. Wolff, R. Weinberg, and D. Kerlick, *Two and Three Dimensional Visualization Workshop.* ACM SIGGRAPH, 1989. SIGGRAPH 1989 course notes # 13.

[32] G. K. Batchelor, "The effect of homogeneous turbulence on material lines and surfaces," *Proceedings of the Royal Society of London Ser. A*, vol. 213, pp. 349–366, 1952.

[33] P. G. Buning, "Sources of error in the graphical analysis of CFD results," *Journal of Scientific Computing*, vol. 3, no. 2, pp. 149–164, 1988.

[34] P. Yeung and S. Pope, "An algorithm for tracking fluid particles in numerical simulations of homogeneous turbulence," *Journal of Computational Physics*, vol. 79, pp. 373–416, 1988.

[35] S. E. Rogers, P. G. Buning, and F. J. Merritt, "Distributed interactive graphics. Applications in computational fluid dynamics," *The International Journal of Supercomputer Applications*, vol. 1, no. 4, pp. 96–105, 1987.

[36] S. Bryson and C. Levit, "The virtual wind tunnel," *IEEE Computer Graphics and Applications*, vol. 12, no. 4, pp. 25–34, 1992. Special issue on visualization.

[37] J. J. van Wijk, "A raster graphics approach to flow visualization," in *EUROGRAPHICS '90* (W. Hansmann, F. Hopgood, and W. Strasser, eds.), pp. 251–259, Elsevier Science Publishers B.V. (North-Holland), 1990.

[38] D. N. Kenwright and G. D. Mallinson, "A 3-D streamline tracking algorithm using dual stream functions," in *Proc. IEEE Visualization '92*, pp. 62–68, CS Press, Los Alamitos, CA., 1992.

[39] J. P. M. Hultquist, "Constructing stream surfaces in steady 3-D vector fields," in *Proc. IEEE Visualization '92*, pp. 171–178, CS Press, Los Alamitos, CA., 1992.

[40] J. L. Helman and L. Hesselink, "Visualization of vector field topology in fluid flows," *IEEE Computer Graphics and Applications*, vol. 11, no. 3, pp. 36–46, 1991. Special issue on visualization.

[41] J. L. Helman and L. Hesselink, "Surface representations of two- and three-dimensional fluid flow topology," in *Proc. IEEE Visualization '90*, pp. 6–13, CS Press, Los Alamitos, CA., 1990.

[42] J. J. van Wijk, "Flow visualization with surface particles," *IEEE Computer Graphics and Applications*, vol. 13, no. 4, pp. 18–24, 1993. Special issue on scientific visualization.

[43] A. Perry and B. Fairlie, "Critical points in flow patterns," *Advances in Geophysics B*, vol. 18, pp. 299–315, 1974.

[44] A. Perry and M. Chong, "A description of eddying motions and flow patterns using critical point concepts," *Annual Review of Fluid Mechanics*, vol. 19, pp. 125–155, 1987.

[45] M. S. Chong, A. E. Perry, and B. J. Cantwell, "A general classification of three-dimensional flow fields," *Physics of Fluids A*, vol. 2, no. 5, pp. 765–777, 1990.

[46] A. Globus, C. Levit, and T. Lasinski, "A tool for visualizing the topology of three-dimensional vector fields," in *Proc. IEEE Visualization '91*, pp. 33–40, CS Press, Los Alamitos, CA., 1991.

[47] H. Vollmers, "The recovering of flow features from large numerical databases," in *Computer Graphics and Flow Visualization in Computational Fluid Dynamics*

(von Karman Lecture Series 1991-07), von Karman Institute for Fluid Dynamics, Rhode Saint Genèse, Belgium, Sept. 1991.

[48] R. R. Dickinson, "Interactive analysis of the topology of 4-D vector fields," *IBM Journal of Research and Development*, vol. 35, no. 1, pp. 59–66, 1991. Special issue on visual interpretation of complex data.

[49] G. Belie, "Flow visualization in the space shuttle's main engine," *Mechanical Engineering*, vol. 107, no. 9, pp. 27–33, 1985.

[50] G. Volpe, "Streamlines and streamribbons in aerodynamics," in *AIAA 27th Aerospace Sciences Meeting*, Jan. 1989. AIAA paper 89-0140.

[51] W. J. Schroeder, C. R. Volpe, and W. E. Lorensen, "The stream polygon: a technique for 3-D vector field visualization," in *Proc. IEEE Visualization '91*, pp. 126–132, CS Press, Los Alamitos, CA., 1991.

[52] R. Haimes, M. Giles, and D. Darmofal, "Visual3 - a software environment for flow visualization," in *Computer Graphics and Flow Visualization in Computational Fluid Dynamics (von Karman Lecture Series 1991-007)*, von Karman Institute for Fluid Dynamics, Rhode Saint Genèse, Belgium, Sept. 1991.

[53] L. Hesselink, "Digital image processing in flow visualization," *Annual Review of Fluid Mechanics*, vol. 20, pp. 421–485, 1988.

[54] M. J. Lighthill, "Introduction. Boundary layer theory," in *Laminar Boundary Layers* (L. Rosenhead, ed.), pp. 46–113, Oxford University Press, 1963.

[55] J. L. Helman and L. Hesselink, "Representation and display of vector field topology in fluid flow data sets," *Computer*, vol. 22, no. 8, pp. 27–36, 1989. Special issue on scientific visualization.

[56] M. Tobak and D. J. Peake, "Topology of three-dimensional separated flows," *Annual Review of Fluid Mechanics*, vol. 14, pp. 61–85, 1982.

[57] G. T. Chapman and L. A. Yates, "Topology of flow separation on three-dimensional bodies," *Applied Mechanics Reviews*, vol. 44, pp. 329–345, July 1991.

[58] G. K. Batchelor, "Axial flow in trailing line vortices," *Journal of Fluid Mechanics*, vol. 20, no. 4, pp. 645–658, 1964.

[59] L. A. Yates and G. T. Chapman, "Streamlines, vorticity lines, and vortices around three-dimensional bodies," *AIAA Journal*, vol. 30, no. 7, pp. 1819–1826, 1992.

[60] H. K. Moffat, "The degree of knottedness of tangled vortex lines," *Journal of Fluid Mechanics*, vol. 35, no. 1, pp. 117–129, 1969.

[61] Y. Levy, D. Degani, and A. Seginer, "Graphical visualization of vortical flows by means of helicity," *AIAA Journal*, vol. 28, pp. 1347–1352, Aug. 1990.

[62] W. Rudin, *Principles of Mathematical Analysis.* McGraw-Hill, New York, third ed., 1976.

[63] K. Perlin, "Hypertexture," *Computer Graphics*, vol. 23, no. 3, pp. 253–262, 1989.

[64] J. Maillot, H. Yahia, and A. Verroust, "Interactive texture mapping," *Computer Graphics (SIGGRAPH'93 Proceedings)*, vol. 27, pp. 27–34, 1993.

[65] W. H. Press, S. A. Teukolsky, W. T. Vetterling, and B. P. Flannery, *Numerical Recipes in C. The Art of Scientific Computing.* Cambridge University Press, NY, second ed., 1992.

[66] W. T. Ashurst, A. R. Kerstein, R. M. Kerr, and C. H. Gibson, "Alignment of vorticity and scalar gradient with strain rate in simulated navier-stokes turbulence," *Phys. Fluids*, vol. 30, pp. 2343–2353, Aug. 1987.

[67] D. C. Leigh, *Nonlinear Continuum Mechanics.* McGraw-Hill Book Company, New York, 1968.

[68] A. A. Andronov, E. A. Leontovich, I. I. Gordon, and A. G. Maier, *Qualitative Theory of Second-Order Dynamic Systems.* John Wiley & Sons, Chichester, 1973.

[69] L. Perko, *Differential Equations and Dynamical Systems.* Springer-Verlag, New York, 1991.

[70] I. Bendixson, "Sur les courbes définies par des équations différentielles," *Acta Mathematica*, no. 24, 1901.

[71] P. A. Firby and C. F. Gardiner, *Surface Topology.* Ellis Horwood series in Mathematics and its Applications, John Willey & Sons, New York, 1982.

[72] J. W. Milnor, *Topology from the Differentiable Viewpoint.* The University Press of Virginia, Charlottesville, 1965.

[73] S. Lefschetz, *Differential Equations: Geometric Theory.* Dover Publications, New York, second ed., 1977.

[74] M. Spivak, *A Comprehensive Introduction to Differential Geometry*, vol. 3. Publish or Perish, Berkeley, 2 ed., 1979.

[75] R. C. Gonzales, *Syntactic Pattern Recognition: an Introduction.* Addison-Wesley, Reading MA, 1978.

[76] G. Wyszecki and W. S. Stiles, *Color Science. Concepts and methods, quantitative data and formulae.* John Wiley & Sons, 2 ed., 1982.

[77] H. Levkowitz and G. T. Herman, "Color scales for image data," *IEEE Computer Graphics and Applications*, vol. 12, no. 1, pp. 72–80, 1992.

[78] P. P. Walatka, J. Clucas, R. K. McCabe, and T. Plessel, "FAST user guide. Beta 2.1," tech. rep., NASA Ames Research Center, Apr. 1992.